

UNIVERSITÀ CAMPUS BIO-MEDICO DI ROMA

CORSO DI DOTTORATO DI RICERCA IN INGEGNERIA BIOMEDICA

XXV CICLO ANNO 2010

A Framework for ECG Signal Processing based on Quadratic Variation Reduction

Advisor

Prof. Giulio Iannello

Co-Advisor

Dr.Eng. Antonio Fasano

Ph.D. Candidate

Valeria Villani

April 2013

A Camillo

*Non quia difficilia sunt non audemus,
sed quia non audemus difficilia sunt.*

Lucius Annaeus Seneca

Abstract

The analysis of the electrocardiogram (ECG) is the standard diagnostic tool for the assessment of heart function and the diagnosis of cardiac diseases. Unfortunately, ECG signal is highly susceptible to several kinds of noise, such as thermal and electromyographic noise, power-line interference, motion artifacts, and baseline wander. In this dissertation, a framework for ECG signal processing based on the notion of *quadratic variation reduction* is proposed. The quadratic variation is a consistent measure of variability for vectors or sampled functions.

In recent years, growing interest has been focused on the analysis of single waves of the ECG, like P-waves or T-waves. Being able to track beat-to-beat changes of such waves has proven to be helpful in predicting important heart diseases, such as atrial fibrillation (AF). Since single waves have low SNR, they are commonly analyzed via signal averaging. In this way information about beat-to-beat variability is unavoidably masked or possibly lost. To cope with this problem, in Chapter 3 a smoothing and denoising algorithm for ECG single waves is proposed, which is based on the notion of quadratic variation reduction. The algorithm is the closed-form solution to a constrained convex optimization problem, where the quadratic variation enters as a constraint. Numerical results show that the approach achieves considerable SNR gain over the whole range of practical input SNRs.

In Chapter 3 the algorithm is successfully applied to the prediction of AF through the analysis of P-waves beat-to-beat variability. Denoising by quadratic variation reduction enters in the definition of a metric that measures P-waves variability. The study of the statistics of such a metric allows to discriminate between AF-prone and healthy subjects.

Narrowband artifacts, such as power-line interference, are another common

kind of noise affecting ECG waves. In Chapter 4 is proposed a *joint* approach to denoising and narrowband artifacts rejection. It is achieved by solving a constrained convex optimization problem, where the energy content of harmonic artifacts enters as an additional constraint.

The improvement achieved by the approach based on quadratic variation reduction is notable, and this makes worth its extension to the smoothing of entire ECGs. However, this is effective if the local structure of the ECG is explicitly taken into account in the smoothing operation. In Chapter 5 a smoothing and denoising algorithm for entire ECGs is proposed. Smoothing is performed by *locally* reducing the variability, i.e., the quadratic variation, of the measured ECG, by an amount that is inversely related to the local SNR. Numerical results show that the smoothing performance is significant. The algorithm is favorable also in terms of complexity, which is *linear* in the size of the record to smooth.

In the presence of noise and narrowband artifacts, a combined approach based on joint denoising and artifacts rejection is needed. This is pursued in Chapter 6, where smoothing and narrowband artifacts rejection are performed jointly combining local characteristics of the ECG and the spectral localization of the artifacts to reject. Simulation results confirm the effectiveness of the approach and highlight a notable ability to smooth and denoise ECG signals.

Finally, in Chapter 7 the problem of baseline wander removal is tackled. This is an unavoidable step in any processing of ECG signals. Baseline wander and ECG have partially overlapping bands in the low-frequency region of the spectrum. This makes its removal difficult without affecting the ECG, in particular the ST segment, which is related to the diagnosis of acute coronary syndromes. Due to the in-band nature of this kind of noise, any technique for its removal that relies on spectral shaping, e.g., linear time-invariant filtering, will unavoidably alter the ST segment. To cope with this problem it is necessary to analyze baseline noise and ECG components contributing to the ST segment in a domain that is not the frequency domain. In this regard, the quadratic variation turns out to be a suitable measure of variability that is not directly related to the frequency domain. In Chapter 7 baseline wander is estimated as the component of measured ECG with the lowest variability. Comparative analyses show that the approach outperforms state-of-the-art algorithms and is superior in removing baseline wander, while preserving the ST segment. The approach compares favorably also in

Abstract

terms of computational complexity, which is *linear* in the size of the vector to de-trend. This makes it suitable for real-time applications as well as for applications on devices with reduced computing power, e.g., handheld devices.

All the techniques described for smoothing, rejection of power-line noise and, in general, narrowband artifacts, either for single waves or entire ECGs, and for baseline wander removal, share a common approach, although with different technicalities. This approach is based on the notion of quadratic variation reduction and constitutes the common framework for ECG signal processing, which is the object of this dissertation.

Preface

This doctoral thesis is based on the following journal papers:

- [1] A. Fasano and V. Villani, “Fast baseline wander estimation and removal by quadratic variation reduction,” *Submitted for publication*.
- [2] A. Fasano and V. Villani, “Baseline wander removal for bioelectrical signals by quadratic variation reduction,” *Submitted for publication*.
- [3] V. Villani and A. Fasano, “Fast ECG baseline wander removal preserving the ST segment,” *Manuscript in submission*.
- [4] A. Fasano and V. Villani, “Smoothing and denoising for ECG waves by quadratic variation reduction,” *Manuscript in submission*.

and conference papers:

- [5] A. Fasano, V. Villani, L. Vollero, and F. Censi, “ECG P-wave smoothing and denoising by quadratic variation reduction,” *Int. Conf. on Bio-Inspired Systems and Signal Processing (BIOSIGNALS)*, 2011.
- [6] V. Villani, A. Fasano, L. Vollero, F. Censi, and G. Boriani, “Measuring P-wave morphological variability for AF-prone patients identification,” *Int. Conf. on Bio-Inspired Systems and Signal Processing (BIOSIGNALS)*, 2011.
- [7] A. Fasano, V. Villani, and L. Vollero, “Denoising and harmonic artifacts rejection for ECG P-waves by quadratic variation reduction,” *Proc. 33rd Annu. Int. Conf. IEEE Eng. Med. Biol. Soc. (EMBC)*, 2011.

- [8] A. Fasano, V. Villani, and L. Vollero, "Baseline wander estimation and removal by quadratic variation reduction," *Proc. 33rd Annu. Int. Conf. IEEE Eng. Med. Biol. Soc. (EMBC)*, 2011.
- [9] A. Fasano, V. Villani, and L. Vollero, "ECG smoothing and denoising by local quadratic variation reduction," *Int. Symp. Appl. Sci. Biomed. Commun. Tech. (ISABEL)*, 2011. (**Recipient of the Best Paper Award**)
- [10] A. Fasano, V. Villani, and L. Vollero, "Fast ECG baseline wander removal preserving the ST segment," *Int. Symp. Appl. Sci. Biomed. Commun. Tech. (ISABEL)*, 2011.
- [11] A. Fasano, V. Villani, and G. Iannello, "ECG denoising and power-line interference rejection by local quadratic variation reduction," *Terzo Congresso del Gruppo Nazionale di Bioingegneria (GNB2012)*, 2012.
- [12] A. Fasano, V. Villani, and G. Iannello, "Fast and effective baseline wander estimation and removal," *Terzo Congresso del Gruppo Nazionale di Bioingegneria (GNB2012)*, 2012.
- [13] A. Fasano and V. Villani, "Joint denoising and narrowband artifact rejection for ECG signals," *Computers in Cardiology (CinC)*, 2012.

Some unpublished results are also presented.

Acknowledgements

I would like to express my gratitude to my supervisor, Prof. Giulio Iannello, for having given me the opportunity to join his group and for having introduced me to research work. Without his willingness, this experience would not even have started.

I am also grateful to my co-supervisor, Dr. Antonio Fasano, for his constant warm advice all over these years. His enthusiasm and brilliant mind were the reasons I started postgraduate studies. Everyday interaction with him have widened my mind. His teachings initiated me to scientific reasoning. His devotion to science has been a spur to hard honest work. He has shared all his knowledge and experience with me and always encouraged me to do my best. His lessons about science and life have helped me and enriched my person. He has been my guide and my mentor, and, with time passing by, my friend. I feel deeply in debt with him for all the time he has sacrificed for me and for all the help and advice he has donated me. Seeing satisfaction for my work in his eyes has been the greatest reward I could have.

In these years, I have learnt one of the most important lessons in life: a life without friends is not worth living. Thank you, Annette, Costa, Cri and Manu for having taught me this. Thank you for tolerating my long silent periods and all the emails and SMSs I have never replied to. Thank you for all your nice thoughts in my worst moments, all your care and your silly jokes that make me feel happy and lucky everyday. Your love has been the best medicine for my sorrows. And, please, forgive me for all the times I was far from you when you needed me. And again, Antonio, thank you for having donated me your friendship. You all are one of the best memories I will have from these years.

I also wish to thank my colleagues and friends in the lab as their nice company

Acknowledgements

and nerd jokes have softened endless days of work. Thanks to Roberto, for his being always willing to help out and for our long chats.

Finally, the hardest part. It is impossible to properly thank someone who has given you everything he/she could, even birth. Mum and Dad, whatever I could write here would be so infinitely little compared to all you have been donating me since I have been alive. You are the strength that keeps me going on everyday, getting over difficulties and all my fears. I will never stop to thank you for having always left me free to follow my passions and dreams, even though this has brought us far apart. Your devotion has taken me to this goal, which is *our* goal, since without your help and love nothing would have been possible. I hope that I will always deserve your pride and that one day in the future I could reward your sacrifices. *Thank you.*

List of symbols

$\mathbf{1}$	vector whose elements equal one
\mathfrak{D}_i	matrix defined in (5.2.4)
\tilde{W}	matrix extracted from the DFT matrix as described in Subsection 4.2.3
D	matrix defined in (3.3.2)
I	identity matrix
q	smoothed vector
W	DFT matrix
z	detrended vector
$\hat{F}(\cdot)$	empirical distribution function
$(\cdot)^H$	transpose conjugate
$(\cdot)^T$	transpose
$[\mathbf{x}]$	quadratic variation of \mathbf{x} as defined in (3.3.2)
$\ \cdot\ ^2$	Euclidean norm
$\mathbb{E}\{\cdot\}$	expected value
\mathcal{E}_a	energy content of harmonic artifacts as defined in (4.2.2)
$\text{Re}\{\cdot\}$	real part

List of symbols

$\text{tr}(\cdot)$	trace
A-V	atrioventricular
AF	atrial fibrillation
ECG	electrocardiogram
G_{SNIR}	signal-to-noise-and-interference ratio gain
G_{SNR}	signal-to-noise ratio gain
KKT	Karush-Kuhn-Tucker
QVR	quadratic variation reduction
SA	sinoatrial
SNIR	signal-to-noise-and-interference ratio
SNIR_0	signal-to-noise-and-interference ratio before smoothing
SNIR_S	signal-to-noise-and-interference ratio after smoothing
SNR	signal-to-noise ratio
SNR_0	signal-to-noise ratio before smoothing
SNR_S	signal-to-noise ratio after smoothing
WAF	wavelet adaptive filtering

Contents

Abstract	i
Preface	iv
Acknowledgements	vi
List of symbols	ix
Contents	xii
1 Introduction	2
2 The electrocardiogram	6
2.1 Electrical activity of the heart	6
2.2 Characteristics of the normal electrocardiogram	9
2.3 Noise and artifacts in ECG signals	11
3 Smoothing and denoising for single ECG waves	13
3.1 Introduction	14
3.2 State of the art	15
3.2.1 Denoising P-waves	15
3.2.2 Denoising T-waves	17
3.3 Proposed approach	18
3.3.1 Rationale	18
3.3.2 The quadratic variation	19
3.3.3 Smoothing ECG waves	21

Contents

3.4	Simulation results	25
3.5	An application: atrial fibrillation prediction	29
3.5.1	Method	30
3.5.1.1	Study population	30
3.5.1.2	Pre-processing of P-waves	30
3.5.1.3	Quantification of the energy of P-waves differ- ences	31
3.5.2	Results	32
3.6	Conclusions	34
4	Joint smoothing and narrowband artifacts rejection for single ECG waves	36
4.1	Introduction	36
4.2	Proposed approach	38
4.2.1	Rationale	38
4.2.2	The quadratic variation	39
4.2.3	Narrowband artifacts rejection	40
4.2.4	Joint denoising and harmonic artifacts rejection	41
4.3	Simulation results	44
4.4	Conclusions	46
5	Smoothing and denoising for ECG records	48
5.1	Introduction	48
5.2	Proposed approach	50
5.2.1	Rationale: the local quadratic variation	50
5.2.2	ECG smoothing by local quadratic variation reduction	52
5.2.3	Computational issues	55
5.3	Simulation results	56
5.4	Conclusions	61
6	Joint smoothing and narrowband artifacts rejection for ECG records	63
6.1	Introduction	63
6.2	Proposed approach	64
6.2.1	Rationale	64
6.2.2	Smoothing ECG signals	65

Contents

6.3	Simulation results	68
6.4	Conclusions	72
7	ECG baseline wander removal preserving the ST segment	73
7.1	Introduction	74
7.2	The ST segment	77
7.3	Review of baseline wander removal for ECG	79
7.4	The proposed approach	82
7.4.1	Rationale	82
7.4.2	Baseline Wander Estimation and Removal	83
7.4.2.1	Sensitivity analysis	86
7.5	Fast Algorithm for Baseline Estimation	87
7.6	Numerical results	89
7.6.1	Effectiveness in removing baseline wander	90
7.6.1.1	Performance metrics	90
7.6.1.2	Performance on real ECG signals	94
7.6.1.3	Performance on synthetic ECG signals	96
7.6.1.4	Robustness to variations of λ	100
7.6.2	Distortion in the ST segment	108
7.6.3	Overall performance	115
7.6.4	Preliminary results on other bioelectrical signals	116
7.7	Conclusions	118
8	Conclusions	121
	Bibliography	142

This Page Intentionally Left Blank

Chapter 1

Introduction

The analysis of the electrocardiogram (ECG) is the standard diagnostic tool for the assessment of heart function and the diagnosis of cardiac diseases. Unfortunately, ECG signal is highly susceptible to several kinds of noise, such as thermal and electromyographic noise, power-line interference, motion artifacts, and baseline wander, as recalled in Chapter 2. In this dissertation, a framework for ECG signal processing based on the notion of *quadratic variation reduction* is proposed.

In recent years, growing interest has been focused on the analysis of single waves of the ECG, like P-waves or T-waves. Being able to track beat-to-beat changes of such waves has proven to be helpful in predicting important heart diseases, such as atrial fibrillation. Since single waves have low SNR, they are commonly analyzed via signal averaging. In this way information about beat-to-beat variability is unavoidably masked or possibly lost. To cope with this problem, in Chapter 3 a smoothing and denoising algorithm for ECG single waves is proposed [1, 2]. It is based on the idea that the effect of noise and artifacts is to introduce additional “variability” into the measured wave, with respect to the true one. Thus, in [1, 2] the *quadratic variation* is introduced as measure of “variability”, and is proved to be a consistent measure in this regard. Then, the problem of smoothing and denoising is recast as a constrained convex optimization problem, where the quadratic variation enters as a constraint. The solution is obtained searching for the signal closest to the observed one, in the ℓ_2 -norm, that exhibits *reduced quadratic variation*. Following this approach, in [1] the smoothing of P-waves extracted from real data is performed, achieving considerable SNR gain

over the whole range of practical input SNRs. The algorithm is also favorable in terms of computational complexity, which is linear in the size of the vector to smooth. This makes it suitable for real-time applications.

In [3], the smoothing algorithm for single waves has been successfully applied to the prediction of atrial fibrillation (AF) through the analysis of P-waves beat-to-beat variability. Denoising by quadratic variation reduction enters in the definition of a metric that measures P-waves variability. The study of the statistics of such a metric allows to discriminate between AF-prone and healthy subjects [3].

Narrowband artifacts, such as power-line interference, are another common kind of noise affecting ECG waves. Their effect is the introduction of further variability in the signal and, thus, they can be removed using the algorithm described above. However, a joint approach that combines denoising and narrowband artifacts rejection has proven to be more effective in this regard. In Chapter 4 denoising and harmonic artifacts rejection is performed jointly, by solving a constrained convex optimization problem, where the energy content of harmonic artifacts enters as an additional constraint [4]. The computational complexity in this case ranges from $O(n)$ to $O(n \log n)$, being n the length of the record to smooth.

The improvement achieved by the approach based on quadratic variation reduction is notable, and this makes worth its extension to the smoothing of entire ECGs. However, this is effective if the local structure of the ECG is explicitly taken into account in the smoothing operation. Indeed, different portions of ECG exhibit different local SNRs, as the signal changes its morphology and noise can be transient or permanent. In Chapter 5 a smoothing and denoising algorithm for entire ECGs is proposed [5]. Smoothing is performed by *locally* reducing the variability of the measured ECG, by an amount that is inversely related to the local SNR. It is the closed-form solution to a constrained convex optimization problem, where local quadratic variations of different portions of ECG enter as constraints. The smoothing performance is significant even without optimizing smoothing parameters: quantitative analysis on synthetic signals have returned average SNR gain exceeding 15 dB on highly corrupted records with initial SNR as low as 0 dB [5]. Moreover, the algorithm is favorable also in terms of complexity, which is *linear* in the size of the record to smooth, regardless of the number of different portions considered in the smoothing operation.

In the presence of noise and power-line interference and, more generally narrowband artifacts, a combined approach based on joint denoising and artifacts rejection is needed. This is pursued in Chapter 6, where smoothing and narrowband artifacts rejection are performed jointly, solving a constrained convex optimization problem [6, 7]. The optimization problem combines local characteristics of the ECG and the spectral localization of the artifacts to reject. Performances have been evaluated on real and synthetic data. Measuring performance in terms of signal-to-noise-and-interference ratio (SNIR), considering narrowband artifacts as interference, quantitative analysis have shown SNIR gains up to 27.6dB on highly corrupted ECG records with initial SNIR as low as -5 dB [7]. The algorithm can be efficiently implemented using the conjugate gradient method. In this case, the complexity ranges from $O(n)$ to $O(n \log n)$, being n the size of the vector to process.

Finally, the problem of baseline wander removal has been tackled in Chapter 7. Baseline wander is a kind of noise affecting ECG recordings that is ubiquitous in all electrocardiographic devices, and its removal is an unavoidable step in any processing of ECG signals. Baseline wander and ECG have partially overlapping bands in the low-frequency region of the spectrum. This makes its removal difficult without affecting the ECG, in particular the ST segment, which is related to the diagnosis of acute coronary syndromes. Due to the in-band nature of this kind of noise, any technique for its removal that relies on spectral shaping, e.g., linear time-invariant filtering, will unavoidably alter the ST segment. To cope with this problem it is necessary to take a different perspective on baseline noise and ECG components contributing to the ST segment. That is, they should be analyzed in a domain that is not the frequency domain.

In this regard, the quadratic variation turns out to be a suitable measure of variability that is not directly related to the frequency domain [8]. The approach based on quadratic variation reduction has been effectively applied in [9, 10], where baseline wander is estimated as the component of measured ECG with the lowest variability. Comparative analyses has shown that this approach outperforms state-of-the-art algorithms and is superior in estimating and removing baseline wander [11], [10, 12], while preserving the ST segment [8], [13]. The approach compares favorably also in terms of computational complexity, which is *linear* in the size of the vector to detrend. This makes it suitable for real-time applica-

Chapter 1

tions as well as for applications on devices with reduced computing power, e.g., handheld devices.

The techniques described for smoothing, rejection of power-line noise and narrowband artifacts, either for single waves or entire ECGs, and for baseline wander removal share a common framework, which is based on the notion of quadratic variation reduction.

Chapter 2

The electrocardiogram

This chapter contains a concise description of the electrical activity of the heart and the electrocardiographic signal. The scope of this chapter is to provide the reader with concepts and notions that will be referred to throughout the dissertation.

2.1 Electrical activity of the heart

The heart is a double pump composed of four chambers: a right heart pumps blood through the lungs for oxygenation, and a left heart pumps oxygenated blood into the general (systemic) circulation through the peripheral organs. In turn, each of these hearts is a pulsatile two-chamber pump composed of an atrium and a ventricle, which are shown in Figure 2.1.1. Each atrium is a weak primer pump for the ventricle and helps to move blood into the ventricle. The ventricles then supply the main pumping force that propels the blood either through the pulmonary circulation by the right ventricle or through the peripheral circulation by the left ventricle [14]. In particular, the right atrium receives venous blood from the systemic circulation, and the right ventricle pumps it into the pulmonary circulation where oxygen and carbon dioxide are exchanged between the blood and alveolar gases. The blood leaving the lungs enters the left atrium by way of the pulmonary veins. Blood then flows from the left atrium into the left ventricle. The left ventricle ejects the blood into the aorta, which then distributes the blood to all the organs via the arterial system [15].

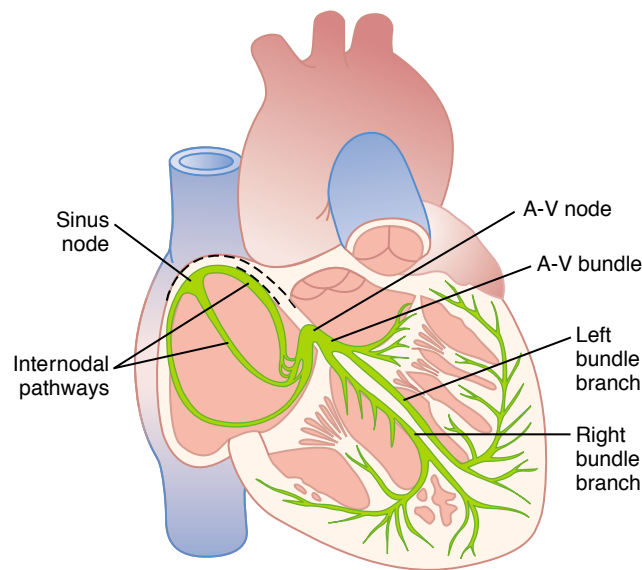


Figure 2.1.1: Electrical conduction system within the heart. A-V: atrioventricular (Figure from [14]).

Each mechanical heartbeat is triggered by an action potential which originates from a rhythmic pacemaker within the heart and is conducted rapidly throughout the organ to produce a coordinated contraction [16]. In normal conditions, the atria contract about one sixth of a second ahead of ventricular contraction, which allows filling of the ventricles before they pump the blood through the lungs and peripheral circulation [14].

The smooth, rhythmic contraction of the atria and ventricles has an underlying electrical precursor in the form of a well-coordinated series of electrical events that takes place within the heart. This set of electrical events is intrinsic to the heart itself. This is well demonstrated by the fact that, when removed from the body and placed in a nutrient medium, the heart continues to beat rhythmically for many hours. Thus, the coordinated contraction of the atria and ventricles is set up by a specific pattern of electrical activation in the musculature of these structures [17].

Normally, the impulse for cardiac electrical stimulation originates in the sinus node, also called sinoatrial (SA) node. It is located in the superior posterolateral wall of the right atrium immediately below and slightly lateral to the opening of

Chapter 2

the superior vena cava [14], as depicted in Figure 2.1.1. The fibers of the SA node have the capability of self-excitation, i.e., they can automatically rhythmically discharge and contract [14]. The rate of rhythmical discharge of the SA node is faster than that of any other part of the heart. As a result, the SA node controls the beat of the heart and is the *pacemaker* of the normal heart [14, 15, 18, 19].

The ends of the SA nodal fibers connect directly with surrounding atrial muscle fibers [14]. Therefore, action potentials originating in the sinus node travel outward into these atrial muscle fibers. In this way, depolarization spreads through the entire atrial muscle mass and signals the atria to contract. As a consequence, blood is pumped nearly simultaneously through the tricuspid and mitral valves into the right and left ventricles [14, 18, 19]. Three anatomic conduction pathways (anterior, middle, and posterior internodal, shown in Figure 2.1.1) originating within or in proximity of the SA node spread excitation through the myocardial atrial tissue [14, 15, 19, 20]. The atrial conductive system is organized so that the cardiac impulse does not travel from the atria into the ventricles too rapidly; this delay allows time for the atria to empty their blood into the ventricles before ventricular contraction begins. The delay in transmission is primarily caused by the atrioventricular (A-V) node and its adjacent conductive fibers. The A-V node is located in the inferior–posterior region of the interatrial septum separating the left from the right atrium [14]. It slows the impulse conduction velocity to about one-tenth the velocity found in atrial or ventricular myocytes [15].

Action potentials leaving the A-V node enter the base of the ventricle at the A-V bundle, known also as bundle of His [14, 15, 18, 19]. A special characteristic of the A-V bundle is the inability, except in abnormal states, of action potentials to travel backward from the ventricles to the atria. Thus, only forward conduction from the atria to the ventricles is allowed [14]. Furthermore, the A-V bundle represents the only route for forward conduction between atrial and ventricular muscle, since everywhere, except at the A-V bundle itself, the atrial muscle is separated from the ventricular muscle by a continuous fibrous barrier [14]. Figure 2.1.1 shows that the A-V bundle from the A-V node penetrates the central fibrous body and passes through the membranous septum as a common bundle and splits into left and right bundle branches at the apex of the muscular septum that separates the two ventricles [15, 18]. The left and right bundle branches lie beneath the endocardium on the two respective sides of the ventricular septum.

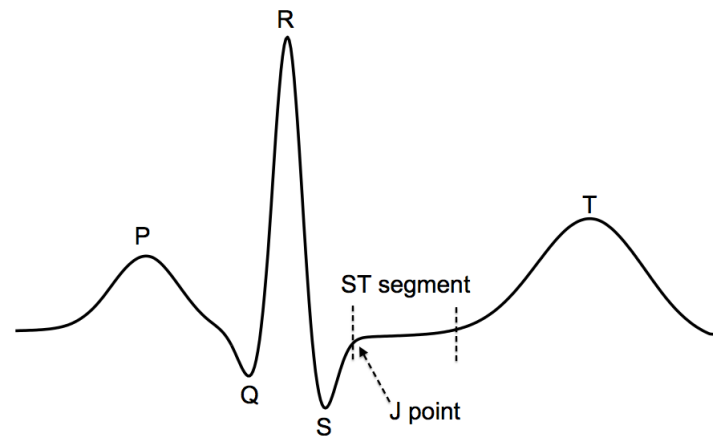


Figure 2.2.1: Typical heartbeat of normal ECG

Each branch spreads downward toward the apex of the ventricle, progressively dividing into smaller branches, as shown in Figure 2.1.1. The bundle branches divide into an extensive system of Purkinje fibers that penetrate into the muscle mass and finally become continuous with ventricular myocytes. These become the final pathway for cell-to-cell conduction within the ventricles [14, 15, 18].

2.2 Characteristics of the normal electrocardiogram

The ECG is a non invasive measure of the electrical activity of the heart recorded by skin electrodes. This activity is caused by repetitive depolarization and polarization of the myocardium during each beat [14]. Physiological ECG signals exhibit a recurrent pattern, where each portion identifies a precise phase of the cardiac cycle. Changes in different parts of this pattern reflect an impairment of the corresponding district of the heart, as will be shown in chapters 3 and 7. The analysis of ECG signals is commonly used as the standard diagnostic tool for the detection of cardiac diseases.

Figure shows a typical beat from a normal ECG consists of a P-wave, a QRS complex, and a T-wave [14].

The *P-wave* is the result of the depolarization that spreads from the SA node throughout the atria. It is caused by electrical potentials generated when the atria

depolarize before atrial contraction begins. In normal adults its duration varies from 0.08 s to 0.11 s [14, 15, 21]. Alterations of P-waves will be discussed in Chapter 3 with regard to atrial fibrillation.

The short isoelectric segment after the P-wave, namely *PQ segment*, corresponds to the interval between the beginning of electrical excitation of the atria and the beginning of excitation of the ventricles. It spans the time required for the propagating impulse to advance from the atria through the A-V node, bundle of His, bundle branches, and the system of Purkinje fibers until the ventricular myocardium begins to depolarize [21]. The normal PQ interval ranges from 0.12 s to 0.20 s [14, 15, 21].

The *QRS complex* represents ventricular depolarization. It occurs at the beginning of contraction of the ventricles and is caused by potentials generated when the ventricles depolarize before contraction, that is, as the depolarization wave spreads through the ventricles [14]. In normal adults the QRS duration varies between 0.07 s and 0.10 s [21]. Since the QRS complex has the largest amplitude of the ECG waveforms, it is used in computer-based analysis for beat detection and delineation [22, 23]. The atria repolarize approximately when the QRS complex is being recorded in the electrocardiogram. Therefore, the atrial repolarization wave is usually obscured by the much larger QRS complex and is seldom observed in the ECG [14, 15].

The *ST segment* is the interval between the end of the QRS complex, namely J point, and the beginning of the T-wave. It is normally isoelectric and represents the period at which the entire ventricle is depolarized. It roughly corresponds to the plateau phase of the ventricular action potential [15, 21]. The ST segment is important in the diagnosis of various cardiac conditions, in which it can become either depressed or elevated, indicating nonuniform membrane potentials in ventricular cells [15]. Moreover, it is susceptible to distortions when baseline wander is removed. The problem of preserving the ST segment while removing baseline wander is tackled in Chapter 7.

The *T-wave* represents the ventricular repolarization and is caused by potentials generated as the ventricles recover from the state of depolarization [14]. Since fibers in the ventricular muscle begin to repolarize not in the same instant, the process of ventricular repolarization extends over a long period. For this reason, the T-wave in the normal electrocardiogram is a prolonged wave, but the

voltage of the T-wave is considerably less than the voltage of the QRS complex, partly because of its prolonged length [14].

2.3 Noise and artifacts in ECG signals

Unfortunately, ECG signals are usually corrupted by different types of noise and interference, originating from external sources or directly from other physiological processes of the body [16, 22]. In the worst cases, the useful signal may be dramatically masked by noise and its informative content can be revealed after appropriate signal processing. In the following, we sketch the main sources of noise and artifacts in ECG signals [16, 22].

Power-line interference is characterized by 50Hz or 60Hz sinusoidal interference, possibly accompanied by a number of harmonics. It is caused by many sources, including supply plugs, outlets, cables, and other equipment operating nearby [24]. Thus, it is ubiquitous in any clinical situation [16, 22, 24]. Although various precautions can be taken to reduce the effect of power-line interference, recordings are often contaminated by residual power-line interference [16, 20, 22, 25, 26]. Chapters 4 and 6 cope with the problem of rejecting power-line interference, and in general narrowband artifacts, from ECG single waves and entire records, respectively.

Electrode motion artifacts are caused by skin stretching, movement of the electrode and, possibly, loss of contact between the electrode and skin. This leads to variation in the impedance at the electrode-skin interface and results in sharp changes in ECG recording [16, 22].

Electromyographic noise is due to the electrical activity originated by muscle contractions. Its spectrum overlaps ECG spectrum in the high-frequency region, where are located ECG components that mainly contribute to QRS complexes. Thus, suppression of electromyographic noise is often cause of distortion in the QRS complex [22, 27]. Moreover, the problem of electromyographic noise suppression becomes extremely important when ECG is recorded during physical exercise, for long-term recording by portable devices (for example, ambulatory Holter monitoring) or for ECG recording of children or of people with injured extremities [27]. In such cases, it is not possible to ensure relaxed conditions for the patient, and the muscular activity is reflected in high-amplitude electromyo-

graphic noise.

Baseline wander is mainly caused by respiration. Additional causes are perspiration, patient's body movements, skin-electrode interface, and variation of the impedance between electrodes and skin due to poor electrode contact [16, 18, 22, 28]. It is modeled as a low-frequency additive noise with band in the range $0 \div 0.8\text{Hz}$ that can extend up to 1 Hz, or even more, during stress tests [16, 22]. The in-band nature of baseline wander makes its removal difficult without affecting the ECG, in particular the ST segment, thus spoiling relevant clinical information [29]. Chapter 7 is entirely devoted to the problem of baseline wander removal with specific regard to preserving the ST segment.

Measurement and quantization noise account for thermal noise and quantization error introduced by quantization in the analog-to-digital conversion, respectively.

Chapter 3

Smoothing and denoising for single ECG waves

In recent years, growing interest has been focused on the analysis of single ECG waves for the purpose of predicting important heart diseases. Given the low signal-to-noise ratio associated to ECG waves, such analyses are possible if noise and artifacts are effectively filtered out from ECG waves. To this end, in this chapter a novel smoothing and denoising algorithm for single ECG waves is presented. The approach is based on the notion of quadratic variation reduction. We prove that quadratic variation is a consistent measure of variability for vectors or sampled functions. The algorithm is the closed-form solution to a constrained convex optimization problem, where the quadratic variation of the noisy wave enters as a constraint. Simulation results confirm the effectiveness of the approach and show that the proposed algorithm is remarkably good at smoothing and denoising ECG waves. The availability of such a smoothing tool for single ECG waves allows the investigation of P-waves beat-to-beat variability for the purpose of atrial fibrillation (AF) prediction. Denoising by quadratic variation reduction enters in the definition of a metric that measures P-waves variability. The study of the statistics of such a metric allows to discriminate between AF-prone and healthy subjects.

3.1 Introduction

In recent years, growing interest has been focused on the analysis of single portions of the ECG, like P-waves, ST segments and T-waves. Being able to track beat-to-beat changes of such waves has proven to be helpful in predicting important heart diseases. This is the case, for example, of the analysis of P-waves for the purpose of atrial fibrillation prediction, the study of T-wave alternans to predict sudden cardiac death, and the analysis of ST segment deviations to detect acute coronary syndromes. Moreover, beat-to-beat analysis may be useful to improve the understanding of the pathophysiological mechanisms of atrial or ventricular substrates predisposing to cardiac disease. However, the analysis of the temporal variability of consecutive waves, whether P- or T-, is possible only if reliable beat-to-beat waves are available. Since single waves have low SNR, these analyses are possible if noise and artifacts are effectively filtered out from such waves. Typically, this is achieved by denoising the whole record and then extracting the portions of interest or via signal averaging. As a consequence, local characteristics of the signal are not taken into account and information about beat-to-beat variability is unavoidably masked or possibly lost. Indeed, each P- or T-wave provides important information about the corresponding depolarization pattern throughout the atrial or ventricular substrate, respectively.

To overcome this limitation, we have recently proposed a novel smoothing and denoising algorithm for ECG single waves [1, 2], which is the object of this chapter. The approach can be applied indistinctly to P-waves and T-waves. It is based on the notion of *quadratic variation*, is meant as a suitable measure of variability for vectors or sampled functions. The notion of *quadratic variation* is introduced in Subsection 3.3.2. The algorithm is derived in Subsection 3.3.3 as the closed-form solution to a constrained convex optimization problem, where smoothing and denoising are achieved by reducing the quadratic variation of the noisy wave. We tested the proposed algorithm on P-waves and compared its performance with a linear-phase FIR low-pass filter [1]. Simulation results, presented in Section 3.4, confirm the effectiveness of the approach and show that the proposed algorithm is remarkably good at smoothing and denoising ECG waves.

In Section 3.5, the smoothing algorithm for single waves is successfully applied to the prediction of atrial fibrillation through the analysis of P-waves beat-

to-beat variability [3]. Following an approach similar to that used for T-waves in the analysis of ventricular repolarization, we investigate P-waves variability, i.e., the variation over time of P-waves morphology.

3.2 State of the art

3.2.1 Denoising P-waves

Atrial Fibrillation (AF) is a sustained cardiac rhythm disturbance characterized by rapid and irregular atrial impulses and ineffective atrial contractions [30]. According to the ATRIA study, its prevalence is 1% of total population, increasing to 9% among patients 80 years or older [31]. The number of persons with AF in the United States in 2010 ranges from ≈ 2.7 to 6.1 million, and is projected to increase to between ≈ 5.6 and 12 million by 2050 [32]. AF is not directly life-threatening but is associated with increased risk of stroke, heart failure, cognitive dysfunction, and premature death [33] and has enormous socioeconomic implications. Annual costs for AF treatment amount to € 3209 per patient in the EU [34] and increase with delay in diagnosis.

AF results from cardiac impulses that have gone berserk within the atrial muscle mass, stimulating first one portion of the atrial muscle, then another portion, then another, and eventually feeding back onto itself to re-excite the same atrial muscle over and over, never stopping. When this happens, many small portions of the atrial muscle will be contracting at the same time, while equally as many other portions will be relaxing. Thus, there is never a coordinate contraction of all the atrial muscle at once, which is required for a pumping cycle of the heart. Despite massive movement of stimulatory signals throughout the atria, the atrial chambers neither enlarge nor contract but remain in an indeterminate stage of partial contraction, pumping either no blood or negligible amounts to ventricles [14]. Moreover, the lack of coordinated atrial contraction leads to unusual fluid flow states through the atrium. These could favor the formation of thrombus at risk to embolize, especially after return to normal sinus rhythm.

On the ECG, AF is described by the replacement of consistent P-waves by rapid oscillations or fibrillatory waves that vary in size, shape, and timing, associated with an irregular, frequently rapid ventricular response when atrioventricular

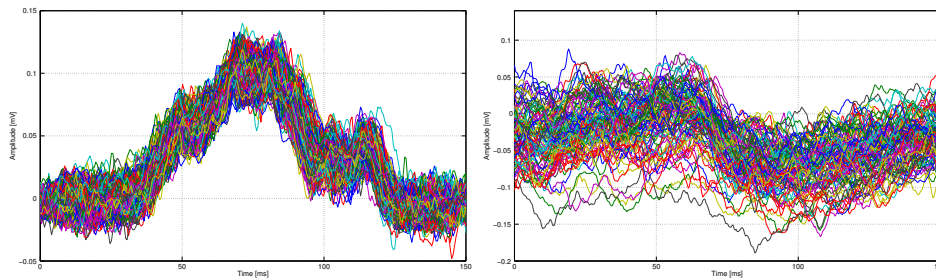


Figure 3.2.1: Butterfly plot of P-waves belonging to a healthy subject (left) and to a patient prone to AF (right).

conduction is intact [14, 30].

The ECG contains valuable prognostic information that can identify patients at risk of AF [35, 36]. Prolonged and fractionated atrial activity during sinus rhythm had been observed in ECG recordings of patients who experienced AF. Conduction defects and abnormal activation patterns in the atria that may lead to AF are manifested in irregular and prolonged P-waves, as exemplified in Figure 3.2.1. As a consequence, time-domain and morphological characteristics of ECG P-waves have been extensively studied to predict AF occurrence or recurrence [35–40].

First studies of P-waves characteristics were performed manually by visual inspection [40, 41], thus incurring in limited accuracy [42]. However, current standard approaches to the analysis of P-waves make use of signal averaging techniques to extract a template [35, 38–40, 43–50]. Then, some features, such as P-wave dispersion or duration, are extracted from the template. Signal averaging is needed to reduce noise, since P-waves exhibit low signal-to-noise ratio. However, the unavoidable drawback of this approach is that some information is lost. Indeed, each P-wave provides important information about the corresponding depolarization pattern throughout the atrial substrate and the electrophysiologic mechanisms underlying AF can be masked in the averaging operation. Moreover, changes between consecutive P-waves, which are representative of irregular and chaotic atrial activation, may be hidden in the template.

3.2.2 Denoising T-waves

The analysis of T-waves is of particular interest since it is related to the prediction and diagnosis of sudden cardiac death and malignant ventricular arrhythmias. Sudden cardiac death refers to death from the abrupt cessation of cardiac function, usually due to a lethal arrhythmia and usually occurs in the background of structural heart disease or coronary artery disease [51]. Almost half a million people die of sudden cardiac death each year in the United States alone, resulting in more deaths than stroke, lung cancer, breast cancer, and AIDS combined. Worldwide, sudden cardiac death comprises 50% of overall cardiac mortality in developed countries [51].

In the last decades, increasing evidence has been reported on the relationship between electrocardiographic phenomenon of T-wave alternans and vulnerability to malignant ventricular arrhythmias and sudden cardiac death [52–54]. In general, alternans of the ECG is defined as a change in the amplitude and/or morphology of a component of the ECG that occurs on an every-other-beat basis. In particular, the T-wave alternans, also termed repolarization alternans, is characterized by changes in shape, amplitude or polarity of the T-wave, appearing with regular rhythmicity, usually every other beat, unaccompanied by gross changes in the cycle length [16, 55, 56]. An example of T-wave alternans is reported in Figure 3.2.2. Macroscopic alternans of the T-wave is a rare appearance. In most cases, such alternans is not detectable by visual inspection, but appears at a microvolt level [57]. Thus, in the effort to assess a clinically useful marker of sudden cardiac death, development of methods for non-invasive automatic detection of non-visible (microvolt) T-wave alternans has been a major challenge in the last two decades [16, 56, 58, 59].

Any system for T-wave alternans detection requires a signal preprocessing step to control for possible effects of factors that may affect T-wave alternans identification. This step usually accounts for noise filtering, baseline wander removal, R peaks detection and T-waves extraction [56, 59, 60]. The most frequent approach to high-frequency noise suppression is low-pass linear filtering, as documented in [59]. Cut-off frequency usually varies in the range from 50Hz to 360Hz, however lower cut-off frequencies (around 15Hz) may be chosen. However, QRS complexes would lose their high-frequency components, what might degrade QRS detection and alignment. Moreover, the widened QRS could confound the adja-

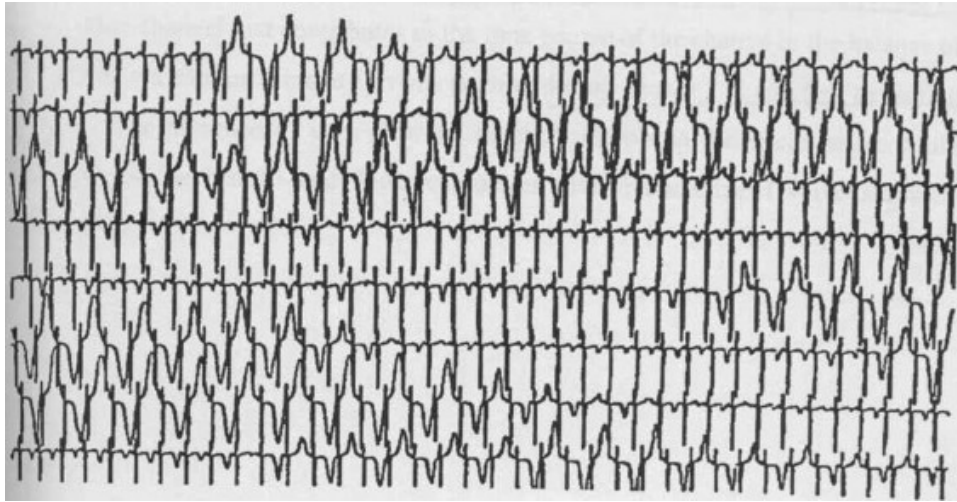


Figure 3.2.2: Continuous ECG tracing showing macroscopic T-wave alternans (Figure from [56]).

cent ST-T complex [59]. In [61] low-pass filtered ECG segments were further compared with a template to reject residual noisy portions. Alternatively to linear filtering, a wavelet based denoising approach is proposed in [62]. Both of these approaches share the fact that denoising is applied to the the whole ECG record and denoised T-waves are then segmented. As a consequence, local characteristics of the single T-waves are not taken into account and some information about beat-to-beat variability may be lost.

3.3 Proposed approach

3.3.1 Rationale

From the previous section, it is evident that the ability to conduct a meaningful analysis of predisposing factors to AF, or sudden cardiac death, strongly depends on the availability of reliable P-waves, or T-waves. In this regard, P-waves, or T-waves, are reliable if the detrimental effects of noise and artifacts are reduced to an acceptable level.

In this section we propose an algorithm that is particularly effective for ECG

single waves smoothing and denoising [1, 2]. It is based on the following idea. The measured wave is affected by noise and artifacts whose effect is to introduce additional “variability” into the observed wave with respect to the true one. Thus, provided that we introduce a suitable index of variability, smoothing and denoising can be performed by searching for a version of the wave that is close, in some sense, to the observed one, but has less “variability”. We make this idea precise in the following.

3.3.2 The quadratic variation

The variability of a generic vector can be quantified introducing the following

Definition 1. Given a vector $\mathbf{x} = [x_1 \cdots x_n]^T \in \mathbb{R}^n$, with $n \geq 2$, the quadratic variation of \mathbf{x} is defined as

$$[\mathbf{x}] \doteq \sum_{k=1}^{n-1} (x_k - x_{k+1})^2 \quad (3.3.1)$$

and is denoted by $[\mathbf{x}]$.

The quadratic variation is a well-known property used in the analysis of stochastic processes [63]. However, in this context we consider it as a function of deterministic or random vectors.

Introducing the $(n-1) \times n$ matrix

$$\mathbf{D} = \begin{bmatrix} 1 & -1 & 0 & \cdots & 0 \\ 0 & 1 & -1 & \ddots & \vdots \\ \vdots & \ddots & \ddots & \ddots & 0 \\ 0 & \cdots & 0 & 1 & -1 \end{bmatrix}, \quad (3.3.2)$$

the quadratic variation of \mathbf{x} can be expressed as

$$[\mathbf{x}] = \|\mathbf{D}\mathbf{x}\|^2, \quad (3.3.3)$$

where $\|\cdot\|$ denotes the Euclidean norm.

The quadratic variation is a consistent measure of variability and its use is motivated by the following property: for vectors affected by additive noise, on av-

erage it does not decrease and is an increasing function of noise variances. Indeed, the following holds.

Proposition 1. *Let $\mathbf{x} = \mathbf{x}_0 + \mathbf{w}$, where $\mathbf{x}_0 \in \mathbb{R}^n$ is a deterministic vector and $\mathbf{w} \in \mathbb{R}^n$ is an absolutely continuous random vector with zero mean and covariance matrix $\mathbf{K}_w = \mathbb{E}\{\mathbf{w}\mathbf{w}^T\}$. Then*

$$\mathbb{E}\{\mathbf{x}\} = \mathbf{x}_0 + \text{tr}(\mathbf{D}\mathbf{K}_w\mathbf{D}^T) \geq \mathbf{x}_0 \quad (3.3.4)$$

where the inequality is strict almost surely¹.

Proof. Taking into account (3.3.3), the average quadratic variation of \mathbf{x} becomes

$$\begin{aligned} \mathbb{E}\{\mathbf{x}\} &= \mathbb{E}\left\{\|\mathbf{D}\mathbf{x}_0\|^2 + \|\mathbf{D}\mathbf{w}\|^2 + 2\mathbf{x}_0^T\mathbf{D}^T\mathbf{D}\mathbf{w}\right\} \\ &= \mathbf{x}_0 + \text{tr}(\mathbf{D}\mathbf{K}_w\mathbf{D}^T) \end{aligned}$$

where, in the last equality, we have exploited the invariance of the trace under cyclic permutations. Note that $\text{tr}(\mathbf{D}\mathbf{K}_w\mathbf{D}^T) \geq 0$, since it is the trace of a positive semidefinite matrix [64], and $\text{tr}(\mathbf{D}\mathbf{K}_w\mathbf{D}^T) > 0$ almost surely. In fact, denoting by $\mathbf{w} = [w_1 \cdots w_n]^T$, we have

$$\text{tr}(\mathbf{D}\mathbf{K}_w\mathbf{D}^T) = \sum_{k=1}^{n-1} \mathbb{E}\left\{(w_k - w_{k+1})^2\right\}.$$

Thus, $\text{tr}(\mathbf{D}\mathbf{K}_w\mathbf{D}^T) = 0$ if and only if the random variables $(w_k - w_{k+1})$, for $k = 1, \dots, n-1$, are almost surely zero, i.e., the components of the noise vector \mathbf{w} are almost surely equal. This event has zero probability since \mathbf{w} is an absolutely continuous random vector, and thus $\text{tr}(\mathbf{D}\mathbf{K}_w\mathbf{D}^T) > 0$ almost surely. \square

Note that in Proposition 1, no assumptions are made about the distribution of \mathbf{w} , so the consistency of quadratic variation as a measure of variability holds *regardless* of the statistics of the noise. Moreover, $\mathbb{E}\{\mathbf{x}\}$ in (3.3.4) is an increasing function of noise variances since

$$\text{tr}(\mathbf{D}\mathbf{K}_w\mathbf{D}^T) = \sum_{k=1}^{n-1} (\sigma_k^2 + \sigma_{k+1}^2 - 2\sigma_{k,k+1}),$$

¹A property holds almost surely if it is true with probability one.

where $\sigma_k^2 = \mathbb{E}\{w_k^2\}$ and $\sigma_{k,k+1} = \mathbb{E}\{w_k w_{k+1}\}$.

The next subsection is devoted to the development of an efficient algorithm for smoothing ECG single waves exploiting the concept of quadratic variation.

3.3.3 Smoothing ECG waves

In this section we denote by \mathbf{q} the vector collecting samples from the measured ECG wave, the one that is affected by noise and artifacts, and by \mathbf{x} the corresponding vector after smoothing. Following the line of reasoning presented in subsection 3.3.1, we determine \mathbf{x} solving the following optimization problem

$$\begin{cases} \underset{\mathbf{x} \in \mathbb{R}^n}{\text{minimize}} & \|\mathbf{x} - \mathbf{q}\|^2 \\ \text{subject to} & [\mathbf{x}] \leq \rho \end{cases} \quad (3.3.5)$$

where ρ is a positive constant that controls the degree of smoothness for \mathbf{q} [1, 2]. Its value is chosen in accordance with the peculiarity of the problem and satisfies $\rho < [\mathbf{x}]$ in order to avoid trivial solutions. In fact, when $\rho \geq [\mathbf{x}]$ the solution is $\mathbf{x} = \mathbf{q}$ and no smoothing is performed. Note that we do not need to know in advance the appropriate value for ρ in any particular problem. In fact, as it will be clear later, the solution to the optimization problem (3.3.5) can be expressed in terms of a parameter that controls the degree of smoothness, i.e., the quadratic variation of the solution, and that is related to the value of ρ in (3.3.5).

Let us consider (3.3.5) in more detail. It is a convex optimization problem, since both the objective function and the inequality constraint are convex. As a consequence, any locally optimal point is also globally optimal and Karush-Kuhn-Tucker (KKT) conditions provide necessary and sufficient conditions for optimality [65]. Moreover, since the objective function is strictly convex and the problem is feasible, the solution exists and is unique. The Lagrangian is

$$\mathcal{L}(\mathbf{x}, \lambda) = \|\mathbf{x} - \mathbf{q}\|^2 + \lambda([\mathbf{x}] - \rho)$$

from the KKT conditions we get

$$\nabla \mathcal{L}(\mathbf{x}, \lambda) = 2(\mathbf{x} - \mathbf{q}) + 2\lambda \mathbf{D}^T \mathbf{D} \mathbf{x} = 0, \quad (3.3.6)$$

$$\lambda([\mathbf{x}] - \rho) = 0, \quad (3.3.7)$$

and the nonnegativity of the Lagrange multiplier $\lambda \geq 0$. However, if $\lambda = 0$ from (3.3.6) it follows that $\mathbf{x} = \mathbf{q}$, which is infeasible since the inequality constraint is not satisfied. Hence $\lambda > 0$ and from (3.3.7) it results that the inequality constraint is active, i.e., $[\mathbf{x}] = \rho$. Thus, solving (3.3.6) we get eventually

$$\mathbf{x} = (\mathbf{I} + \lambda \mathbf{D}^T \mathbf{D})^{-1} \mathbf{q} \quad (3.3.8)$$

where \mathbf{I} denotes the identity matrix, and λ is determined by

$$[\mathbf{x}] = \left\| \mathbf{D} (\mathbf{I} + \lambda \mathbf{D}^T \mathbf{D})^{-1} \mathbf{q} \right\|^2 = \rho. \quad (3.3.9)$$

Note that in (3.3.8) the inverse exists for any $\lambda \geq 0$, since $\mathbf{D}^T \mathbf{D}$ is positive semidefinite, and when $\lambda = 0$ the solution corresponds to not smoothing. It is interesting that the solution to (3.3.8) is a linear operator acting on \mathbf{q} . Moreover, the Lagrange multiplier λ plays the role of a parameter controlling the quadratic variation of the solution \mathbf{x} , i.e., the degree of smoothing applied to \mathbf{q} . In addition, λ can be used in place of ρ since they are in one-to-one correspondence through (3.3.9). In fact, the following property holds true [10].

Proposition 2. *The quadratic variation of \mathbf{x} in (3.3.9) $[\mathbf{x}] = \left\| \mathbf{D} (\mathbf{I} + \lambda \mathbf{D}^T \mathbf{D})^{-1} \mathbf{q} \right\|^2$ is a continuous and strictly decreasing function of $\lambda \in [0, +\infty)$ regardless of \mathbf{q} , provided that it is not a constant vector. When \mathbf{q} is a constant vector $[\mathbf{x}] = 0$. Moreover,*

$$\lim_{\lambda \rightarrow +\infty} [\mathbf{x}] = 0$$

regardless of \mathbf{q} .

Proof. When \mathbf{q} is a constant vector, $\mathbf{q} \in \ker(\mathbf{D})$, i.e., $\mathbf{D}\mathbf{q} = 0$, and the following identities hold

$$\begin{aligned} [\mathbf{x}] &= \left\| \mathbf{D} (\mathbf{I} + \lambda \mathbf{D}^T \mathbf{D})^{-1} \mathbf{q} \right\|^2 \\ &= \left\| (\mathbf{I} + \lambda \mathbf{D} \mathbf{D}^T)^{-1} \mathbf{D} \mathbf{q} \right\|^2 = 0 \end{aligned}$$

where we exploited the identity $\mathbf{D}(\mathbf{I} + \lambda\mathbf{D}^T\mathbf{D})^{-1} = (\mathbf{I} + \lambda\mathbf{D}\mathbf{D}^T)^{-1}\mathbf{D}$ [66].

When \mathbf{q} is not a constant vector we have

$$\begin{aligned} [\mathbf{x}] &= \left\| \mathbf{D}(\mathbf{I} + \lambda\mathbf{D}^T\mathbf{D})^{-1} \mathbf{q} \right\|^2 \\ &= \mathbf{q}^T (\mathbf{I} + \lambda\mathbf{D}^T\mathbf{D})^{-1} \mathbf{D}^T \mathbf{D} (\mathbf{I} + \lambda\mathbf{D}^T\mathbf{D})^{-1} \mathbf{q} \end{aligned} \quad (3.3.10)$$

$$\begin{aligned} &= \mathbf{q}^T \mathbf{D}^T \mathbf{D} (\mathbf{I} + \lambda\mathbf{D}^T\mathbf{D})^{-1} (\mathbf{I} + \lambda\mathbf{D}^T\mathbf{D})^{-1} \mathbf{q} \\ &= \mathbf{q}^T \mathbf{D}^T \mathbf{D} (\mathbf{I} + \lambda\mathbf{D}^T\mathbf{D})^{-2} \mathbf{q} \end{aligned} \quad (3.3.11)$$

since $(\mathbf{I} + \lambda\mathbf{D}^T\mathbf{D})^{-1}$ and $\mathbf{D}^T\mathbf{D}$ commute.

Matrix $\mathbf{D}^T\mathbf{D}$ is symmetric positive semidefinite and thus diagonalizable [64]. Moreover $\mathbf{D}^T\mathbf{D}$ is tridiagonal and has zero as a simple eigenvalue with corresponding unit-norm eigenvector $\frac{1}{\sqrt{n}}\mathbf{1}$ [67]. Thus, the spectral decomposition of $\mathbf{D}^T\mathbf{D}$ can be expressed as

$$\mathbf{D}^T\mathbf{D} = \mathbf{U}\mathbf{\Gamma}\mathbf{U}^T \quad (3.3.12)$$

where $\mathbf{\Gamma} = \text{diag}(0, \gamma_2, \dots, \gamma_n)$ is a diagonal matrix with $\gamma_i > 0$, for $i = 2, \dots, n$, and \mathbf{U} is an orthogonal matrix having $\frac{1}{\sqrt{n}}\mathbf{1}$ as its first column. Taking into account (3.3.12), formula (3.3.11) becomes

$$\begin{aligned} [\mathbf{x}] &= \mathbf{q}^T \mathbf{D}^T \mathbf{D} (\mathbf{I} + \lambda\mathbf{D}^T\mathbf{D})^{-2} \mathbf{q} \\ &= \mathbf{q}^T \mathbf{U} \mathbf{\Gamma} \mathbf{U}^T \mathbf{U} (\mathbf{I} + \lambda\mathbf{\Gamma})^{-2} \mathbf{U}^T \mathbf{q} \\ &= \mathbf{q}^T \mathbf{U} \mathbf{\Gamma} (\mathbf{I} + \lambda\mathbf{\Gamma})^{-2} \mathbf{U}^T \mathbf{q} \\ &= \mathbf{q}^T \mathbf{U} \text{diag} \left(0, \frac{\gamma_2}{(1 + \lambda\gamma_2)^2}, \dots, \frac{\gamma_n}{(1 + \lambda\gamma_n)^2} \right) \mathbf{U}^T \mathbf{q} \\ &= \sum_{i=2}^n \frac{\gamma_i}{(1 + \lambda\gamma_i)^2} (\mathbf{u}_i^T \mathbf{q})^2 \end{aligned} \quad (3.3.13)$$

where \mathbf{u}_i denotes the i th column of \mathbf{U} . Note that, since \mathbf{q} is assumed not a constant vector, there exists at least an index $k \geq 2$ such that $\mathbf{u}_k^T \mathbf{q} \neq 0$ in (3.3.13). In fact, $\mathbf{u}_1^T \mathbf{q}, \dots, \mathbf{u}_n^T \mathbf{q}$, denote the components of \mathbf{q} in the orthonormal basis spanned by the columns of \mathbf{U} . In particular $\mathbf{u}_1^T \mathbf{q}$ is the component along the constant vector $\frac{1}{\sqrt{n}}\mathbf{1}$, whereas $\mathbf{u}_i^T \mathbf{q}$, for $i = 2, \dots, n$, denote the components in the subspace orthogonal

to the constant vectors. Thus, since \mathbf{q} is not constant it must have at least a non zero component in this subspace.

From (3.3.13) it follows that the quadratic variation $[\mathbf{x}]$ is a linear combination with positive coefficients of continuous and strictly decreasing functions of λ and thus it is continuous and strictly decreasing. Moreover, from (3.3.13) it follows

$$\lim_{\lambda \rightarrow +\infty} [\mathbf{x}] = 0$$

regardless of \mathbf{q} , thus proving the proposition. \square

Proposition 2 is equivalent to say that, when \mathbf{q} is not a constant vector, (3.3.9) establishes a one-to-one correspondence between $\lambda \in [0, +\infty)$ and $\rho \in (0, [\mathbf{q}]]$, with $\lambda = 0$ corresponding to $\rho = [\mathbf{q}]$, and $\lambda \rightarrow +\infty$ corresponding to $\rho \rightarrow 0^+$.

A consequence of Proposition 2 is that we *do not need to know* in advance the value of ρ in (3.3.5), since smoothing can be performed according to (3.3.8), without caring about ρ and by reducing parametrically the quadratic variation of the solution \mathbf{x} to the desired level. That is, λ is used in place of ρ as the controlling parameter. In general, the optimal value for the controlling parameter can be found and λ can be adapted to the particular problem or to meet some performance criteria. For example, considering the SNR gain² as a quality index, λ can be chosen as the one that entails the maximum gain. However, different figures of merit can be chosen, according to the peculiarity of the problem.

As stated above, smoothing through (3.3.8) is a linear operator acting on the signal to smooth \mathbf{q} . It is worthwhile noting that the matrix of the transformation, namely $(\mathbf{I} + \lambda \mathbf{D}^T \mathbf{D})^{-1}$, is not Toeplitz [66] and this makes the transformation time variant [68]. As a consequence, there exists *no* linear time-invariant filter that can achieve the same result as (3.3.8) [10]. However, it can be proved that, under some hypotheses, smoothing through (3.3.8) is approximately equivalent to passing the signal through a two-poles IIR filter whose transfer function is the z-transform of an autocorrelation function. Thus its frequency response has zero phase. In particular, it is the autocorrelation function of the impulse response of a single-pole IIR filter. In other words, smoothing through (3.3.8) can be approximately

²This is the ratio between the SNR after and before smoothing.

seen as zero-phase filtering, where data are passed through a single-pole IIR filter in both the forward and reverse directions [2].

It is important to consider the computational aspects related to the smoothing operation, since a matrix inversion is involved in (3.3.8). If the size of the vector \mathbf{q} is large enough computational problems may arise. Actually this is not an issue for the typical length of vectors representing P-waves or T-waves. However, if the same algorithm is applied to a complete ECG recording the computational burden, in terms of time and memory, and the accuracy become serious issues, even for batch processing.

However, smoothing ECG waves through (3.3.8) amounts to solve a linear system where the coefficient matrix, namely $(\mathbf{I} + \lambda\mathbf{D}^T\mathbf{D})$, is tridiagonal [64]. Tridiagonal systems can be solved efficiently with $O(n)$ operations [69], being n the number of unknowns. As a consequence, smoothing using (3.3.8) can be performed with complexity $O(n)$, i.e., *linear* in the size n of the vector \mathbf{q} to smooth. This property is very important and makes the proposed algorithm suitable also for real-time applications.

Finally, it is worthwhile noting that the algorithm we propose is not limited to the smoothing of ECG waves, but it can be applied in very general situations, whenever smoothing and/or denoising are needed. This is due to the fact that the formulation and the rationale behind it, i.e., quadratic variation reduction, have general validity.

3.4 Simulation results

In this section, we report some results we obtained applying the proposed smoothing algorithm to P-waves [1]. Similar results can be achieved considering T-waves, given the generality of the approach.

In order to evaluate the performance of the algorithm, a noiseless reference model of P-wave is needed. In this regard, we considered the P-wave model reported in [70], obtained fitting linear combinations of Gaussian functions to measured P-waves. Such a model can be reliably used to represent real P-waves as documented in the cited reference.

The noiseless reference model considered is reported in Figure 3.4.2. It has a

duration of 200ms and its bandwidth essentially does not exceed 100Hz. It has been sampled at 2048 Hz and the corresponding samples have been collected in a vector denoted by \mathbf{p}_0 .

The noiseless P-wave reference model \mathbf{p}_0 has been corrupted by additive noise, denoted by \mathbf{w} , where the components of \mathbf{w} are independent identically distributed zero mean Gaussian random variables with variance σ_w^2 . Thus, the corresponding noisy P-wave is

$$\mathbf{p} = \mathbf{p}_0 + \mathbf{w}. \quad (3.4.1)$$

In order to assess performance of the proposed algorithm the following quantities have been considered:

- the signal-to-noise ratio before smoothing

$$\text{SNR}_0 = \frac{\|\mathbf{p}_0\|^2}{n \cdot \sigma_w^2}$$

where n is the size of vector \mathbf{p}_0 ;

- the signal-to-noise ratio after smoothing

$$\text{SNR}_s = \frac{\|\mathbf{p}_0\|^2}{\|\mathbf{x} - \mathbf{p}_0\|^2} \quad (3.4.2)$$

where $(\mathbf{x} - \mathbf{p}_0)$ is the error vector with respect to the reference model \mathbf{p}_0 .

In definition (3.4.2), we consider as noise affecting the smoothed vector \mathbf{x} , both the residual Gaussian noise and the reconstruction error.

Performances are measured in terms of SNR gain, defined as

$$G_{\text{SNR}} = \frac{\text{SNR}_s}{\text{SNR}_0} = \frac{n \cdot \sigma_w^2}{\|\mathbf{x} - \mathbf{p}_0\|^2}. \quad (3.4.3)$$

Simulations have been carried out applying smoothing in accordance with (3.3.8) and choosing for λ the value, denoted by λ_{opt} , that entails the maximum SNR gain.

In Figure 3.4.2 the noiseless P-wave reference model \mathbf{p}_0 (red dashed line) is reported. Figure 3.4.1 shows the corresponding noisy version \mathbf{p} , corrupted by

Chapter 3

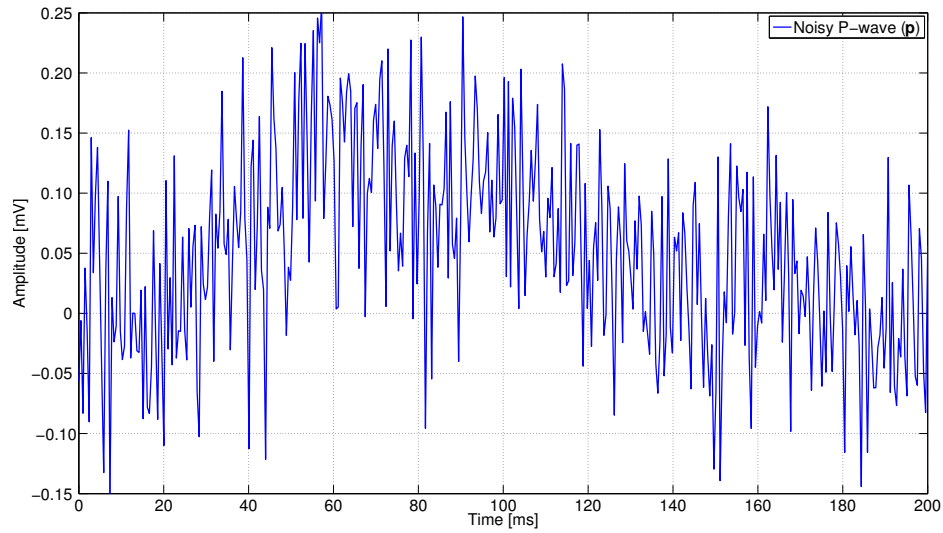


Figure 3.4.1: P-wave reference model of Figure 3.4.2 corrupted by additive Gaussian noise with $\text{SNR}_0 = 0\text{dB}$.

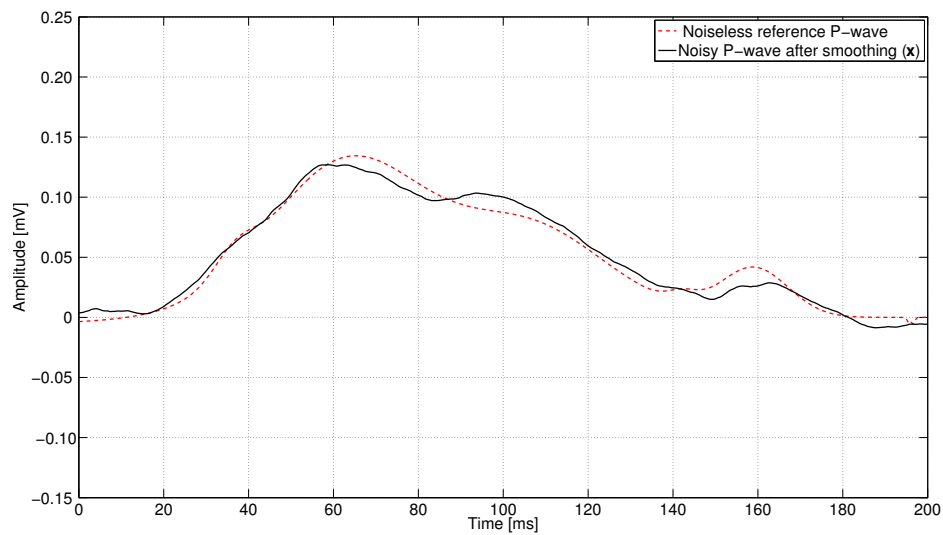


Figure 3.4.2: P-wave reference model p_0 (red dashed line) and smoothed solution x (black continuous line) from the noisy P-wave of Figure 3.4.1 [1].

additive noise according to (3.4.1), with $\text{SNR}_0 = 0\text{dB}$. Note that the SNR in this case is quite low, nevertheless the proposed algorithm is very effective in denoising \mathbf{p} . The resulting smoothed vector, namely \mathbf{x} , is plotted in Figure 3.4.2 (black continuous line) for an easy comparison with the reference model (red dashed line). In this case the resulting SNR gain is quite remarkable and amounts to $G_{\text{SNR}} = 19.4\text{dB}$. It is important to point out that we evaluated the proposed algorithm on different models of P-wave and the resulting gains were all consistent with the ones reported in this work.

In order to evaluate how gain varies as input SNR changes, in Figure 3.4.3 we report the average SNR gain versus input SNR (bottom axis), when the reference P-wave model of Figure 3.4.2 is corrupted by additive noise with SNR ranging from -20dB to 40dB . The top axis of Figure 3.4.3 represents the corresponding in-band SNR, computed using the 100Hz bandwidth of the P-wave reference model. The in-band SNR is about³ 10.1 dB greater than the corresponding input SNR.

For each input SNR we considered the solutions with $\lambda = \lambda_{opt}$ for 300 noise realizations and then we averaged the corresponding SNR gains. As Figure 3.4.3 highlights, the proposed algorithm exhibits a remarkable ability in smoothing P-waves. It achieves considerable gains over the whole range of practical input SNRs and for input SNR $\leq 6\text{dB}$ the average gain exceeds 15 dB. It is remarkable that even when the SNR is quite high the algorithm exhibits considerable gain.

It is worth noting that the proposed algorithm is able to reject both out-of-band and in-band noise. In this regard, low-pass filtering cannot reject in-band noise without altering the signal. Indeed, an ideal 100Hz low-pass filter, in the same setting of our simulation, would exhibit a constant average gain of about 10.1 dB over the whole range of input SNR, as a result of rejection of the sole out-of-band noise. This is confirmed by simulation where we considered a linear-phase FIR low-pass filter synthesized applying the window method [68] to an ideal 100Hz low-pass filter, using a Kaiser window and requiring 0.1 dB ripple in passband and 80 dB attenuation in stopband. In Figure 3.4.3 we report the filter SNR gain versus input SNR, averaged over the same 300 noise realizations used before.

Figure 3.4.3 highlights the effectiveness of the proposed algorithm and shows,

³Actually it is $10\log(10.24)\text{dB} \approx 10.1\text{dB}$, where 10.24 is the ratio between half of the sampling frequency and bandwidth of the P-wave reference model.

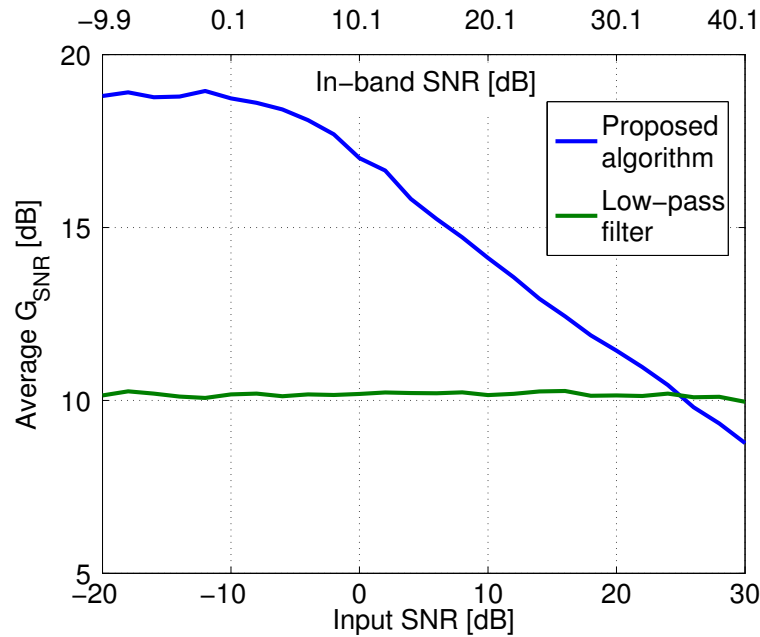


Figure 3.4.3: Average SNR gain G_{SNR} versus input SNR (bottom axis) and in-band SNR (top axis) [1].

in particular considering the in-band SNR, that it outperforms low-pass filtering for all practical values of SNR.

3.5 An application: atrial fibrillation prediction

Through the smoothing algorithm above described, we are able to improve the signal-to-noise ratio of single P-waves. As a consequence, reliable beat-to-beat P-waves are available and the temporal variability of consecutive P-waves can be analyzed. Following an approach similar to that used for T-waves in the analysis of ventricular repolarization [71], it is worth investigating P-waves variability, i.e., the variation over time of morphological characteristics of P-waves. Only few attempts to examine P-wave changes on a beat to beat basis have been proposed [72, 73]. However, beat-to-beat changes have never been deeply investigated or quantified.

In the following we propose an approach to measure beat-to-beat P-waves

variability [3]. Denoising by quadratic variation reduction enters in the definition of a metric that measures P-waves variability. The study of the statistics of such a metric allows to discriminate between AF-prone and healthy subjects, as shown in subsection 3.5.2.

3.5.1 Method

Below we describe the strategy we have developed in order to measure P-waves variability within an ECG tracing of cardiac cycles [3].

3.5.1.1 Study population

The study population consisted of 37 subjects, divided into 2 groups: 21 patients had a persistent form of atrial fibrillation and underwent electrical cardioversion (AF group); 16 subjects had no history of AF and have been considered as controls in this paper (control group). The AF group consists of 10 patients, who experienced at least another documented episode of AF within 3 months after cardioversion (AF relapse group), and 11 patients, who did not experience any documented AF episodes after cardioversion (no-AF relapse group). The Istituto Superiore di Sanità in Rome, Italy, provided us with the ECG signals, which had been acquired at the Institute of Cardiology of the Policlinico Sant'Orsola-Malpighi in Bologna, Italy. Each recording was 5 minutes in duration and was acquired using a high resolution mapping system (BioSemi ActiveTwo, Amsterdam, Netherlands) in a 16-electrodes configuration, with a sampling frequency of 2048 Hz, a resolution of 24-bit (about 30 nV LSB), and a bandwidth from DC to 400 Hz. For AF patients, ECG was recorded after successful cardioversion.

3.5.1.2 Pre-processing of P-waves

P-waves were first isolated according to the method proposed in a previous paper [70]. After the detection of each R-wave, P-waves were extracted in a 200 ms-long window starting from 300 ms before the R-wave. Then, in order to remove baseline wander, a beat-by-beat linear piecewise interpolation was performed, selecting fiducial points from TP and PQ tracks of each beat for linear interpolation. Finally, ectopic atrial signals or P-waves with excessive noise were excluded by

template matching of each P-wave as described in [70]. The extracted P-waves are finite length sampled signals available in the following as vectors having the same size. P-waves from ECG II lead were considered.

3.5.1.3 Quantification of the energy of P-waves differences

P-waves selected during the above mentioned pre-processing phase are analyzed in order to define and characterize statistical indicators of AF phenomena based on P-waves morphological variability.

We denote by \mathbf{p}_i the i -th segmented P-wave of the ECG tracing under analysis and by $\tilde{\mathbf{p}}_i$ the corresponding P-wave after smoothing by the algorithm described above. Let us assume to have N of such waves each L samples long. In order to emphasize the morphological differences instead of absolute differences among waves, a unit-norm normalization is applied to each of them:

$$\hat{\mathbf{p}}_i = \frac{\tilde{\mathbf{p}}_i}{\|\tilde{\mathbf{p}}_i\|}$$

where, according to (3.3.8),

$$\tilde{\mathbf{p}}_i = (\mathbf{I} + \lambda \mathbf{D}^T \mathbf{D})^{-1} \mathbf{p}_i.$$

We propose to evaluate the distance between single P-waves for each subject, namely $\varepsilon_{i,j}$

$$\varepsilon_{i,j} = \|\hat{\mathbf{p}}_i - \hat{\mathbf{p}}_j\|^2 \quad (3.5.1)$$

where $\|\cdot\|$ denotes the Euclidean norm and $\hat{\mathbf{p}}_i$ and $\hat{\mathbf{p}}_j$ are P-waves from the same subject. Thus, (3.5.1) amounts to computing the squared Euclidean norm between single smoothed P-waves, or, equivalently, the squared Mahalanobis distance between single noisy P-waves, i.e., prior smoothing. However other norms revealing specific aspects of waves can be used.

A complete statistical characterization of distance (3.5.1) is provided by its empirical cumulative distribution function:

$$\hat{F}(\varepsilon) = \frac{2}{N(N-1)} \sum_{i < j}^N \chi_{(-\infty, \varepsilon]}(\varepsilon_{i,j})$$

where $\chi_E(\cdot)$ denotes the indicator function of the set E .

Although the empirical cumulative distribution function is rich of information about waves variability, the availability of descriptive parameters may be of interest. In the following we consider the sample mean and the sample variance of the differences energies as indicators:

$$\mu = \frac{2}{N(N-1)} \sum_{i < j}^N \varepsilon_{i,j}$$

$$\sigma^2 = \frac{2}{N(N-1)-2} \sum_{i < j}^N [\varepsilon_{i,j} - \mu]^2$$

3.5.2 Results

Before ECG acquisition, AF patients underwent electrical cardioversion. In Figure 3.5.1, we report the empirical cumulative distribution functions pertaining to controls (top), no-AF relapse group (middle), and AF-relapse group (bottom). Each curve corresponds to a patient.

Top panel of Figure 3.5.1 shows the empirical cumulative distribution function of P-waves differences energy for patients belonging to the control group. All the functions exhibit similar behavior, with a high probability of having low differences among different P-waves. Conversely, in middle and bottom panels of Figure 3.5.1 show the empirical cumulative distribution function of P-waves distance for AF patients. In this case the probability of significant differences among P-waves increases. This effect is considerably more evident in the case of AF relapse group. It is worth noting that the distribution functions of AF relapse group are significantly different from the corresponding functions pertaining to the control group. Moreover, considering the AF relapse and the no-AF relapse groups it is possible to appreciate differences in the distribution functions that allow same level of discrimination between the two groups.

The joint analysis of sample mean and sample variance confirms the difference between the control group and the AF patients groups. Figure 3.5.2 shows the log-log plot of the pair sample mean and sample variance, namely (μ, σ^2) , for each patient. Two regions can be distinguished: bottom-left and top-right regions.

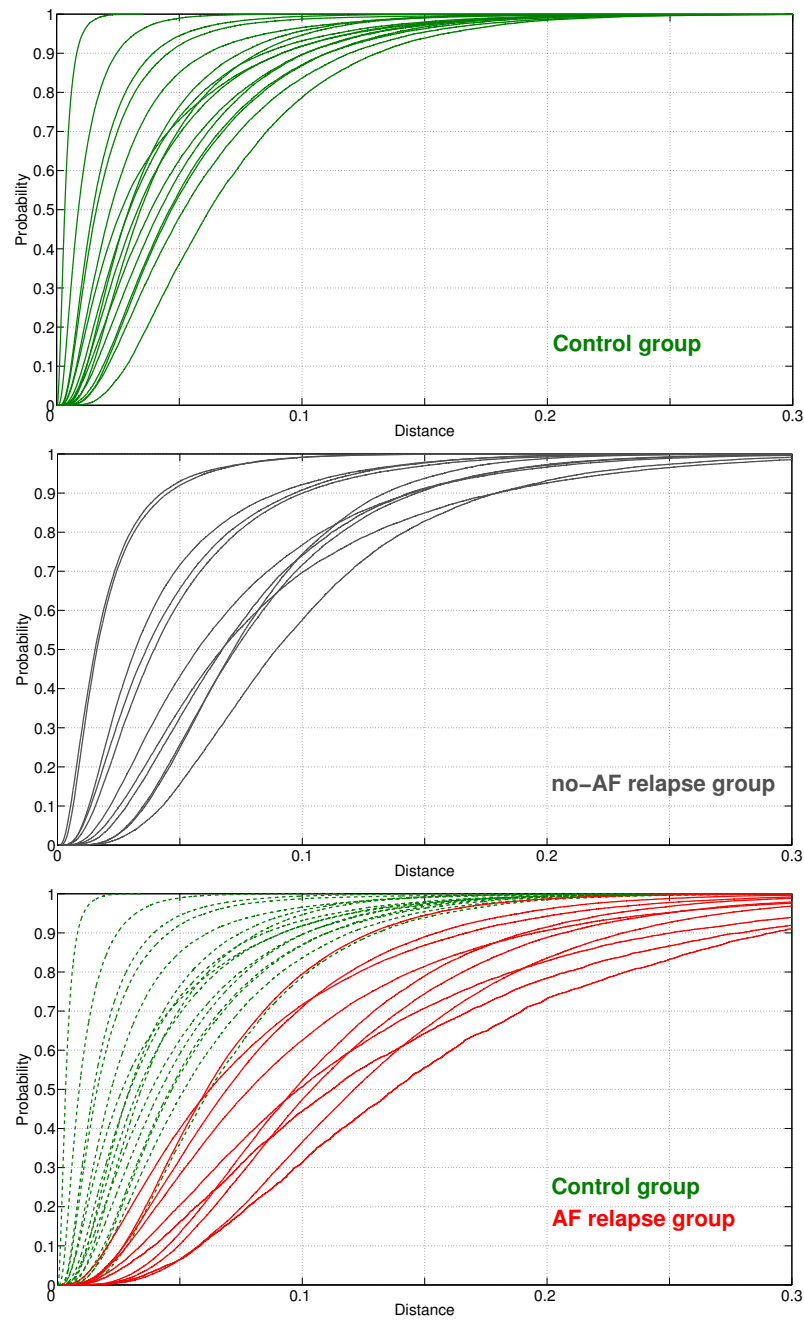


Figure 3.5.1: Empirical cumulative distribution functions of distance between P-waves for controls (top), AF patients in the no-AF relapse group (middle), and AF patients in the AF relapse group, compared to curves for controls (bottom) [3].

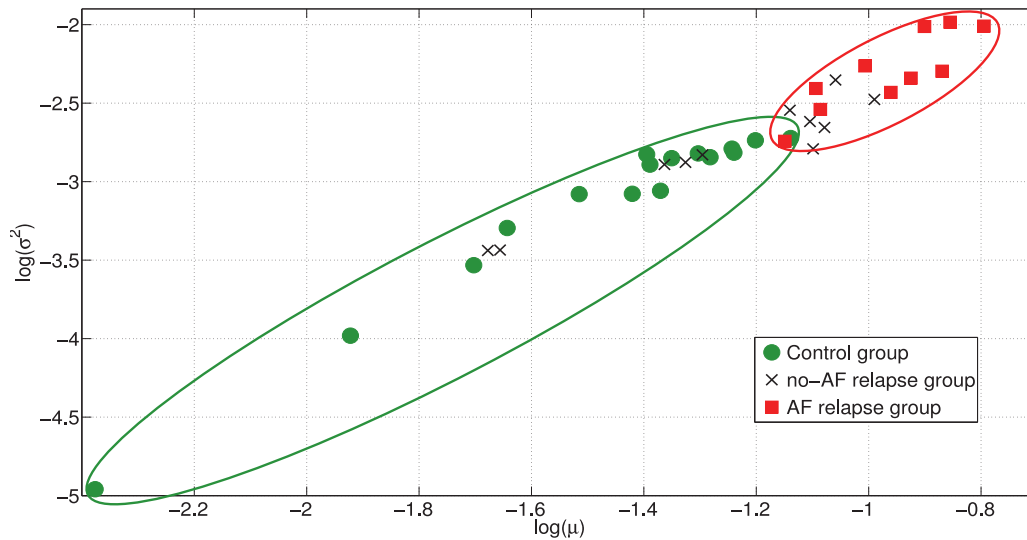


Figure 3.5.2: Sample mean and sample variance of differences energy for AF group and control group [3].

In the bottom-left region both mean and variance of the distance is small. This region identifies controls and, hence, patients without AF problems. Conversely, the top-right region identifies patients belonging to the AF relapse group, i.e., patients with AF problems. In this figure, control group results to be well separated from AF-relapse group. No-AF relapse group turns out to be characterized by intermediate values with respect to other groups. The proposed method seems able to discriminate between healthy and AF patients. In this regard it could be of help in identifying AF-prone patients.

3.6 Conclusions

In this chapter we considered the problem of smoothing and denoising single portions of the ECG, such as P-waves and T-waves. The effort has been motivated by the need to have reliable beat-to-beat P- and T-waves. Indeed, tracking changes between consecutive waves turns out to be very important in understanding the mechanisms underlying cardiac diseases, such as atrial fibrillation and sudden

cardiac death. This is attainable only if reliable waves are available, that is if noise and artifacts are filtered out effectively from each single wave. To this end, we proposed a novel smoothing and denoising algorithm for ECG single waves. It is based on the notion of *quadratic variation reduction*. Quadratic variation is meant as a measure of variability for vectors or sampled functions. The problem of smoothing ECG single waves is recast as a constrained convex optimization problem, where quadratic variation enters as a constraint. The smoothed wave is estimated searching for the signal closest to the observed one, but exhibiting reduced quadratic variation. The computational complexity of the algorithm is *linear* in the size of the vector to be processed, and this makes it suitable also for real-time applications as well as for applications on devices with reduced computing power, e.g., handheld devices. Simulation results on P-waves confirm the effectiveness of the approach and highlight a remarkable ability to smooth and denoise them. Similar results can be achieved with T-waves. Moreover, it is worthwhile remarking that the proposed algorithm is not limited to ECG, but can be effectively applied to a broader class of bioelectrical signals. Indeed, the formulation and the rationale behind it have general validity.

The availability of such a smoothing tool for single ECG waves allows to investigate the temporal variability of waves for the purpose of predicting important heart diseases. In this chapter, we proposed a novel method for the statistical analysis of P-waves beat-to-beat variability aimed at atrial fibrillation prediction. Denoising by quadratic variation reduction enters in the definition of a metric that measures P-waves variability. Taking advantage of the smoothing algorithm, the approach is based on the computation of the empirical cumulative distribution function of distances between consecutive P-waves. The proposed method was tested on P-waves from healthy and atrial fibrillation prone subjects and proved promising for capturing atrial anomalies and identifying patients prone to atrial fibrillation.

Chapter 4

Joint smoothing and narrowband artifacts rejection for single ECG waves

Narrowband artifacts, such as power-line interference, are a common kind of noise affecting ECG waves. Their effect is the introduction of further variability in the signal and, thus, they can be removed using the algorithm described in the previous chapter. However, a joint approach that combines denoising and narrowband artifacts rejection has proven to be more effective in this regard. In this chapter, denoising and harmonic artifacts rejection is performed jointly, by solving a constrained convex optimization problem, where the energy content of harmonic artifacts enters as an additional constraint. The computational complexity in this case ranges from $O(n)$ to $O(n \log n)$, being n the length of the record to smooth. Simulation results confirm the effectiveness of the approach and highlight its ability to remove both noise and artifacts.

4.1 Introduction

In the previous chapter we pointed out the importance of smoothing and denoising single ECG waves. Indeed, the ability to conduct a meaningful analysis of predisposing factors of certain atrial and ventricular diseases strongly depends on the availability of reliable ECG waves, e.g., P-waves and T-waves. In this regard,

ECG waves are reliable if the detrimental effects of noise and artifacts are reduced to an acceptable level. To this end, we proposed a novel algorithm for smoothing and denoising single ECG waves, based on the notion of quadratic variation reduction. In this chapter, we extend to approach to narrowband artifacts rejection.

Narrowband artifacts, which include harmonic artifacts and power-line interference, are a common kind of noise affecting ECG recordings. Power-line interference at 50Hz or 60Hz is a disturbance unavoidably present in any clinical situation [16, 22, 24]. AC fields caused by a power-line represent a common noise source in the ECG, as well as to any other bioelectrical signal recorded from the body surface [16, 17, 22, 24]. They are caused by many sources, including supply plugs, outlets, cables, and other equipment operating nearby [24]. AC fields that may cause interference can be magnetic or electric [17, 24]. A changing magnetic field produced by AC can induce in any nearby conductive loop an electromotive force, which results in an AC potential. A changing electric field produced by an alternating potential can also produce interference by causing AC currents to flow to ground through the system. These currents flow through tissue and electrode impedances, thus producing AC potential. Electric fields can be present even when the apparatus is not turned on, because current is not necessary to establish the electric field [17, 24].

Various precautions can be taken to reduce the effect of power-line interference, such as selection of a recording location with few surrounding electrical devices or appropriate shielding and grounding of the location [25]. Moreover, modern biomedical amplifiers have a very high common mode rejection ratio [26]. Nevertheless, recordings are often contaminated by residual power-line interference, which sometimes can mask the real signal, especially those portions having low amplitude, such as late potentials [16, 22]. Therefore, artifacts suppression is an unavoidable step in any preprocessing of ECG signal before clinical interpretation. However, as remarked in the previous chapter, particular care must be paid in such preprocessing step to preserve signal morphology and retain all relevant clinical information.

Customarily, noise reduction and artifacts rejection are tackled as two distinct problems. Classical approaches to artifacts suppression resort to linear time-invariant notch filtering [16, 22, 25]. However, since power-line amplitude and phase are time-varying, such technique is unable to track slow variations around

the 50/60Hz fundamental and its harmonics. The use of a band-stop filter does not help in this regard since it induces distortions in ECG signals and impacts the correct delineation of waves. Adaptive approaches have been presented to handle variations in power-line frequency and suppress the influence of transients manifested by the occurrence of QRS complexes [22, 74–77]. They track the amplitude, phase and frequency of the fundamental component and of the harmonics of the power-line interference. However, this technique introduces unacceptable transient response time, especially following signals of steep and high amplitude, e.g. the QRS complex [26, 75]. Another approach to the removal of power-line interference is to estimate the amplitude and phase of the interfering sinusoid in an isoelectric segment, usually the PQ or TP segment. Then, the estimated sinusoid is subtracted from the original ECG signal [22, 78].

In the remaining of this chapter, we propose a novel approach to *jointly* suppress noise and narrowband artifacts in ECG single waves, e.g., P-waves or T-waves. The approach has been published in [4]. The rationale behind the proposed approach and the smoothing algorithm are described in Section 4.2. In Section 4.3 numerical results of simulations on P-waves are reported. However, being the proposed approach of general validity, similar results are achieved considering T-waves. Eventually, Section 4.4 follows with conclusions.

4.2 Proposed approach

4.2.1 Rationale

In the previous chapter, we proposed a novel algorithm that proves being quite effective in smoothing ECG single waves. It is based on the idea that the effect of noise and artifacts on ECG waves is to introduce additional “variability” into the measured wave, with respect to the true one. To reduce such amount of undesired “variability”, in Subsection 3.3.2 the quadratic variation is introduced as a measure of “variability”, and we proved it is a consistent measure in this regard. The problem of smoothing and denoising is recast as a constrained convex optimization problem, where the quadratic variation enters as a constraint. The solution is obtained searching for the signal closest to the observed one, but exhibiting reduced quadratic variation.

The effect of narrowband artifacts, such as power-line interference, is the introduction of further variability in ECG waves. Thus, they can be removed using the smoothing algorithm described throughout Section 3.3. However, as will be illustrated in Subsection 4.2.2, a *joint* approach that combines denoising and tailored narrowband artifacts rejection proves to be more effective in this regard. In particular, in Subsection 4.2.3 we quantify the amount of narrowband artifacts through their energy content. Thus, noise and narrowband artifacts suppression is achieved in Subsection 4.2.4 by *jointly* reducing the quadratic variation of waves and the energy content of narrowband artifacts [4].

4.2.2 The quadratic variation

As stated in Subsection 3.3.2, we quantify the variability of a generic vector $\mathbf{x} = [x_1 \cdots x_n]^T \in \mathbb{R}^n$ through its *quadratic variation*, namely $[\mathbf{x}]$, defined as

$$[\mathbf{x}] \doteq \sum_{k=1}^{n-1} (x_k - x_{k+1})^2 = \|\mathbf{D}\mathbf{x}\|^2,$$

where $\|\cdot\|$ is the Euclidean norm and \mathbf{D} has been defined in (3.3.2).

In Subsection 3.3.2 we proved that the quadratic variation is a consistent index of variability for vectors. We motivated its use in denoising signals showing that, for vectors affected by additive noise, on average it does not decrease and is an increasing function of noise variances. In fact, let $\mathbf{x} = \mathbf{x}_0 + \mathbf{w}$, where \mathbf{x}_0 is a deterministic vector and $\mathbf{w} = [w_1 \cdots w_n]^T$ is a zero-mean random vector with covariance matrix $\mathbf{K}_w = \mathbb{E}\{\mathbf{w}\mathbf{w}^T\}$. Computing the averaged quadratic variation of \mathbf{x} , in Proposition 1 we got

$$\mathbb{E}\{[\mathbf{x}]\} = [\mathbf{x}_0] + \text{tr}(\mathbf{D}\mathbf{K}_w\mathbf{D}^T).$$

Considering a typical scenario, let $\mathbf{w} = \mathbf{m} + \mathbf{a}$, where \mathbf{m} is due to white Gaussian noise whereas \mathbf{a} is due to the residual narrowband artifacts, e.g., 50/60Hz power-line noise. We may assume $\mathbf{m} \sim \mathcal{N}(\mathbf{0}, \sigma_m^2 \mathbf{I})$ and $\mathbf{a} = [a_1 \cdots a_n]^T$ vector of samples from a harmonic process, i.e., $a_k = A \cos\left[2\pi\frac{f_0}{F_c}(k-1) + \phi\right]$, with A and ϕ independent, ϕ uniformly distributed in $[0, 2\pi)$, $f_0 \in \{50\text{Hz}, 60\text{Hz}\}$ and F_c being the sampling frequency. Moreover \mathbf{m} and \mathbf{a} are independent.

In this case it is easy to verify that

$$\begin{aligned} \text{tr}(\mathbf{D}\mathbf{K}_w\mathbf{D}^T) &= \\ &= 2(n-1) \left[\sigma_m^2 + 2\mathbb{E}\{A^2\} \sin^2\left(\pi\frac{f_0}{F_c}\right) \right] \\ &= \frac{2\|\mathbf{x}_0\|^2(n-1)}{n} \left[\frac{1}{\text{SNR}} + \frac{4}{\text{SIR}} \sin^2\left(\pi\frac{f_0}{F_c}\right) \right] \end{aligned} \quad (4.2.1)$$

where $\text{SNR} = \frac{\|\mathbf{x}_0\|^2}{n\sigma_m^2}$ denotes the signal-to-noise ratio and $\text{SIR} = \frac{2\|\mathbf{x}_0\|^2}{n\mathbb{E}\{A^2\}}$ is the signal-to-interference ratio, considering the power-line noise as interference. From (4.2.1) it is evident that the average quadratic variation is a decreasing function of SNR and SIR. This supports the rationale behind quadratic variation reduction as a viable criterion for noise reduction. However, in (4.2.1) the SIR^{-1} is multiplied by $4\sin^2(\pi f_0/F_c)$ that is less than 1 when $f_0/F_c < 1/6$. For example, when $f_0 = 60\text{Hz}$ and $F_c = 2048\text{Hz}$ it is about 3×10^{-2} . As a result, low-frequency harmonic artifacts tend to be less attenuated in response to a quadratic variation reduction. Thus, extra conditions must be considered for effective narrowband artifact rejection.

4.2.3 Narrowband artifacts rejection

The approach proposed to effectively reject narrowband artifacts is to exploit quadratic variation reduction *in conjunction* with an additional requirement. The requirement is to make negligible the energy content of narrowband artifacts in the denoised signal [4].

To quantify it, denote by $\mathbf{x} \in \mathbb{R}^n$ a generic real vector and let

$$\mathbf{X} = \mathbf{W}\mathbf{x}$$

be its DFT [68], where $\mathbf{W} = [w_{h,k}]$ is the DFT matrix, with $w_{h,k} = \frac{1}{\sqrt{n}} \exp\{-j2\pi(h-1)(k-1)/n\}$, $h, k = 1, \dots, n$. Now, denote by $\tilde{\mathbf{W}}$ the matrix obtained stacking the rows of \mathbf{W} corresponding to the harmonic components that we want to reject, as depicted in Figure 4.2.1. Note that since \mathbf{x} is a real vector, symmetries occur in

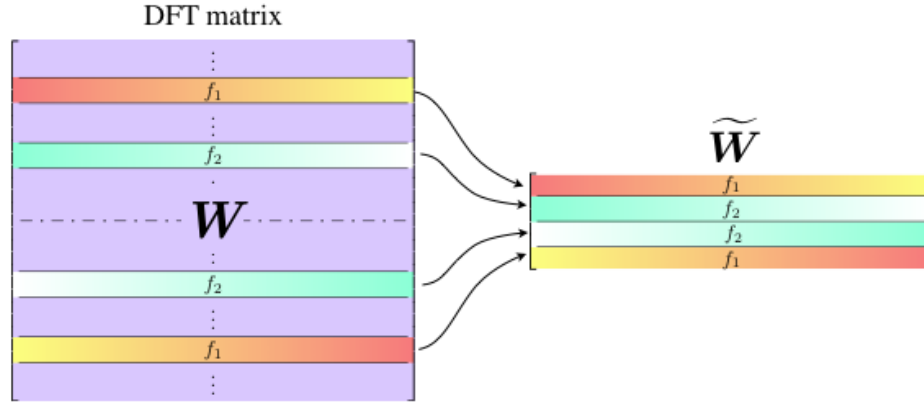


Figure 4.2.1: Extraction of matrix $\tilde{\mathbf{W}}$ from DFT matrix \mathbf{W} : f_1 and f_2 represent the central frequencies of the narrowband artifacts to reject. Note symmetries occurring in both matrices.

its DFT [68] and rows have to be matched in pairs in general.¹ Matrix $\tilde{\mathbf{W}}$ has dimensions $m \times n$, with $m < n$ in general. The quadratic form

$$\mathcal{E}_a = \left\| \tilde{\mathbf{W}}\mathbf{x} \right\|^2 = \mathbf{x}^T \tilde{\mathbf{W}}^H \tilde{\mathbf{W}} \mathbf{x} = \mathbf{x}^T \text{Re} \left\{ \tilde{\mathbf{W}}^H \tilde{\mathbf{W}} \right\} \mathbf{x} \quad (4.2.2)$$

quantifies the energy content of the narrowband artifacts. In (4.2.2) $(\cdot)^H$ denotes the transpose conjugate and $\text{Re}\{\cdot\}$ is the real part.

4.2.4 Joint denoising and harmonic artifacts rejection

In this subsection, using the same nomenclature as in Subsection 3.3.3, we denote by \mathbf{q} the vector collecting samples from the measured ECG wave, the one that is affected by noise and artifacts, and by \mathbf{x} the corresponding vector after smoothing. Following the line of reasoning presented previously, we achieve *joint* denoising and narrowband artifacts rejection by reducing the quadratic variation and the energy content of narrowband artifacts of the noisy wave \mathbf{q} . This amounts to determine \mathbf{x} solving the following optimization problem

¹Apart from some special cases where single rows are taken.

$$\begin{cases} \underset{\mathbf{x} \in \mathbb{R}^n}{\text{minimize}} & \|\mathbf{x} - \mathbf{q}\|^2 \\ \text{subject to} & \|\mathbf{D}\mathbf{x}\|^2 \leq a \\ & \|\tilde{\mathbf{W}}\mathbf{x}\|^2 \leq b \end{cases} \quad (4.2.3)$$

where a and b are positive constants controlling the degree of smoothness for \mathbf{q} . Their values are chosen in accordance with the peculiarity of the problem and satisfy $a < \|\mathbf{q}\|^2$ and $b < \|\mathbf{q}\|^2$ in order to avoid trivial solutions. Indeed, when $a \geq \|\mathbf{q}\|^2$ and $b \geq \|\mathbf{q}\|^2$ the solution is $\mathbf{x} = \mathbf{q}$ and no smoothing is performed.

Let us consider (4.2.3) in more detail. It is a convex optimization problem, since both the objective function and the inequality constraints are convex. As a consequence, any locally optimal point is also globally optimal and Karush-Kuhn-Tucker (KKT) conditions provide necessary and sufficient conditions for optimality [65]. Moreover, since the objective function is strictly convex and the problem is feasible the solution exists and is unique. The Lagrangian is

$$\mathcal{L}(x, \lambda, \nu) = \|\mathbf{x} - \mathbf{q}\|^2 + \lambda \left(\|\mathbf{D}\mathbf{x}\|^2 - a \right) + \nu \left(\|\tilde{\mathbf{W}}\mathbf{x}\|^2 - b \right)$$

and from the KKT conditions we get

$$\begin{aligned} \lambda &\geq 0, \\ \nu &\geq 0, \\ \lambda \left(\|\mathbf{D}\mathbf{x}\|^2 - a \right) &= 0, \\ \nu \left(\|\tilde{\mathbf{W}}\mathbf{x}\|^2 - b \right) &= 0, \end{aligned}$$

$$\nabla \mathcal{L}(x, \lambda, \nu) = 2(\mathbf{x} - \mathbf{q}) + 2\lambda \mathbf{D}^T \mathbf{D}\mathbf{x} + 2\nu \tilde{\mathbf{W}}^H \tilde{\mathbf{W}}\mathbf{x} = 0. \quad (4.2.4)$$

However, if $\lambda = 0$ and $\nu = 0$ from (4.2.4) it follows that $\mathbf{x} = \mathbf{q}$, which is infeasible since the inequality constraints are not satisfied. Hence, the Lagrange multipliers λ and ν cannot be both null at the same time and at least one of the inequality constraints is active.

Solving (4.2.4) we get eventually

$$\mathbf{x} = \left(\mathbf{I} + \lambda \mathbf{D}^T \mathbf{D} + \nu \text{Re} \left\{ \tilde{\mathbf{W}}^H \tilde{\mathbf{W}} \right\} \right)^{-1} \mathbf{q} \quad (4.2.5)$$

where \mathbf{I} is the identity matrix and λ and ν are functions of a and b [4].

Note that in (4.2.5) the inverse exists for any $\lambda \geq 0$ and $\nu \geq 0$ and when $\lambda = \nu = 0$ no smoothing is performed. It is interesting that the solution to (4.2.3) is a linear operator acting on \mathbf{q} . Moreover, the parameters λ and ν control the degree of smoothing applied to \mathbf{q} . In particular, even though λ and ν interact, λ mainly controls the quadratic variation of the solution, i.e., the reduction of wideband noise, whereas ν mainly controls the degree of rejection of narrowband artifacts.

A consequence of (4.2.5) is that we do not need to know in advance the value of a and b in (4.2.3). In fact the solution to the optimization problem (4.2.3) can be expressed in terms of the two parameters λ and ν that control the degree of smoothness of \mathbf{x} and whose values are related to the values of a and b in (4.2.3). Thus, smoothing can be performed without caring about a and b , by reducing parametrically the quadratic variation of the solution and the energy of artifacts to the desired levels. In general, the optimal values for λ and ν can be adapted to fulfill some performance criteria. For example, considering the SNR gain² as a performance index, λ and ν can be chosen to achieve the maximum gain. However, different figures of merit can be chosen, according to the peculiarity of the problem.

Finally, some remarks on the computational aspects related to the smoothing operation, since matrix inversion is involved in (4.2.5). If the size of vector \mathbf{q} is large enough, computational problems may arise. Actually this is not an issue for the typical length of vectors representing P-waves or T-waves, even considering high sampling frequencies. However, in the case of analyses such as the one of P-wave variability in Section (3.5), where smoothing is applied to several waves, the computational burden, both in terms of time and memory, and the accuracy become serious issues, even for batch processing.

In this regard, the proposed algorithm behaves favorably. It is possible to prove that smoothing using (4.2.5) can be performed with complexity $O(n \log n)$ (or $O(n)$ when $\nu = 0$), where n is the size of vector \mathbf{q} . This property is very important and makes it suitable also for real-time applications. Just to give an idea

²This is the ratio between the SNR after and before smoothing.

of how fast the proposed algorithm is, a MATLAB (ver. 7.11) implementation of (4.2.5) with $v > 0$ running over a PC equipped with 2.3 GHz Core i5 processor, takes about 0.23 s to smooth an ECG record of 10^6 double precision floating point samples.

4.3 Simulation results

In this section, we report results obtained applying the above described algorithm for joint denoising and narrowband artifacts rejection to P-waves [4]. Given the generality of the approach, similar results are achieved considering T-waves.

In order to provide quantitative evaluation of performances, we considered a reference noiseless model of P-wave. This has been extracted from a synthetic ECG trace generated using the model described in [79]. The P-wave segment has a duration of 200 ms and has been sampled at 2048 Hz. The corresponding samples have been collected in the vector \mathbf{p}_0 . The reference P-wave \mathbf{p}_0 has been corrupted by additive noise and harmonic artifacts, denoted by \mathbf{w} and \mathbf{d} respectively.

The components of \mathbf{w} are independent identically distributed zero mean Gaussian random variables with variance σ_w^2 such that $\text{SNR} = 10 \log \frac{\|\mathbf{p}_0\|^2}{n \cdot \sigma_w^2} = 2 \text{ dB}$, where n is the length of \mathbf{p}_0 . Concerning harmonic artifacts \mathbf{d} , we considered three sine waves with random phases at frequencies 60 Hz, 80 Hz and 120 Hz, respectively. The sine waves at 60 Hz and 120 Hz account for the first and second harmonics of the power-line noise, whereas the 80 Hz sine wave is a generic harmonic interference. Magnitudes of the waves at frequencies 60 Hz and 80 Hz have been chosen to be the same, whereas magnitude of the sinusoid at frequency 120 Hz has been set to half. The resulting signal-to-interference ratio $\text{SIR} = 10 \log \frac{\|\mathbf{p}_0\|^2}{\|\mathbf{d}\|^2}$ was chosen to be 1.5 dB.

Thus, the corresponding noisy P-wave is

$$\mathbf{p} = \mathbf{p}_0 + \mathbf{w} + \mathbf{d} \quad (4.3.1)$$

and is characterized by a signal-to-noise-plus-interference ratio

$$\text{SNIR}_0 = 10 \log \frac{\|\mathbf{p}_0\|^2}{\|\mathbf{w} + \mathbf{d}\|^2} = -1.3 \text{ dB}.$$

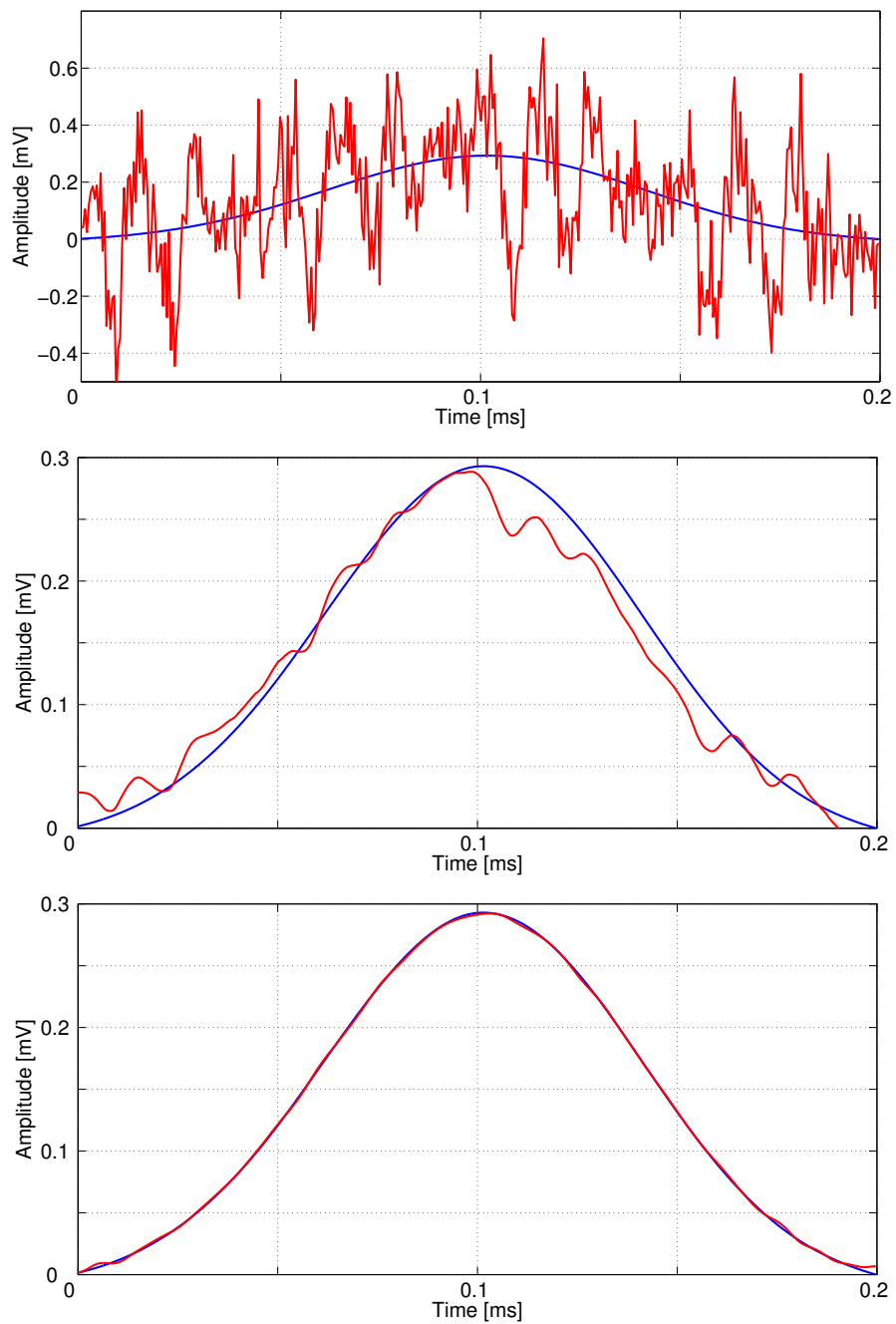


Figure 4.3.1: Top: noiseless reference P-wave (blue) and noisy P-wave (red). Middle: reference P-wave p_0 (blue) and reconstructed P-wave after partial smoothing \tilde{x} (red). Bottom: Reference P-wave p_0 (blue) and smoothed P-wave x (red) [4].

The top panel of Figure 4.3.1 shows the noiseless reference P-wave \mathbf{p}_0 in blue and the corresponding noisy P-wave \mathbf{p} of (4.3.1) in red.

In the middle panel of Figure 4.3.1 we report the reference model (\mathbf{p}_0 , in blue) and the reconstructed wave ($\tilde{\mathbf{x}}$, in red) resulting from a partial smoothing which reduces the quadratic variation of the noisy wave but not the energy of narrowband artifacts, i.e., $\nu = 0$ in (4.2.5). The parameter $\lambda = 524$ was chosen in order to minimize the Euclidean distance $\|\tilde{\mathbf{x}} - \mathbf{p}_0\|$, where $\tilde{\mathbf{x}} - \mathbf{p}_0$ is the error vector with respect to the reference model \mathbf{p}_0 . Although SNIR_0 is quite low, partial smoothing with $\nu = 0$ and $\lambda = 524$ is very effective in denoising \mathbf{p} and the resulting wave $\tilde{\mathbf{x}}$ may be considered a good approximation of \mathbf{p}_0 . Indeed, measuring the performance of the proposed algorithm in terms of SNIR gain

$$G_{\text{SNIR}} = \text{SNIR}_S - \text{SNIR}_0 = 10 \log \frac{\|\mathbf{w} + \mathbf{d}\|^2}{\|\tilde{\mathbf{x}} - \mathbf{p}_0\|^2}$$

where SNIR_S is the SNIR after smoothing and SNIR_0 is the SNIR before smoothing, for these realizations of noise and harmonic interferences we obtain $G_{\text{SNIR}} = 20.7$ dB.

Nevertheless, to reduce the residual oscillatory behavior in $\tilde{\mathbf{x}}$, we considered the combined action of ν and λ . In the bottom panel of Figure 4.3.1 we compare the reference P-wave \mathbf{p}_0 (in blue) and the denoised P-wave \mathbf{x} (in red) resulting from smoothing with ν and λ such as to minimize the Euclidean distance $\|\mathbf{x} - \mathbf{p}_0\|$. Here, the smoothing makes it hard to distinguish between the two waves. The resulting gain is $G_{\text{SNIR}} = 44.3$ dB, considering the same realizations of noise and narrowband interferences of the middle panel of Figure 4.3.1.

Eventually, it is important to point out that we evaluated the proposed algorithm on different models of P-wave, realizations of noise and disturbance vectors. The resulting gains were all consistent with the ones reported in this work.

4.4 Conclusions

In this chapter we considered the problem of noise and narrowband artifacts removal in the ECG waves, e.g., P-waves and T-waves. In particular, narrowband artifacts include harmonic artifacts and power-line interference, which is ubiqui-

tous in clinical environment. Customarily, noise reduction and artifacts rejection are tackled as two distinct problems. In this chapter we have proposed a novel approach to *jointly* suppress noise and narrowband artifacts.

To reject the variability induced in the measured wave by noise and artifacts, we exploit the quadratic variation as a suitable index of variability, and quantify the amount of narrowband artifacts through their energy content. The proposed approach achieves denoising and narrowband artifacts rejection combining two actions: the *joint* reduction of the quadratic variation of the noisy wave and of the energy content of narrowband artifacts. The algorithm is the closed-form solution to a constrained convex optimization problem, where the quadratic variation and the energy content of narrowband artifacts enter as constraints. The smoothing performance is significant: quantitative analysis on synthetic P-waves have returned SNIR gain exceeding 44 dB on highly corrupted wave with initial SNIR as low as -1 dB. The computational complexity of the algorithm is $O(n \log n)$ (or $O(n)$ in some special cases) in the size n of the vector to be processed, and this makes it suitable for real-time applications.

The low complexity of the algorithm makes it suitable, after proper extension, for processing longer signal records, such as whole ECGs, as will be shown in Chapter 6.

Chapter 5

Smoothing and denoising for ECG records

Since the improvement achieved on single ECG waves by the approach based on quadratic variation reduction presented in Chapter 3 is notable, its extension to the smoothing of entire ECGs may be worthy. To be effective, this must take into account the local structure of ECG. In this chapter, we present a fast and effective algorithm for smoothing and denoising ECG records. Smoothing is achieved by locally reducing the quadratic variation of different portions of a noisy ECG by an amount that is inversely related to the local SNR. The computational complexity of the algorithm is linear in the size of the vector under analysis, thus making it suitable for real-time applications and for applications on devices with reduced computing power. Numerical results confirm the effectiveness of the approach and highlight its ability to remove noise and artifacts from ECG signals, outperforming low-pass filtering for all values of SNR.

5.1 Introduction

ECG signals are highly susceptible to contamination by several kinds of noise and artifacts, such as 50 or 60Hz power-line interference, thermal and quantization noise, electromyographic interference, electrode motion artifacts and baseline wander [16, 22]. Thus, noise and artifacts suppression is an unavoidable step in any processing of ECG signals. Several solutions have been proposed in the lit-

erature to suppress noise and artifacts with the aim of preserving ECG morphology. The non-stationary nature of cardiac signal and the in-band nature of noise and artifacts make sometimes ineffective linear time-invariant filtering [16]. To overcome this limitation, several studies focused on adaptive filtering techniques where filters match local characteristics of the processed signal [74, 75, 77, 80].

Multiresolution analysis based on wavelet decomposition is another common technique for ECG denoising [81–84]. Broadly speaking, these approaches decompose the signal into a preset number of components having different scales and resolutions [85]. Components affected by noise are either filtered or discarded by fixed or adaptive thresholding of wavelet coefficients.

Other approaches to ECG denoising resort to mathematical morphology [86–88]. They mainly differ in the choice of the structuring element, the order in which operators are applied, and the way operators are combined.

Further, principal component analysis (PCA) [89] and independent component analysis (ICA) [90, 91] have been proposed for the denoising of ECG records. These approaches are based on multivariate statistical approaches: signal is decomposed into components, which are determined from data and have some geometric (orthogonality) or statistical (independence) properties. Denoising is performed identifying and discarding the components that contribute to noise before signal reconstruction.

A nonlinear Bayesian filtering framework is proposed in [92] for the filtering of single channel noisy ECG recordings. The necessary dynamic models of the ECG are based on a modified nonlinear dynamic model [79], previously suggested for the generation of a highly realistic synthetic ECG.

In [93] a new method for ECG enhancement based on the empirical mode decomposition (EMD) [94] is proposed. EMD acts essentially as a dyadic filter bank resembling those involved in wavelet decompositions [95].

In the recent work [1], extended in [4], we proposed a smoothing algorithm for heavily corrupted single ECG waves, e.g., P-waves and T-waves. The approach has been widely described in Chapter 3 and Chapter 4. It is based on the notion of quadratic variation reduction and proved to be very effective in both denoising and rejecting harmonic artifacts. However, when applied to an entire ECG record its effectiveness reduces, as shown in Subsection 5.2.1, since different portions of a noisy ECG exhibit different local SNRs. The aim of this chapter

is to extend the approach based on the notion of quadratic variation reduction to the smoothing and denoising of entire ECG records. Towards this end, we need to keep into account the local structure of the ECG signal. This is achieved in Subsection 5.2.2 by introducing the notion of *local* quadratic variation. The algorithm is the closed-form solution to a constrained convex optimization problem, where the local quadratic variations of different segments of the ECG enter as constraints [5].

The chapter is organized as follows. The rationale behind the proposed approach and the notion of local quadratic variation are described in Subsection 5.2.1. The smoothing algorithm is derived in Subsection 5.2.2. Computational aspects are discussed in Subsection 5.2.3. Section 5.3 and Section 5.4 follow with numerical results and conclusions.

5.2 Proposed approach

5.2.1 Rationale: the local quadratic variation

The improvement achieved on single ECG waves by the approach based on quadratic variation reduction presented in Chapter 3 is notable, and this makes worth its extension to the smoothing of entire ECGs. However, the amount of additional “variability” introduced in the observed ECG by noise and artifacts is time-varying, since signal morphology changes over time, and noise and artifacts can be persistent, like thermal noise, or transient, like electromyographic noise. As a consequence, different portions of a noisy ECG present different local¹ SNRs. As an example, in Figure 5.2.1 we report a P-wave (black, left) and a QRS complex (black, right) extracted from a simulated ECG [79]. Waveforms in the two panels are reported on the same scale. Although they have been corrupted with white noise with the same variance, the noisy waves (red) exhibit quite different local SNRs: $\text{SNR}_P = 3.2 \text{ dB}$ for the P-wave and $\text{SNR}_{QRS} = 9.6 \text{ dB}$ for the QRS complex. Smoothing these waves by quadratic variation reduction requires two different values of the smoothing parameter λ in (3.3.8): the optimal value for λ , i.e., the one that entails the maximum SNR gain (3.4.3), is $\lambda_P = 12$ for the P-wave

¹The local SNR is the SNR computed on a portion of the signal.

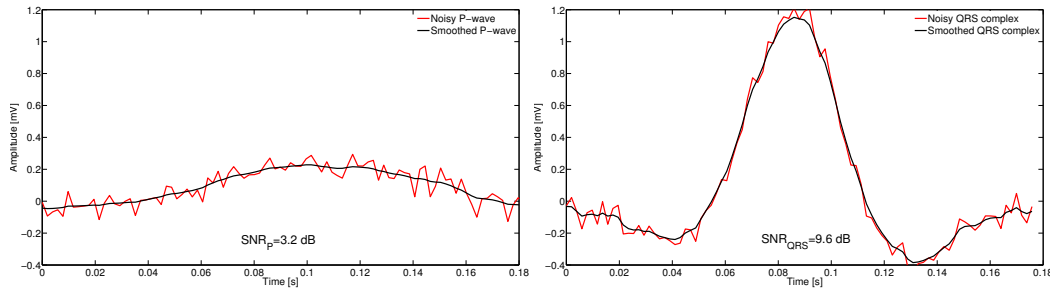


Figure 5.2.1: P-wave and QRS complex corrupted with same noise variance exhibit different local SNRs: $\text{SNR}_P = 3.2 \text{ dB}$ for the P-wave and $\text{SNR}_{QRS} = 9.6 \text{ dB}$ for the QRS complex.

and $\lambda_{QRS} = 2.1$ and the QRS complex. Thus, to be effective smoothing and denoising can be performed by locally reducing the variability of a measured ECG. Considering the quadratic variation (3.3.1) as a suitable measure of variability, this means *locally* reducing the quadratic variation of different portions of a noisy ECG by an amount that is inversely related to the local SNR [5].

Given a vector $\mathbf{x} = [x_1 \cdots x_n]^T \in \mathbb{R}^n$, let us denote a generic subvector² of \mathbf{x} by $\mathbf{x}(k_1, k_2) = [x_{k_1} \cdots x_{k_2}]^T$, with $1 \leq k_1 < k_2 \leq n$, . It will come in handy later to express the quadratic variation of $\mathbf{x}(k_1, k_2)$ in terms of \mathbf{x} . Thus, introducing the diagonal matrix $\mathbf{S}(k_1, k_2) \in \mathbb{R}^{n \times n}$ defined as

$$\mathbf{S}(k_1, k_2) = \text{diag} \{s_1, \dots, s_n\}$$

with

$$s_i = \begin{cases} 1, & k_1 \leq i \leq k_2 \\ 0, & \text{otherwise} \end{cases},$$

the quadratic variation of $\mathbf{x}(k_1, k_2)$ can be computed as

$$[\mathbf{x}(k_1, k_2)] = \|\mathbf{D}\mathbf{S}(k_1, k_2)\mathbf{x}\|^2, \quad (5.2.1)$$

where \mathbf{D} has been defined in (3.3.2).

²Having size greater than or equal to 2.

5.2.2 ECG smoothing by local quadratic variation reduction

In the following, we denote by \mathbf{q} the vector collecting n samples of the measured ECG, which is affected by noise and artifacts, and by $\mathbf{x} \in \mathbb{R}^n$ the corresponding vector after smoothing. The idea is to perform smoothing and denoising by locally reducing the quadratic variation of different portions of the measured ECG.

Let $0 \leq L \leq n - 1$ and assume the vector \mathbf{q} decomposed into $L + 1$ segments

$$\mathbf{q}(k_i, k_{i+1}) = [\mathbf{q}_{k_i} \cdots \mathbf{q}_{k_{i+1}}]^T, \text{ for } i = 0, \dots, L \quad (5.2.2)$$

where indices k_i satisfy

$$1 = k_0 < k_1 < \cdots < k_L < k_{L+1} = n.$$

Segments in (5.2.2) denote distinct portions of the ECG characterized by different local SNRs, like QRS complexes, P-waves or T-waves, as depicted in Figure (5.2.2). Note that two consecutive segments overlap: this choice guarantees the absence of abrupt changes in the smoothed vector \mathbf{x} .

Smoothing is performed searching for a vector \mathbf{x} close to \mathbf{q} , with segments $\mathbf{x}(k_i, k_{i+1})$ having reduced quadratic variation with respect to the corresponding $\mathbf{q}(k_i, k_{i+1})$, i.e., $[\mathbf{x}(k_i, k_{i+1})] < [\mathbf{q}(k_i, k_{i+1})]$. The amount of reduction depends on the segment and is inversely related to the local SNR. In formal terms, smoothing can be achieved solving the following optimization problem

$$\begin{cases} \underset{\mathbf{x} \in \mathbb{R}^n}{\text{minimize}} & \|\mathbf{x} - \mathbf{q}\|^2 \\ \text{subject to} & [\mathbf{x}(k_i, k_{i+1})] \leq a_i, \quad i = 0, \dots, L \end{cases} \quad (5.2.3)$$

where $[\cdot]$ denotes the quadratic variation and a_i , for $i = 0, \dots, L$, are positive constants controlling the degree of smoothness applied to each segment of \mathbf{q} [5]. Their values are chosen in accordance with the peculiarity of the problem and satisfy $a_i < [\mathbf{q}(k_i, k_{i+1})]$ in order to avoid trivial solutions.³ Note that we do not need to know in advance the appropriate values for a_i in any particular problem, as it will be clear later.

³When $a_i \geq [\mathbf{q}(k_i, k_{i+1})]$, for $i = 0, \dots, L$, the solution is $\mathbf{x} = \mathbf{q}$ and no smoothing is performed.

Let us consider (5.2.3) in more detail. It is a convex optimization problem, since both the objective function and the inequality constraints are convex. As a consequence, any locally optimal point is also globally optimal and Karush-Kuhn-Tucker (KKT) conditions provide necessary and sufficient conditions for optimality [65]. Moreover, since the objective function is strictly convex and the problem is feasible the solution exists and is unique. Denoting by

$$\mathfrak{D}_i = \mathbf{DS}(k_i, k_{i+1}) \quad (5.2.4)$$

with $i = 0, \dots, L$, the Lagrangian is

$$\mathcal{L}(\mathbf{x}, \lambda_0, \lambda_1, \dots, \lambda_L) = \|\mathbf{x} - \mathbf{q}\|^2 + \sum_{i=0}^L \lambda_i \left(\|\mathfrak{D}_i \mathbf{x}\|^2 - a_i \right)$$

and from the KKT conditions we get

$$\nabla \mathcal{L}(\mathbf{x}, \lambda_0, \lambda_1, \dots, \lambda_L) = 2(\mathbf{x} - \mathbf{q}) + 2 \sum_{i=0}^L \lambda_i (\mathfrak{D}_i^T \mathfrak{D}_i \mathbf{x}) = 0 \quad (5.2.5)$$

$$\lambda_i \left(\|\mathfrak{D}_i \mathbf{x}\|^2 - a_i \right) = 0, \quad i = 0, \dots, L \quad (5.2.6)$$

$$\lambda_i \geq 0, \quad i = 0, \dots, L. \quad (5.2.7)$$

However, if $\lambda_i = 0$, with $i = 0, \dots, L$, from (5.2.5) it follows that $\mathbf{x} = \mathbf{q}$, which is infeasible since the inequality constraints are not satisfied. Hence, at least one of λ_i , $i = 0, \dots, L$, must be non null and from (5.2.6) it results that at least one of the inequality constraints is active. Eventually, solving (5.2.5) we get

$$\mathbf{x} = \left(\mathbf{I} + \sum_{i=0}^L \lambda_i \mathfrak{D}_i^T \mathfrak{D}_i \right)^{-1} \mathbf{q} \quad (5.2.8)$$

where \mathbf{I} is the $n \times n$ identity matrix and $\lambda_0, \dots, \lambda_L$ are nonnegative parameters functions of a_0, \dots, a_L .

Note that in (5.2.8) the inverse exists for any $\lambda_i \geq 0$ and when $\lambda_i = 0$, for $i = 0, \dots, L$, no smoothing is performed. It is interesting that the solution to (5.2.3) is a linear operator acting on \mathbf{q} . Moreover, the $L + 1$ parameters λ_i control the degree of smoothing applied to each of the $L + 1$ segments of \mathbf{q} . In particular,

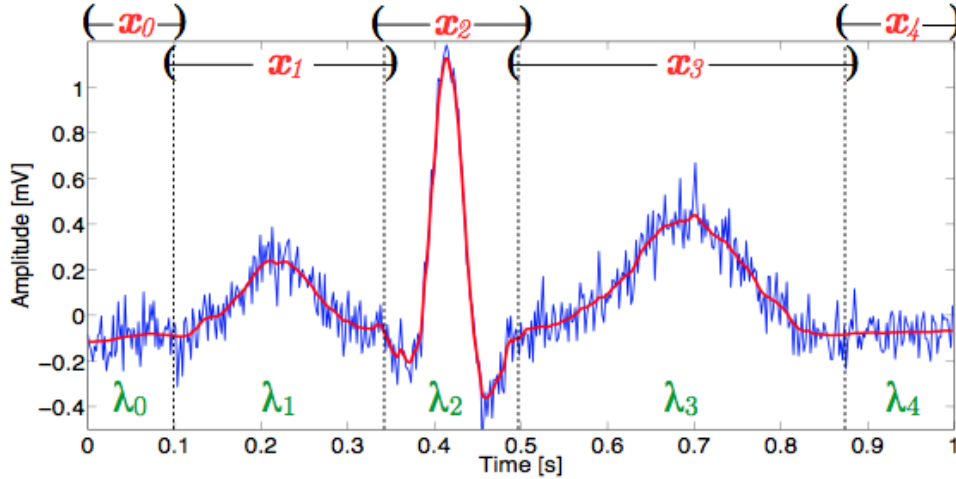


Figure 5.2.2: Smoothing of an ECG beat by local quadratic variation reduction: noisy (blue) and smoothed (red) signals.

even though $\lambda_0, \dots, \lambda_L$ interact, λ_i mainly controls the quadratic variation of the segment $\mathbf{x}(k_i, k_{i+1})$.

As a consequence, we do not need to know in advance the appropriate value of a_i in (5.2.3), as smoothing can be performed according to (5.2.8) where the parameters λ_i , for $i = 0, \dots, L$, control the degree of smoothness, i.e., the quadratic variation, of each portion of the solution. These parameters are related to the values of a_i in (5.2.3). In this way, smoothing can be performed without caring about a_i , by reducing locally the quadratic variation of the solution to the desired levels. The controlling parameters λ_i can be adapted to meet some performance criteria. For example, considering the SNR gain, i.e., the ratio between the SNR after and before smoothing, as a performance index, the optimal values for λ_i , $i = 0, \dots, L$, can be found as the ones that entail the maximum SNR gain. However, different figures of merit can be chosen, according to the peculiarity of the problem.

Figure (5.2.2) shows an example of application of smoothing by (5.2.8) on an ECG beat. In this example $L = 4$ since the ECG has been divided into 5 regions: isoelectric TP segment, P-wave, QRS complex, T-wave, and isoelectric TP segment. \mathbf{x}_i and λ_i represent the corresponding smoothed subvectors and smoothing parameters, respectively. In this regard, it is worthwhile noting that the approach

is well suited for signals with periodic, or pseudoperiodic, structure, such as ECG. In this case, homologous portions, i.e., exhibiting analogous local SNRs, share the same value for the corresponding smoothing parameters. As a consequence, the number of independent parameters reduces and few parameters control the degree of smoothing. In the case of Figure (5.2.2), this corresponds to setting $\lambda_0 = \lambda_4$ and, possibly, $\lambda_1 = \lambda_3$.

5.2.3 Computational issues

The smoothing operation (5.2.8) involves matrix inversion. So, computational aspects become important, especially if the size of vector \mathbf{q} is large enough, as is the case of entire ECG records. In this case, the computational burden, both in terms of time and memory, and the accuracy may become serious issues, even for batch processing. In this regard, the proposed algorithm behaves favorably.

Smoothing through (5.2.8) amounts to solve a linear system where the coefficient matrix, namely $\left(\mathbf{I} + \sum_{i=0}^L \lambda_i \mathfrak{D}_i^T \mathfrak{D}_i\right)$, is tridiagonal [64]. Tridiagonal systems can be solved efficiently with $O(n)$ operations [69], being n the number of unknowns. As a consequence, smoothing using (5.2.8) can be performed with complexity $O(n)$, i.e., *linear* in the size of vector \mathbf{q} , *regardless* of the value of L . Just to give an idea of how fast our algorithm is, a MATLAB (ver. 7.11) implementation of (5.2.8) with $L = 10^3$ running over a PC equipped with 2.3 GHz Core i5 processor takes about 0.73 s to smooth a record of 10^7 double precision floating point samples, which correspond to an ECG ~ 5.5 hours long, sampled at 512 Hz.

This property makes the proposed algorithm suitable also for real-time applications and for applications on handheld devices with reduced computing power, such as smartphones or tablets. This may be very important in depressed areas of less-developed countries, where, due to a lack of adequate primary care capacity, ECG is recorded under not ideal conditions, with low-cost recorders, i.e., more sensitive to artifacts and noise, and often by untrained people. Then, ECG is transferred from compact and inexpensive battery-powered acquisition devices to mobile phones and relayed for interpretation to experts, usually located in urban hospitals. The availability of such a fast tool for the smoothing of ECG records would provide an instantaneous feedback about recording quality to untrained operators, thus prompting them to make adjustments in recording data, e.g., prepare

skin more adequately, correct the position of electrodes, and improve electrodes contact. As a consequence, only diagnostically useful high-quality recordings would be sent to experts, thus facilitating their work and avoiding the risk of saturating their capacity.

5.3 Simulation results

In the following simulations, ECG delineation was accomplished manually: segments including P-waves, QRS complexes, T-waves, and isoelectric levels were roughly determined by visual inspection. No accurate delineation is required, as the proposed smoothing algorithm proved to be robust in this regard. Thus, segmentation is not a critical task for subsequent smoothing by our algorithm and can be implemented without extreme accuracy also in noisy recordings. Automatic tools [19, 96] for ECG segmentation may be used, too.

We adopt the following nomenclature for smoothing parameters λ_i in (5.2.8): λ_P , λ_{QRS} , λ_T , and λ_{iso} denote the parameters controlling the degree of smoothing for P-waves, QRS complexes, T-waves and isoelectric segments, respectively. When required, we denote by λ_Q , λ_R and λ_S the corresponding parameters for Q-waves, R peaks, and S-waves.

It is worthwhile noting that values of parameters λ_i are related and tend to have approximately a constant ratio. In our simulations, both on real and simulated data, we found the following empirical relations holding for a wide range of SNRs

$$\lambda_{iso} \simeq 8\lambda_P, \lambda_T \simeq \lambda_P, \lambda_S \simeq 0.2\lambda_P, \lambda_Q \simeq \lambda_S. \quad (5.3.1)$$

Relations (5.3.1) allow us to reduce the number of smoothing parameters for ECG to one or two. It is remarkable that even without optimization the smoothing performance is significant, as simulation results will show.

The performance of the proposed algorithm has been investigated both on real and simulated ECG traces.

As for real signals, we considered ECG traces from the MIT-BIH Normal Sinus Rhythm Database [97] available on Physionet [19]. This database includes 18 long-term ECG recordings of subjects with no significant arrhythmias. Signals were acquired at a sampling frequency of 128Hz with 12-bit resolution. Fig-

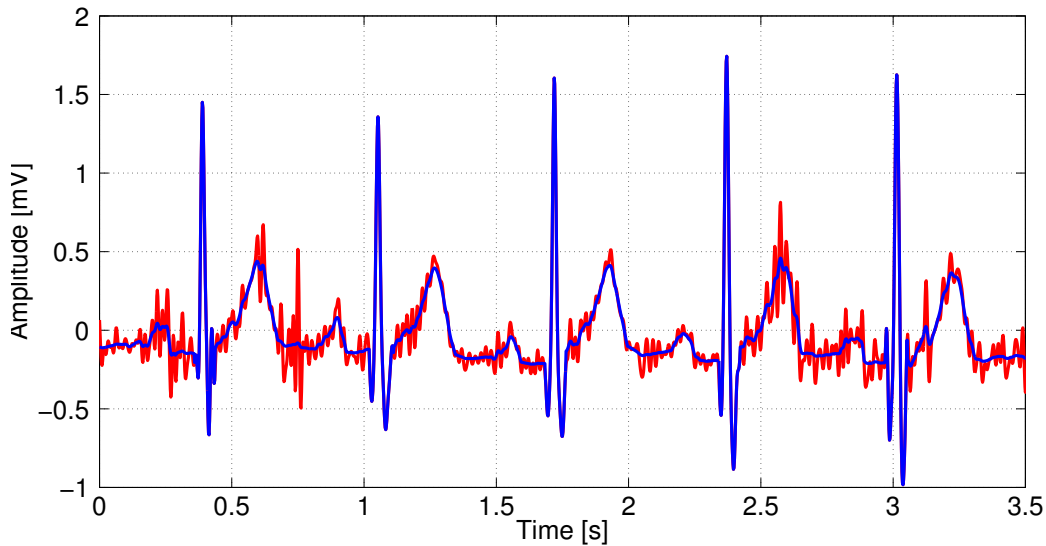


Figure 5.3.1: ECG record nsrdb/16483 from the MIT-BIH Normal Sinus Rhythm Database [97]: noisy (red) and smoothed (blue) by local quadratic variation reduction [5].

Figure 5.3.1 shows a 3.5 s segment of the record nsrdb/16483 affected by thermal and electromyographic noise (red curve) and the same record after denoising by local quadratic variation reduction (blue curve). In this case, local quadratic variation reduction was applied to the following segments: isoelectric TP and PQ segments, P-waves and T-waves, and QRS complexes. The corresponding degrees of smoothing were: $\lambda_{\text{iso}} = 8\lambda_{\text{P}}$, $\lambda_{\text{T}} = \lambda_{\text{P}} = 30$, and $\lambda_{\text{QRS}} = 0$, i.e., no smoothing for QRS complexes. A visual and qualitative comparison of the two curves highlights how local quadratic variation reduction technique managed to smooth the ECG signal. Although the values of the smoothing parameters were chosen merely by visual inspection, without any optimization, undesired noise was removed without any visible distortion of the original signal.

For a quantitative assessment of performance of the proposed algorithm, we considered a synthetic ECG signal corrupted by noise. The synthetic noiseless ECG record, denoted by q_0 , was generated according to the model described in [79], setting the sampling frequency to 512 Hz and the heart rate to 60 bpm. The record lasts 15 s and its bandwidth essentially does not exceed 40 Hz. The first 5 s

of \mathbf{q}_0 are reported in Figure 5.3.2 (blue curve).

The noiseless ECG \mathbf{q}_0 has been corrupted by additive noise, denoted by \mathbf{w} , where the components of \mathbf{w} are independent identically distributed zero mean Gaussian random variables with variance σ_w^2 . Thus, the corresponding noisy ECG signal is

$$\mathbf{q} = \mathbf{q}_0 + \mathbf{w}.$$

Figure 5.3.2 reports the noiseless ECG record \mathbf{q}_0 (blue) and its noisy version \mathbf{q} (red curve), corrupted by additive Gaussian noise with $\text{SNR}_0 = 0$ dB.

To quantify performance, the following quantities have been considered:

- the signal-to-noise ratio before smoothing:

$$\text{SNR}_0 = \frac{\|\mathbf{q}_0\|^2}{n \cdot \sigma_w^2}$$

where n is the size of vector \mathbf{q}_0 ;

- the signal-to-noise ratio after smoothing

$$\text{SNR}_s = \frac{\|\mathbf{q}_0\|^2}{\|\mathbf{x} - \mathbf{q}_0\|^2}$$

where $(\mathbf{x} - \mathbf{q}_0)$ is the error vector with respect to the reference ECG record \mathbf{q}_0 . Here, we consider as noise affecting the smoothed vector \mathbf{x} both the residual noise and the reconstruction error.

Performance is measured in terms of SNR gain, defined as

$$G_{\text{SNR}} = \frac{\text{SNR}_s}{\text{SNR}_0} = \frac{n \cdot \sigma_w^2}{\|\mathbf{x} - \mathbf{q}_0\|^2}.$$

In the following two simulations, local quadratic variation reduction was applied to the following segments: isoelectric TP, PQ and ST segments, P-waves and T-waves, Q-waves and S-waves, and R peaks. The corresponding degrees of smoothing were: $\lambda_{\text{iso}} = 8\lambda_P$, $\lambda_Q = \lambda_S = 0.2\lambda_P$, $\lambda_T = \lambda_P$, $\lambda_R = 5, 4, 3, 2, 1$ for SNR_0 in dB in the ranges $[-15, 10)$, $[-10, -5)$, $[-5, 5)$, $[5, 15)$, $[15, 30)$, respectively. The value for λ_P was chosen as the one that entails the maximum SNR

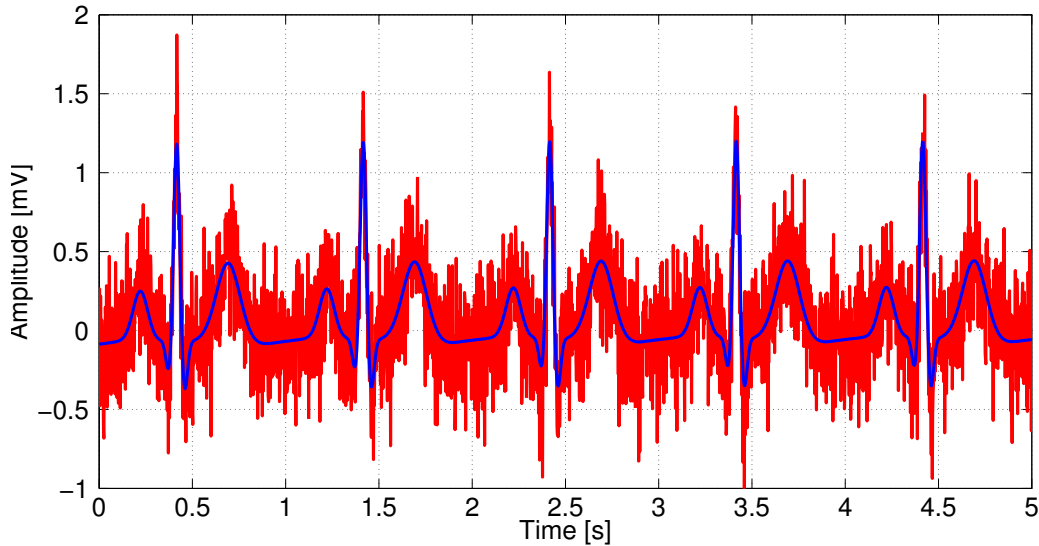


Figure 5.3.2: ECG record simulated according to the model in [79]: noiseless reference (blue) and noisy record (red) corrupted by additive Gaussian noise with $\text{SNR}_0 = 0\text{ dB}$.

gain. This choice is motivated by the need to determine the limit performance of the proposed algorithm.

In Figure 5.3.3 the first 5 s of both the smoothed vector \mathbf{x} (red) and the reference ECG \mathbf{q}_0 (blue) are plotted together for ease of comparison. Note that in this case the SNR before smoothing is quite low, nevertheless the proposed algorithm is very effective in denoising \mathbf{q} , as Figure 5.3.3 highlights. The two curves almost overlap and the SNR gain in this case is as high as $G_{\text{SNR}} = 14.5\text{ dB}$.

To evaluate how gain varies as input SNR changes, we report in Figure 5.3.4 the average SNR gain versus input SNR, when the reference ECG record \mathbf{q}_0 is corrupted by additive Gaussian noise with SNR ranging from -15 dB to 30 dB . The top axis in Figure 5.3.4 represents the in-band SNR, which is computed using the 40Hz bandwidth of the reference ECG record. The in-band SNR is about⁴ 8.1 dB greater than the corresponding input SNR. For each input SNR we averaged the gain G_{SNR} over 100 noise realizations. As Figure 5.3.4 highlights, the proposed

⁴Actually it is $10\log(6.4)\text{ dB} \approx 8.1\text{ dB}$, where 6.4 is the ratio between half of the sampling frequency and bandwidth of the reference ECG record.

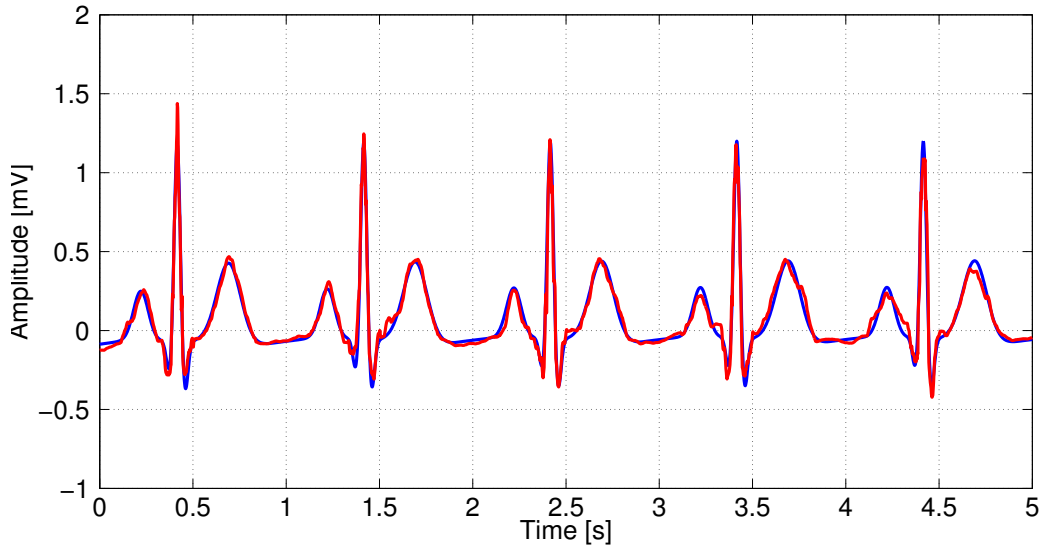


Figure 5.3.3: Noiseless reference ECG q_0 (blue) from Figure 5.3.2 and smoothed ECG x (red) by local quadratic variation reduction [5].

algorithm is very effective in smoothing ECG signals and achieves considerable gain over the whole range of practical input SNRs.

It is worth noting that the proposed algorithm is able to reject both out-of-band and in-band noise. In this regard, low-pass filtering cannot reject in-band noise without altering the signal. Indeed, an ideal 40Hz low-pass filter, in the same setting of our simulation, would exhibit a constant average gain of about 8.1 dB as a result of the rejection of the sole out-of-band noise. This is confirmed by simulations where we considered a linear-phase FIR low-pass filter synthesized applying the window method [68] to an ideal 40Hz low-pass filter, using a Kaiser window and requiring 0.1 dB ripple in passband and 80dB attenuation in stopband. In Figure 5.3.4 we report the filter SNR gain versus input SNR, averaged over the same 100 noise realizations used before. Figure 5.3.4 highlights the effectiveness of the smoothing algorithm, which outperforms low-pass filtering for all values of SNR. Note that high-pass filtering is the standard approach to ECG denoising currently implemented in all electrocardiographic devices [16, 20, 25, 98, 99].

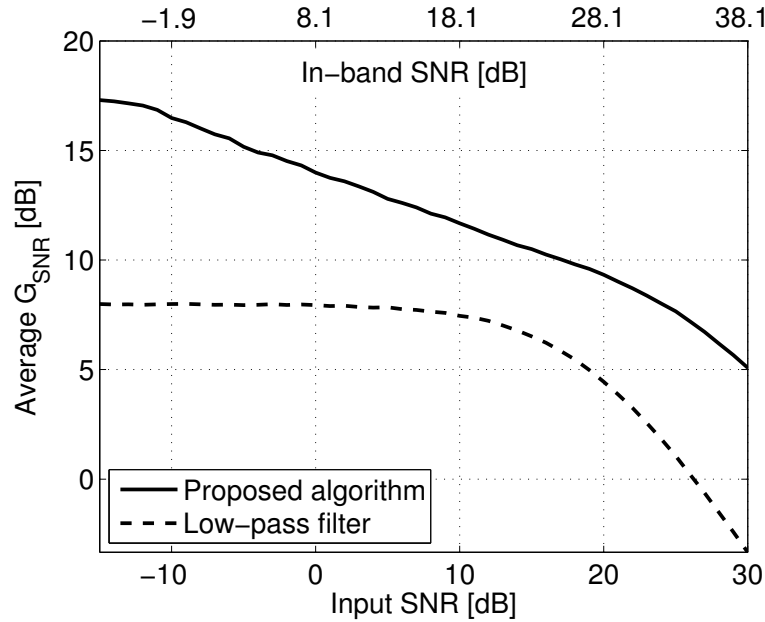


Figure 5.3.4: SNR gain G_{SNR} versus input SNR (bottom axis) and in-band SNR (top axis). Gain has been averaged over 100 realizations of noise [5].

5.4 Conclusions

In this chapter, a novel approach to smoothing heavily corrupted ECG traces has been presented. Denoising of ECG is effective if the local structure of the ECG is explicitly taken into account in the smoothing operation. Indeed, different portions of a noisy ECG exhibit different local SNRs. As a consequence, smoothing and denoising can be performed by locally reducing the variability of ECG. Considering the quadratic variation as a suitable index of variability for vectors or sampled functions, we achieve smoothing by locally reducing the quadratic variation of different portions of a noisy ECG by an amount that is inversely related to the local SNR. The algorithm is the closed-form solution to a constrained convex optimization problem, where local quadratic variations of different portions of ECG enter as constraints. Simulation results confirm the effectiveness of the approach and highlight its ability to remove noise and artifacts from ECG traces. Quantitative assessment of performance shows that the approach outperforms low-pass filtering for all values of SNR. Moreover, it is able to reject both

in-band and out-of-band noise. The computational complexity of the algorithm is *linear* in the size of the record to smooth. This makes it particularly suitable for real-time applications and for applications on handheld devices with reduced computing power, such as smartphones or tablets.

Eventually, it is worthwhile noting that the algorithm is particularly suited for signals with periodic, or pseudoperiodic, structure. Indeed, in this case only few parameters control the degree of smoothing. However, the rationale and the formulation behind it have general validity and do not depend on the nature of the signal to process. Thus, the approach can be effectively applied to the broader class of bioelectrical signals. In this regard, preliminary results of its application to TMS-EEG records are encouraging.

Chapter 6

Joint smoothing and narrowband artifacts rejection for ECG records

Narrowband artifacts, such as power-line interference, are a common kind of noise affecting ECG recordings. Their effect is the introduction of further variability in the signal. Thus, they can be removed using the algorithm for ECG smoothing described in the previous chapter. However, a joint approach that combines denoising and narrowband artifacts rejection has proven to be more effective in this regard. This is pursued in this chapter, where smoothing and narrowband artifacts rejection are performed jointly, solving a constrained convex optimization problem. The optimization problem combines the local characteristics of the ECG and the spectral localization of the artifacts to reject. The local quadratic variation of different portions of the noisy ECG and the energy content of harmonic artifacts enter as constraints in the problem. The computational complexity ranges from $O(n)$ to $O(n \log n)$, being n the length of the record to smooth. Simulation results confirm the effectiveness of the approach and highlight its ability to remove both noise and narrowband artifacts in ECG signals.

6.1 Introduction

Narrowband artifacts, which include harmonic artifacts and power-line interference, are a common kind of noise affecting ECG recordings. Hence, artifacts suppression is an unavoidable step in any preprocessing of ECG signal. Details

about causes originating them are provided in Section (4.1).

Customarily, noise reduction and artifacts rejection from ECG records are tackled as two distinct problems. Classical approaches resort to linear time-invariant filters, whether low-pass to attenuate noise, or notch to remove harmonic artifacts [16, 22, 25]. However, low-pass filtering cannot remove in-band noise due to muscle activity, nor accommodate the non-stationary nature of cardiac signals [22]. Moreover, harmonic artifacts in general represent an in-band noise for ECG signal and their amplitude and phase are time-varying. Hence, on the one hand, the suppression band of the notch filter should be as narrow as possible in order to minimize distortions in the filtered signal; on the other hand, a narrow stopband may lead to ineffective filtering of artifacts since it may be unable to track slow variations around the fundamental and its harmonics. To overcome these limitations, adaptive filtering has been proposed both for noise [74, 80] and power-line cancellation [74, 75]. Furthermore, wavelet decomposition was proposed for ECG denoising [81, 83, 100] and power-line interference removal [100]. Further approaches resort to empirical mode decomposition [93], mathematical morphology [86], and independent component analysis [91].

In the previous chapter we have described a novel approach to smoothing and denoising ECG records that keeps into account the local structure of ECG signal. Its effectiveness reduces when it is used to reject multiple harmonic artifacts. To overcome this limitation, in this chapter we propose a *joint* approach to denoising and narrowband artifacts rejection that exploits the narrowband nature of the artifacts [6, 7].

The chapter is organized as follows. The rationale behind the proposed approach is described in Subsection 6.2.1. The smoothing algorithm is derived in Subsection 6.2.2. Sections 6.3 and 6.4 follow with simulation results and conclusions.

6.2 Proposed approach

6.2.1 Rationale

In the previous chapter, we have proposed a novel algorithm for smoothing and denoising ECG records. It is based on the idea that the effect of noise and artifacts

on ECG is to introduce additional “variability” into the measured record, with respect to the true one. The amount of additional “variability” is time-varying, since signal morphology changes over time, and noise and artifacts can be persistent, like thermal noise, or transient, like electromyographic noise. As a consequence, different portions of a noisy ECG exhibit different local SNRs, where local SNR is the SNR computed on a portion of the signal. Considering the quadratic variation as a suitable measure of variability, in Section 5.2 we achieve smoothing of ECG by reducing the local quadratic variation of different portions of a noisy ECG by an amount that is inversely related to the local SNR.

The effect of narrowband artifacts, such as power-line interference, is the introduction of further variability in ECG. Thus, they can be removed using the smoothing algorithm (5.2.8) presented in Subsection 5.2.2. However, we showed in Subsection 4.2.2 that low-frequency harmonic artifacts tend to be less attenuated in response to a quadratic variation reduction. A joint approach that combines denoising and tailored narrowband artifacts rejection proves to be more effective in this regard. To this end, the amount of narrowband artifacts has been quantified in Subsection 4.2.3 through their energy content. Thus, we achieve joint ECG denoising and narrowband artifacts rejection by exploiting local quadratic variation reduction in conjunction with an additional requirement: to make negligible the energy content of narrowband artifacts in the denoised signal [6, 7].

6.2.2 Smoothing ECG signals

In the following $\mathbf{q} \in \mathbb{R}^n$ is the measured ECG, which is affected by noise and artifacts, and \mathbf{x} the corresponding vector after smoothing. The idea is to perform smoothing, meant as combined denoising and artifacts rejection, by *jointly* reducing the local quadratic variation of different segments of the measured ECG and the energy content of narrowband artifacts.

Let the vector \mathbf{q} be decomposed into $L + 1$ segments

$$\mathbf{q}(k_i, k_{i+1}) = [q_{k_i} \cdots q_{k_{i+1}}]^T, \text{ for } i = 0, \dots, L \quad (6.2.1)$$

with $0 \leq L \leq n - 1$ and $1 = k_0 < k_1 < \cdots < k_L < k_{L+1} = n$. Segments in (6.2.1) denote distinct portions of the ECG exhibiting different local SNRs, like QRS complexes, P-waves or T-waves, as depicted in Figure 5.2.2. Note that two con-

secutive segments overlap. This choice guarantees the absence of abrupt changes in the smoothed vector \mathbf{x} .

Following the line of reasoning outlined above, denoising and narrowband artifacts rejection can be recast as the following convex optimization problem

$$\begin{cases} \underset{\mathbf{x} \in \mathbb{R}^n}{\text{minimize}} & \|\mathbf{x} - \mathbf{q}\|^2 \\ \text{subject to} & [\mathbf{x}(k_i, k_{i+1})] \leq a_i, \quad i = 0, \dots, L \\ & \mathcal{E}_a \leq b \end{cases} \quad (6.2.2)$$

where $[\mathbf{x}(k_i, k_{i+1})]$ denotes the local quadratic variation (5.2.1) of $\mathbf{x}(k_i, k_{i+1})$, \mathcal{E}_a has been defined in (4.2.2) to quantify the energy content of narrowband artifacts, a_0, \dots, a_L are positive constants controlling the degree of smoothness applied to each segment $\mathbf{q}(k_i, k_{i+1})$, and b is a positive constant controlling the degree of rejection of narrowband artifacts [7]. We do not need to know in advance the appropriate values for a_i and b in any particular problem, as will be shown later.

Problem (6.2.2) is a convex optimization problem, since both the objective function and the inequality constraints are convex. As a consequence, any locally optimal point is also globally optimal and Karush- Kuhn-Tucker (KKT) conditions provide necessary and sufficient conditions for optimality [65]. Moreover, since the objective function is strictly convex and the problem is feasible, the solution exists and is unique. The Lagrangian is

$$\mathcal{L}(\mathbf{x}, \lambda_0, \dots, \lambda_L, \nu) = \|\mathbf{x} - \mathbf{q}\|^2 + \sum_{i=0}^L \lambda_i \left(\|\mathcal{D}_i \mathbf{x}\|^2 - a_i \right) + \nu \left(\|\tilde{\mathbf{W}} \mathbf{x}\|^2 - b \right)$$

where \mathcal{D}_i has been defined in (5.2.4) and $\tilde{\mathbf{W}}$ in Subsection (4.2.3). From the KKT conditions we get

$$\lambda_i \left(\|\mathcal{D}_i \mathbf{x}\|^2 - a_i \right) = 0, \quad i = 0, \dots, L, \quad (6.2.3)$$

$$\nu \left(\|\tilde{\mathbf{W}} \mathbf{x}\|^2 - b \right) = 0, \quad (6.2.4)$$

$$\nabla \mathcal{L}(\mathbf{x}, \lambda_0, \dots, \lambda_L, \nu) = 2(\mathbf{x} - \mathbf{q}) + 2 \sum_{i=0}^L \lambda_i \mathcal{D}_i^T \mathcal{D}_i \mathbf{x} + 2\nu \tilde{\mathbf{W}}^H \tilde{\mathbf{W}} \mathbf{x} = 0 \quad (6.2.5)$$

and the nonnegativity of the Lagrange multipliers, i.e., $\mathbf{v} \geq 0$ and $\lambda_i \geq 0$, with $i = 0, \dots, L$. From (6.2.5) it results that at least one of the Lagrange multipliers λ_i and \mathbf{v} must be non null, otherwise $\mathbf{x} = \mathbf{q}$ and no smoothing is performed. Hence, from (6.2.3) and (6.2.4) at least one of the inequality constraints must be active. Solving (6.2.5) we get

$$\mathbf{x} = \left(\mathbf{I} + \sum_{i=0}^L \lambda_i \mathfrak{D}_i^T \mathfrak{D}_i + \mathbf{v} \text{Re} \left\{ \tilde{\mathbf{W}}^H \tilde{\mathbf{W}} \right\} \right)^{-1} \mathbf{q} \quad (6.2.6)$$

where \mathbf{I} denotes the identity matrix [7]. The parameters $\lambda_0, \dots, \lambda_L$ and \mathbf{v} are functions of a_0, \dots, a_L and b in (6.2.2), but are used in their place to control the solution (6.2.6). Smoothing can be performed without caring about a_i and b , by adapting λ_i and \mathbf{v} in (6.2.6) to meet some performance criteria. For example, the optimal values for λ_i and \mathbf{v} can be found as those that entail the maximum gain on signal-to-noise-and-interference ratio (SNIR), i.e., the ratio between the SNIR after and before smoothing. It is worthwhile to remark that, even though $\lambda_0, \dots, \lambda_L$ and \mathbf{v} interact, λ_i mainly controls the quadratic variation of the segment $\mathbf{x}(k_i, k_{i+1})$, whereas \mathbf{v} mainly controls the degree of rejection of narrowband artifacts.

Finally, some remarks on computational aspects, since matrix inversion is involved in (6.2.6). Let us denote by n the size of \mathbf{q} . In the general case $\lambda_i > 0$ and $\mathbf{v} > 0$, it is possible to prove that smoothing through (6.2.6) can be performed with complexity $O(n \log n)$ using the conjugate gradient method [101]. Indeed, such method does not require the storage of the matrix to be inverted but requires only the computation of the product between the matrix and a vector. Moreover, in our case convergence to the solution is achieved in few steps. Thus, the computational complexity of (6.2.6) is determined by the computation of the product between the matrix $\tilde{\mathbf{W}}$ and a vector, which can be performed through the FFT with complexity $O(n \log n)$. Finally, when $\lambda_i = 0$, for $i = 0, \dots, L$ and $\mathbf{v} > 0$, the complexity is still $O(n \log n)$, but the solution can be achieved by direct methods. When $\mathbf{v} = 0$, (6.2.6) is solved efficiently by direct methods with complexity $O(n)$ regardless of L , as detailed in Chapter (5).

6.3 Simulation results

The performance of the proposed algorithm has been investigated both on real and synthetic ECG signals. In all simulations, ECG delineation was performed manually: the different segments were roughly determined by visual inspection. No accurate delineation is required, as the proposed algorithm proved to be robust in this regard. Thus, segmentation is not a critical task for subsequent smoothing by our algorithm and can be implemented without extreme accuracy also in noisy recordings. Automatic tools for ECG segmentation may be used, too.

Regarding real signals, in Figure 6.3.1 we report a portion of a noisy ECG \mathbf{q} (red) from ambulatory recording, which is strongly affected by noise and narrow-band artifacts centered at 50Hz and 100Hz (plus higher harmonics), due to power-line noise. The signal was acquired with a sampling frequency of 512Hz and with 16-bit resolution. In the same figure we report the corresponding smoothed signal \mathbf{x} (blue) resulting from joint denoising and narrowband artifacts rejection. Within each beat local quadratic variation reduction has been applied to P-wave, QRS complex, T-wave, and isoelectric TP, PQ, and ST segments. We denote the corresponding parameters by λ_P , λ_{QRS} , λ_T , and λ_{iso} , respectively. Their value have been set according to relations (5.3.1), setting $\lambda_{iso} = 8\lambda_P$, $\lambda_T = \lambda_P$, and $\lambda_{QRS} = 0.2\lambda_P$. Thus, the independent parameters reduce to λ_P and ν , which have been roughly set to $\lambda_P = 90$ and $\nu = 10^4$ without any optimization. As Figure 6.3.1 highlights, the proposed approach managed to effectively smooth the noisy ECG, although it was highly corrupted, and neither optimization in the choice of the smoothing parameters nor accurate ECG segmentation were performed.

In order to provide quantitative evaluation of performances, we tested the proposed algorithm on synthetic ECG signals corrupted by noise and harmonic artifacts. A synthetic noiseless ECG record, denoted by \mathbf{q}_0 , was generated according to the model described in [79], setting the sampling frequency to 512Hz and the heart rate to 75bpm. The bandwidth of \mathbf{q}_0 essentially does not exceed 40Hz. The noiseless ECG \mathbf{q}_0 was corrupted by additive noise, denoted by \mathbf{w} , which is a zero-mean Gaussian random vector with independent components having variance σ_w^2 such that $\text{SNR} = 10\log \frac{\|\mathbf{q}_0\|^2}{n \cdot \sigma_w^2} = 5\text{dB}$, being n the length of \mathbf{q}_0 . In addition, \mathbf{q}_0 was corrupted by harmonic artifacts, denoted by \mathbf{d} , which consist of three sine waves with random phases and frequencies 30Hz, 60Hz and 120Hz,

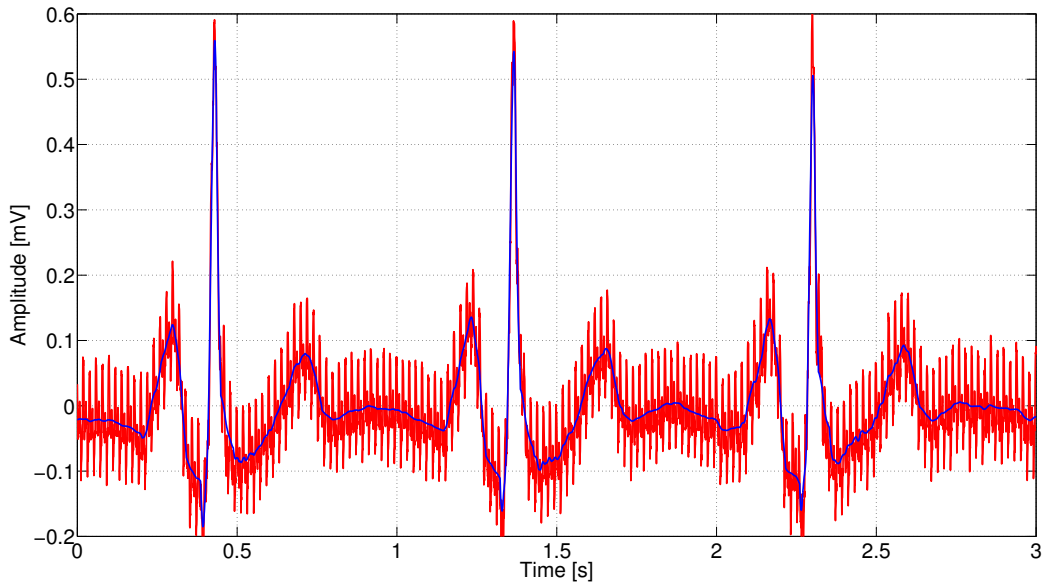


Figure 6.3.1: ECG from real data: noisy ECG \mathbf{q} (red) and smoothed ECG \mathbf{x} (blue) using the proposed algorithm [7].

respectively. The corresponding amplitudes, namely A_{30} , A_{60} and A_{120} , are in the ratio $A_{30}/A_{60} = A_{60}/A_{120} = 2$ and are such that the corresponding signal-to-interference ratio $\text{SIR} = 10 \log \frac{\|\mathbf{q}_0\|^2}{\|\mathbf{d}\|^2} = 0 \text{ dB}$. The sine waves at 60Hz and 120Hz account for the first and second harmonics of the power-line noise, whereas the sine wave at 30Hz models a strong in-band harmonic interference.

The resulting ECG corrupted by noise and artifacts is $\mathbf{q} = \mathbf{q}_0 + \mathbf{w} + \mathbf{d}$, and is characterized by a signal-to-noise-plus-interference ratio

$$\text{SNIR}_0 = 10 \log \frac{\|\mathbf{q}_0\|^2}{\|\mathbf{w} + \mathbf{d}\|^2} = -1.3 \text{ dB}.$$

Note that \mathbf{q} is highly corrupted. Figure 6.3.2 reports a segment of \mathbf{q} (red) together with the corresponding noiseless reference ECG \mathbf{q}_0 (blue).

Performance is measured in terms of SNIR gain

$$G_{\text{SNIR}} = \text{SNIR}_s - \text{SNIR}_0 = 10 \log \frac{\|\mathbf{w} + \mathbf{d}\|^2}{\|\mathbf{x} - \mathbf{q}_0\|^2}$$

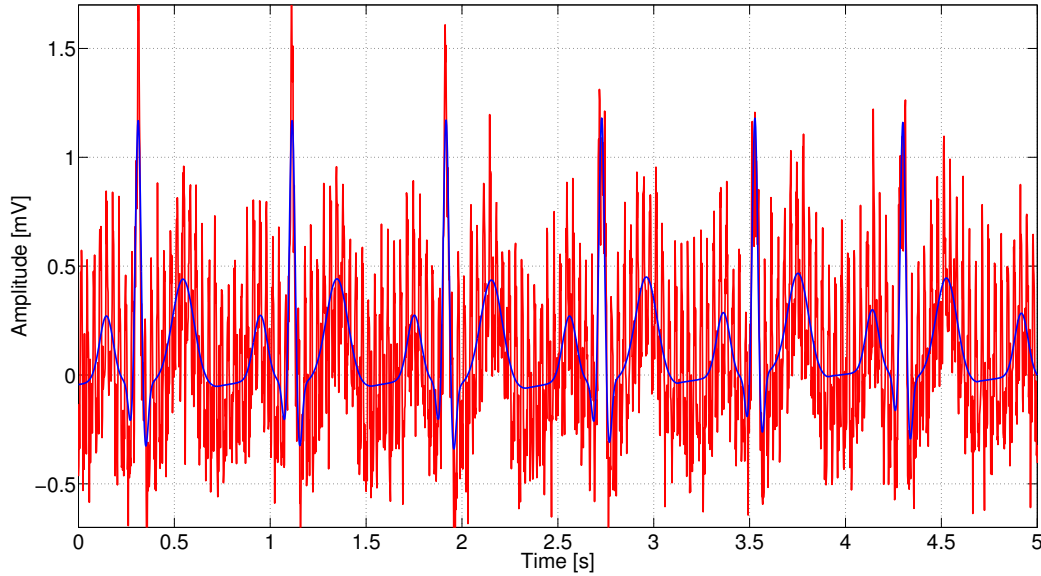


Figure 6.3.2: Synthetic ECG: noiseless reference ECG \mathbf{q}_0 (blue) from the model in [79] and corrupted ECG \mathbf{q} (red), affected by noise and narrowband artifacts with $\text{SNIR}_0 = -1.3$ dB [7].

where $\text{SNIR}_s = 10 \log \frac{\|\mathbf{q}_0\|^2}{\|\mathbf{x} - \mathbf{q}_0\|^2}$ is the signal-to-noise-plus-interference ratio after smoothing. By $(\mathbf{x} - \mathbf{q}_0)$ we regard as noise affecting \mathbf{x} both the residual noise and the reconstruction error.

In Figure 6.3.3 we report in blue the reference ECG \mathbf{q}_0 and in red the record smoothed by the algorithm in the previous chapter, i.e., $\mathbf{v} = 0$ in (6.2.6). Smoothing was applied with different smoothing parameters to the following segments: isoelectric PQ, ST and TP segments (λ_{iso}), P-waves (λ_{P}), Q-waves (λ_{Q}), R peaks (λ_{R}), S-waves (λ_{S}), and T-waves (λ_{T}). The corresponding smoothing parameters were: $\lambda_{\text{iso}} = 8\lambda_{\text{P}}$, $\lambda_{\text{Q}} = \lambda_{\text{S}} = 0.2\lambda_{\text{P}}$, $\lambda_{\text{R}} = 3$, and $\lambda_{\text{T}} = \lambda_{\text{P}} = 60$, according to (5.3.1). The value for λ_{P} has been coarsely set by visual inspection of the smoothed signal, without any optimization. It is remarkable that even without optimization the smoothing performance is significant, as Figure 6.3.3 shows. Indeed, for these realizations of noise and narrowband artifacts the gain is $G_{\text{SNIR}} = 13.5$ dB.

However, a residual oscillatory behavior is still present in $\tilde{\mathbf{x}}$. To suppress it, we

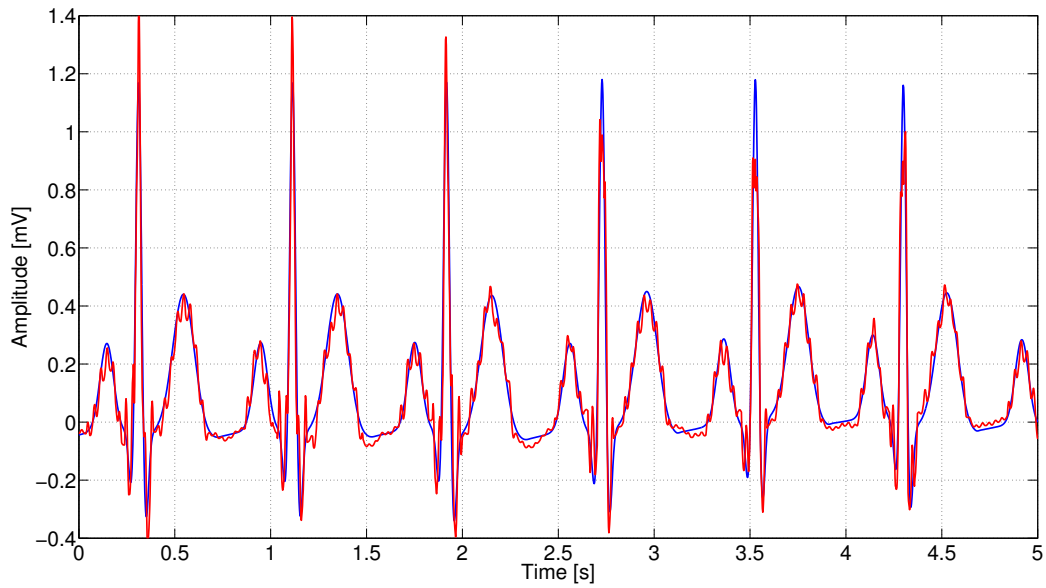


Figure 6.3.3: Reference ECG q_0 (blue) and reconstructed ECG \tilde{x} (red) setting $v = 0$ in (6.2.6). In this case, the gain is $G_{\text{SNIR}} = 13.5$ dB [7].

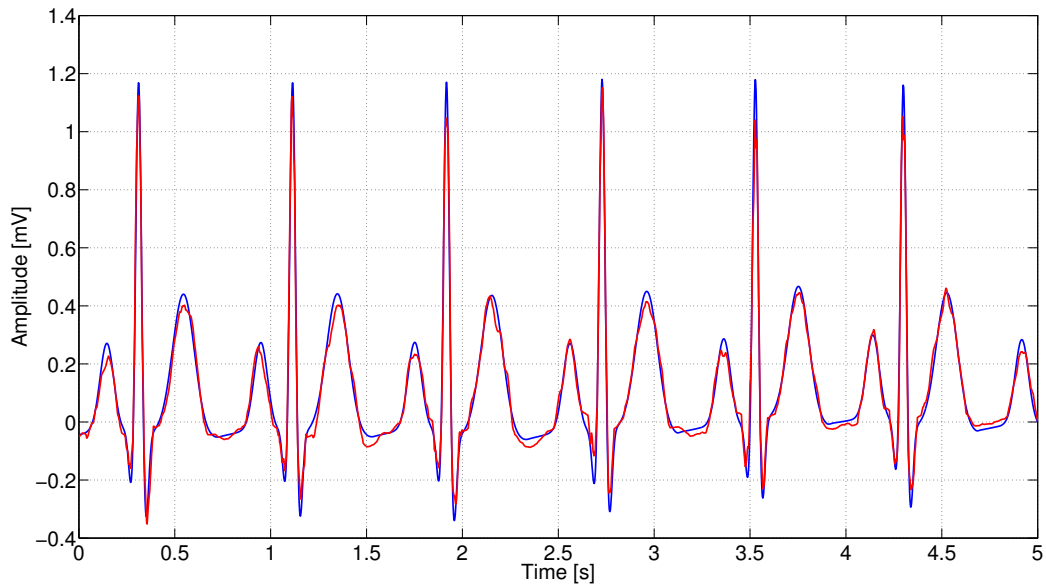


Figure 6.3.4: Reference ECG q_0 (blue) and smoothed ECG x (red) after joint denoising and artifacts rejection. The resulting gain is $G_{\text{SNIR}} = 19.6$ dB [7].

must consider the combined action of $\lambda_i > 0$, $i \in \{\text{iso}, \text{P}, \text{Q}, \text{R}, \text{S}, \text{T}\}$, and $\nu > 0$ in (6.2.6). This amounts to performing *joint* denoising and harmonic artifacts rejection on \mathbf{q} . In Figure 6.3.4 we compare the resulting smoothed ECG signal \mathbf{x} (red) and the noiseless ECG record \mathbf{q}_0 (blue) as reference. The smoothing parameters λ_i are the same as in Figure 6.3.3 and ν has been coarsely set to 10^3 , again without any optimization. As Figure 6.3.4 highlights, the proposed approach managed to effectively smooth the ECG signal. The corresponding SNIR gain is as high as $G_{\text{SNIR}} = 19.6\text{dB}$, thus entailing an additional 6.1 dB gain over the sole denoising of Figure 6.3.3.

6.4 Conclusions

In this chapter we have considered the problem of noise and narrowband artifacts removal in ECG signals. Narrowband artifacts include harmonic artifacts and power-line interference, which is ubiquitous in clinical environment. The proposed approach achieves denoising and narrowband artifacts rejection combining two actions: the local reduction of the quadratic variation of different segments of the ECG by an amount inversely related to the local SNR, and the global reduction of the energy content of narrowband artifacts. These actions are performed *jointly*. Numerical results confirm the effectiveness of the approach and highlight its ability to remove noise and artifacts in ECG signals. The computational complexity of the algorithm ranges from $O(n)$ to $O(n \log n)$ using the conjugate gradient method, being n the size of the vector to smooth. Finally, it is worthwhile noting that the proposed algorithm is not limited to ECG and can be effectively applied to a broader class of signals, since the rationale and the formulation behind it have general validity.

Chapter 7

ECG baseline wander removal preserving the ST segment

Baseline wander is a low-frequency additive noise affecting almost all bioelectrical signals. ECG is the worst affected in this regard, since baseline wander and ECG have overlapping bands. The in-band nature of baseline wander makes its removal difficult without affecting the ECG, in particular the ST segment. This is a portion of the ECG with high clinical relevance, as it is related to the diagnosis of acute coronary syndromes. The ST segment is highly susceptible to distortion when baseline removal is performed affecting the low-frequency region of ECG spectrum, where are concentrated the harmonic components that mainly contribute to the shape of the ST segment. In this chapter we propose to tackle the problem of baseline removal from a different perspective, considering the quadratic variation as an alternative measure of variability not directly related to the frequency domain. Baseline is estimated solving a constrained convex optimization problem where quadratic variation enters as a constraint. The solution depends on a single parameter whose value is not critical. The computational complexity of the algorithm is linear in the size of the vector to detrend. This makes it suitable for real-time applications as well as for applications on devices with reduced computing power, e.g., handheld devices. An efficient implementation of the algorithm is presented later in the chapter. Performances of the approach are extensively evaluated and compared to the state of the art. The approach is analyzed also in terms of distortions introduced in the ST segment. Moreover, overall

performance of our approach and competing algorithms is assessed, taking into account jointly effectiveness in removing baseline wander, distortion introduced in the ST segment and computational burden. Results show that quadratic variation reduction is the most effective and the fastest algorithm for baseline wander removal, among those effective in removing baseline drift. Eventually, the proposed algorithm is not limited to ECG signals, but can be effectively applied to a broader class of bioelectrical signals. In this regard, we have successfully applied it to EMG, EEG and EOG signals.

7.1 Introduction

Baseline wander is a particular kind of noise affecting almost all bioelectrical signals, ranging from electroencephalogram (EEG) [22,102] and magnetoencephalogram (MEG) [102], to electrooculogram (EOG) [20,103], electromyogram (EMG), either surface or needle EMG [104], and electrocardiogram (ECG) [16,22]. The sources of baseline wander may be different, but it always appears as a low-frequency artifact that introduces slow oscillations in the recorded signal.

In the following, we discuss the problem of baseline wander separately for the different bioelectrical signals. A special focus to ECG signals is provided and in Section 7.3 we report an exhaustive review of state-of-the-art approaches for ECG baseline wander removal.

EEG and MEG In EEG and MEG registrations, baseline can be due to brain activity, muscle tension, sweating, eye and head movement, electrode movement (in the case of EEG) or other noise sources [28,105]. In particular, baseline correction is a crucial task in the analysis of event-related activities measured in response to a time-locked stimulation, such as electric potentials recorded from the scalp with EEG, namely event-related potentials (ERPs), or magnetic fields measured close to the head through MEG, namely event-related fields (ERFs) [102]. Indeed, such a response is about 10-fold weaker than the spontaneous activity of the brain [22] and can be easily masked by noise. Moreover, stimuli are often presented at a relatively high rate so that the response to a previous stimulus has not extinguished at the moment of the current stimulus, resulting in an additional contribution to baseline [102]. Common approaches to baseline correction in ERP

and ERF analyses are: i) high-pass filtering [102, 106], ii) ensemble averaging of several trials [22], and iii) subtraction of the average over a pre-stimulus interval [107]. The respective limits are: i) baseline and ERP, or ERF, spectra overlap, ii) a large number of records is needed and some information is lost in the averaging, and, finally, iii) trends more complex than the constant cannot be removed.

EMG EMG signals are used in the assessment of muscles activity, acquired whether on skin surface (surface EMG, or sEMG) or with a needle inserted into the muscle (needle EMG, or nEMG) [108, 109]. Regardless of the acquisition method, EMG signals are affected by baseline fluctuations primarily due to electrical drifts in the acquisition equipment [22, 108, 110, 111]. Additionally, baseline drift is also caused by skin-electrode interface in sEMG [28, 109, 110], and by movements of the recording needle relative to the muscle and variation of skin potential induced by the needle in nEMG [111]. However, the main source of baseline fluctuations in EMG recordings is interference of adjacent muscle units different from the one under investigation [22, 111, 112]. Such a crosstalk phenomenon is more evident in sEMG records as nEMG provides a high-resolution localized description of muscle activity [22, 109]. The common approach to baseline fluctuations removal from EMG recordings is high-pass filtering [22, 113, 114]. Nevertheless, baseline drift and EMG spectra have overlapping bands in the low-frequency region of the spectrum [111, 114, 115]. For example, in [116, 117] the analysis of the low-frequency region of EMG spectrum was proposed to quantify fatigue undergone by certain muscles. Moreover, spectral content of baseline fluctuations is highly variable, depending on the muscle whose activity is recorded, the degree of muscle contraction, and the position of needle [111, 112]. This translates into a difficulty in selecting the appropriate cut-off frequency of the filter [110]. In this regard, several recommendations have been issued, but they all suggest the use of different cut-off frequencies [104, 110, 115, 118]. To overcome these limitations, several approaches have been proposed in the literature [111, 114].

ECG The main cause of baseline wander in ECG signals is respiration. Indeed, both the resistivity and position of the lungs change during respiration [119]. Moreover, the orientation and location of the heart change during the respiratory cycle, and certain cyclic changes occur in the measured electric heart vector as a

consequence of the respiration [119, 120]. Additional causes of baseline wander in ECG signals are perspiration, patient's body movements, skin-electrode interface, and varying impedance between electrodes and skin due to poor electrode contact [16, 18, 22, 28]. Baseline wander is *ubiquitous* in all electrocardiographic devices, thus its removal turns out to be an unavoidable step in any processing of ECG signals.

Among bioelectrical signals, ECG is the worst affected by baseline wander. Indeed, baseline wander in ECG is modeled as a low-frequency additive noise with band in the range $0 \div 0.8$ Hz that can extend up to 1 Hz, or even more, during stress tests [16, 22]. As a consequence, baseline wander and ECG have overlapping bands in the low-frequency region of the spectrum [121]. Unfortunately, distortion in this band of ECG spectrum negatively affects the shape of the ST segment, which is the portion connecting the QRS complex with the T-wave [14]. Details about the ST segment are provided in Section 7.2. Furthermore, the low-frequency region of ECG spectrum proved to be useful in detecting nightly events of obstructive sleep apnea [122, 123]. The in-band nature of baseline wander makes its removal difficult without affecting the ECG, thus spoiling relevant clinical information [29].

In this chapter we propose propose a novel approach to baseline wander estimation and removal for bioelectrical signals. The approach is based on the notion of *quadratic variation reduction* [9–12]. The quadratic variation has been introduced in Subsection 3.3.2 as a measure of variability for functions or sampled vectors, and we have proved that it is a consistent measure in this regard. The problem of baseline wander estimation is recast as a constrained convex optimization problem, where the quadratic variation enters as a constraint. Baseline is estimated searching for the signal closest to the observed one, but exhibiting *reduced quadratic variation*. Numerical results show that the approach effectively removes baseline wander and outperforms state-of-the-art algorithms [10, 12]. It compares favorably also in terms of computational complexity, which is *linear* in the size of the vector to detrend [12]. This makes it suitable for real-time applications as well as for applications on devices with reduced computing power, e.g., handheld devices. We also investigate the behavior of our approach with specific respect to preserving the ST segment [8, 13]. Eventually, we present an over-

all analysis of performances of our approach and state-of-the-art algorithms that assesses algorithms *jointly* in terms of effectiveness in removing baseline drift, distortion introduced in the ST segment and computational burden [13]. To our knowledge, this kind of joint analysis has never been conducted before. Results show that quadratic variation reduction has the best performance and is the fastest algorithm for baseline wander removal, among those effective in removing baseline wander.

The chapter is organized as follows. In Section 7.2 we give some details about the ST segment and its clinical relevance. Due to the importance of baseline wander removal in ECG, Section 7.3 is fully devoted to review the literature on this topic. The rationale behind the approach we propose is described in Subsection 7.4.1. The baseline wander estimator is derived in Section 7.4.2 as the solution to a constrained convex optimization problem. In Section 7.5 we report an efficient implementation of the algorithm. Numerical results of several performance analyses are reported in Section 7.6. We assess performances of our approach with regard to different aspects, i.e., effectiveness in removing baseline drift, distortion in the ST segment and computational burden, and compare it to the state of the art. Finally, Section 7.7 follows with conclusions.

7.2 The ST segment

The ST segment represents the period at which the entire ventricle is depolarized and roughly corresponds to the plateau phase of the ventricular action potential [15]. In health conditions, it is isoelectric with respect to the PQ segment. The ST segment has strong clinical relevance, since deviations from its physiological level, namely elevation or depression, as shown in Figure 7.2.1, indicate that membrane potentials in ventricular cells are nonuniform [15]. This condition reflects an undergoing Acute Coronary Syndrome (ACS).

ACS are life-threatening disorders and represent one of the most severe forms of heart disease and the main cause of mortality in developed countries [124]. According to the Heart Disease and Stroke Statistics 2012 Update from the American Heart Association (AHA), 1,190,000 hospital discharges in the United States were due to ACS in 2009 [32]. Moreover, approximately every 25 seconds, an American will have a coronary event, and approximately every minute, someone

Chapter 7

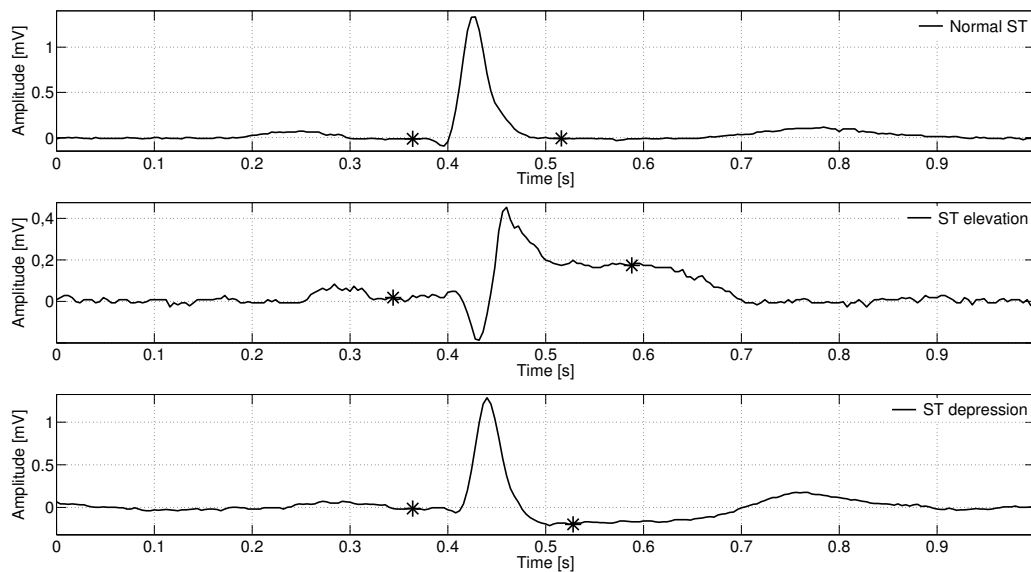


Figure 7.2.1: ECG beats from real data exhibiting a normal ST segment level (i.e., isoelectric to PQ segment, top), ST elevation ($+165\mu\text{V}$ relative to isoelectric PQ level, middle) and ST depression ($-167\mu\text{V}$ relative to isoelectric PQ level, bottom). Asterisks mark isoelectric PQ level and ST level.

will die of one [32]. As reported in [125–127], the term ACS comprises a continuum of biological events progressing from plaque instability to plaque rupture, coronary thrombosis, reduced coronary blood flow, myocardial ischemia and, ultimately, myocardial necrosis. ACS identifies a spectrum of clinical disorders caused by acute ischemic heart disease, including unstable angina, ST-segment elevation myocardial infarction and non-ST-segment elevation myocardial infarction [124, 125].

The ECG is the gold standard for identifying the presence and location of acute myocardial ischemia [128]. Hence, it is a fundamental tool for the diagnosis of ACS [99, 129]. Information about the site of the infarct related lesion, prediction of final infarct size, and estimation of prognosis can be obtained from the initial ECG [128]. The main electrocardiographic abnormalities in ACS are ST segment deviations (elevation or depression), T-wave tenting or inversion and pathologic Q-waves [14, 124, 125, 129–131]. Thus, special care must be paid in any processing of ECG signals to preserve the features related to these syndromes,

in particular the ST-segment. However, despite the clinical relevance of this portion of the ECG, only few approaches to baseline wander removal explicitly focus on minimizing distortion of the ST segment, as will be shown in the next section.

7.3 Review of baseline wander removal for ECG

The simplest approach to ECG baseline wander removal is high-pass filtering with cut-off frequency of about 0.8Hz [132, 133], and it is available with efficient implementations [78, 134]. However, this approach, and in general any technique for baseline removal that relies on frequency domain separation, may induce unacceptable distortions in the ST segment [18, 25, 29, 135–137]. To prevent this, the American Heart Association (AHA) recommends a cut-off frequency of 0.05 Hz for routine filters or 0.67 Hz or below for linear digital filters with zero phase distortion [99]. However, some residual baseline drift may still be present in the filtered signal [25]. To overcome this problem, linear time-variant filtering approaches have been proposed. In [138] is proposed a low-pass filter with time-varying cut-off frequency that depends on the instantaneous RR interval, i.e., the interval between two consecutive R peaks. This approach has better performance than low-pass filtering with fixed cut-off frequency, but can still distort the ST segment. Adaptive filtering was proposed in [74], where baseline is estimated minimizing the mean-squared error between the noisy ECG and a constant reference input. However, due to slow convergence, this approach cannot track abrupt changes in baseline and causes distortion in the ST segment as well [74]. To cope with this problem, in [139] a cascade adaptive filter is proposed, where the adaptive filter of [74] is combined with an adaptive impulse correlated filter.

A different approach is median filtering proposed in [140, 141]. It consists in subtracting from the signal the median value computed in a sliding window of fixed length. Performance dramatically depends on the choice of the window length. To deal with this problem, in [141] a two-stage median filtering using two different window lengths is proposed. However, a residual drift in the detrended signal is still noticeable [141]. In [142] a multistage procedure, including median subtraction and polynomial fitting, is proposed. Computational complexity increases, and the procedure requires an accurate detection of QRS complexes [142].

Another common technique for baseline estimation is polynomial fitting, typically cubic splines [143, 144]. This approach requires the identification of an isoelectric point, namely knot, for every beat. Baseline is estimated as the polynomial that best fits the knots. The major disadvantage of this technique is that it needs ECG delineation, which may lead to unreliable knots location in presence of noise [22]. Moreover, performance dramatically decreases in presence of low heart rates. Indeed, low heart rates mean knots located far apart, and thus only slow trends can be caught in baseline estimate [22, 144]. Moreover, polynomial fitting is unviable in presence of arrhythmias or premature complexes and cannot remove sudden baseline shifts [145].

Multiresolution analysis based on wavelet decomposition is another common technique for baseline removal. It has been proposed in several works [84, 146–150]. Basically, wavelet decomposition approaches decompose the signal into a preset number of components having different scales and resolutions [85]. Components affected by baseline drift are either discarded [147, 150] or filtered [146, 148, 149]. The signal is then reconstructed by an inverse transformation. The different approaches mainly differ in the choice of the mother wavelet, the number of components in which the original signal is decomposed, and the way components affected by baseline are selected and processed. The Daubechies wavelet db4 [151] is among the most used, since the corresponding mother wavelet has a shape resembling the typical ECG beat [149, 150]. In [148] the component contributing to baseline undergoes a so-called wavelet averaging filtering, i.e., the average amplitude of the PQ segment is subtracted in each beat. In [149] baseline is estimated as the component whose energy, calculated as a function of wavelet coefficients, exceeds an empirical threshold. In [146] a joint approach, namely WAF, combining wavelet decomposition and adaptive filter is proposed. Baseline drift is removed by adaptively filtering the wavelet component that mainly contributes to baseline. In evaluating performance, the problem of ST segment distortion is explicitly taken into account. Finally, the bionic wavelet transform is used in [84], which results in a better tradeoff between time and frequency resolution [152]. The major issues when using wavelet decomposition are the choice of the mother wavelet, the number of decomposition levels, and the use of automatic or empirical threshold, if soft-thresholding is used.

Mathematical morphology [86–88, 153, 154] is another approach to baseline

wander removal, which is also known as background normalization in this context. This is a nonlinear technique for signal or image processing based on set operations [88] that incorporates shape information of a signal or image [86]. The basic idea of mathematical morphology is to modify geometric features, i.e., the shape information of a signal, considered as a set, by transforming it through its interaction with another object, referred to as the structuring element [88]. The basic morphological operators are erosion and dilatation that combined result in opening and closing operators [88]. There are several papers that exploit mathematical morphology for baseline wander removal in ECG [86–88, 153, 154]. They mainly differ in the choice of the structuring element, the order in which operators are applied, and the way operators are combined. Moreover, in [154] morphological operators and empirical mode decomposition are used in combination. The main drawbacks of background normalization by morphological operators are the presence of residual drift and noticeable distortions in the detrended signal [86–88].

A relatively recent approach to baseline removal is empirical mode decomposition (EMD) [94], and its modified version, namely ensemble EMD [155]. It relies on the local characteristic time scale of the data, and thus can be applied to nonlinear and non-stationary processes [94]. The EMD is a data-driven technique that decomposes (within a prescribed error) the signal into a sum of intrinsic mode functions (IMFs) with decreasing frequency content. Higher-order IMFs represent slow oscillations and are expected to mainly contribute to baseline. Thus, baseline drift is removed discarding or filtering the last higher-order IMFs. The main concerns about this technique are the trial by trial choice of the number of IMFs to reject or filter, and the high computational burden. Moreover, simply discarding the last higher-order IMFs, as in [156–158], may introduce significant distortions [93], since relevant signal components may be cancelled. For this reason, EMD is usually followed by additional low-pass filtering steps [93, 154], which add complexity to an already time-consuming procedure.

For the sake of completeness, we mention few other approaches addressing the problem of baseline wander removal for ECG. Joint baseline wander and power-line interference removal is performed in [159] by means of a nonlinear trimmed moving average filter. An adaptive Kalman filter is proposed in [160]. In [161] is presented an algorithm based on the notion of dominant points. Independent component analysis is exploited in [162] and neural networks in [163].

Among all the approaches cited above, those that somehow take into account the problem of preserving the ST segment are only two, to the the best of our knowledge. First, a high-pass two-pole, phase-compensated digital filter was proposed in [134] and its ability to remove baseline wander without altering the ST segment was discussed. However, the proposed filter fails the AHA triangular test for ST segment distortion [135] and results in a cutoff frequency of 1 Hz, in contrast to AHA recommendations [99]. Second, the problem of ST segment distortion is explicitly taken into account in evaluating performance of WAF [146]. Moreover, a comparative analysis of seven different baseline removal algorithms was carried out in [164], strictly focusing on the evaluation of distortions introduced into the ST segment. The algorithm that proved being the most effective in this regard is right the WAF [146]. Finally, for the sake of completeness, we mention that in [165] ST segment distortion is used, with other figures of merit, to characterize performance of some baseline removal algorithms.

Finally, in the recent works [9, 10, 12] we have proposed a novel approach to baseline wander estimation and removal, based on the notion of *quadratic variation reduction*. It is the object of this chapter and will be described and analyzed in full detail in the following sections.

7.4 The proposed approach

7.4.1 Rationale

As highlighted in Section 7.1, ECG baseline wander is modeled as a low-frequency additive noise over the range $0 \div 1$ Hz [16, 22]. Thus, baseline wander and ECG overlap in the low-frequency region of the spectrum. The low-frequency components of the ECG (mainly) contribute to the shape of the ST segment [136]: distortion in this band of the ECG spectrum negatively affects the shape of the ST segment, thus spoiling relevant clinical information. As a consequence, the in-band nature of baseline wander makes its removal difficult without affecting the ECG, in particular the ST segment [135, 136]. In other words and with little abuse of language, baseline wander is a “low-frequency” noise and the “low-frequency” components of the ECG (mainly) contribute to the shape of the ST segment. The problem is that they overlap both in time and frequency domain. As a conse-

quence any technique for baseline removal that relies on spectral shaping, e.g., linear time-invariant filters, will unavoidably alter the ST segment. To cope with this problem it is necessary to take a different perspective on baseline noise and ECG components contributing to the ST segment. That is, they should be separated in a domain that is not the frequency domain. To this end, the following considerations come in useful.

Baseline wander is a “low-variability” noise and the ST segment is a “low-variability” component¹ of the ECG as well. When they are considered in the frequency domain, “low-variability” is synonymous of “low-frequency”, bandwidth is regarded as a measure of “variability”, and the aforementioned problem of overlapping bands arises. To cope with this problem it is necessary to introduce a suitable measure of “variability” that is not directly related to the frequency domain. A careful choice of such a measure allows us to separate baseline noise from ECG components contributing to the ST segment. Thus baseline wander can be removed from ECG without significantly affecting the ST segment.

To this end the quadratic variation (3.3.1) comes in useful. It is a good candidate in this regard since it is not directly related to the frequency domain and with Proposition 1 in Subsection 3.3.2 we have proved that it is a consistent measure of variability. Being baseline drift a “low-variability” noise, it exhibits low quadratic variation. Hence, baseline wander can be estimated searching for ECG components with reduced quadratic variation [9, 10].

7.4.2 Baseline Wander Estimation and Removal

In this section, we denote by $\tilde{\mathbf{z}}$ the vector collecting n samples of a measured biosignal, i.e., one that is affected by baseline wander, by \mathbf{x} the vector of estimated baseline, and by $\mathbf{z} = \tilde{\mathbf{z}} - \mathbf{x}$ the corresponding detrended vector. Following the line of reasoning presented above, baseline wander can be estimated searching for a signal component that has reduced variability, with respect to the measured signal. This amounts to searching for a component that is “close” to the observed signal, but has *reduced* quadratic variation. The problem of baseline estimation can be recast as a convex optimization problem

¹To be precise, “low-variability” components of the ECG contribute to the ST segment.

$$\begin{cases} \underset{\mathbf{x} \in \mathbb{R}^n}{\text{minimize}} & \|\mathbf{x} - \tilde{\mathbf{z}}\|^2 \\ \text{subject to} & [\mathbf{x}] \leq \rho \end{cases} \quad (7.4.1)$$

where ρ is a nonnegative constant that controls the quadratic variation of the estimated baseline [9, 10]. Its value is chosen in accordance with the peculiarity of the problem and satisfies $\rho < [\tilde{\mathbf{z}}]$, to avoid trivial solutions. We do not need to know in advance the appropriate value for ρ in any particular problem since, as shown in Chapter 3, the solution to the optimization problem (7.4.1) can be expressed in terms of a parameter that controls the quadratic variation of the solution and that is related to ρ in (7.4.1).

Problem (7.4.1) resembles problem (3.3.5) for smoothing single ECG waves in Chapter 3. However, here we use it to estimate the slow unwanted oscillations due to baseline drift that are then removed from the measured signal. Recalling Subsection 3.3.3, the solution to (3.3.5) is

$$\mathbf{x} = (\mathbf{I} + \lambda \mathbf{D}^T \mathbf{D})^{-1} \tilde{\mathbf{z}} \quad (7.4.2)$$

where \mathbf{I} denotes the $n \times n$ identity matrix, and λ is a nonnegative parameter determined by (3.3.9). Note that in (7.4.2) the matrix inverse exists for any $\lambda \geq 0$, since $\mathbf{D}^T \mathbf{D}$ is positive semidefinite. It is interesting that solution to (7.4.1) is a linear operator acting on $\tilde{\mathbf{z}}$. Moreover, the Lagrange multiplier λ plays the role of a parameter controlling the quadratic variation of the solution \mathbf{x} , i.e., the degree of variability of the estimated baseline. Moreover, λ can be used in place of ρ since they are in one-to-one correspondence through (3.3.9). In fact, with Proposition 2 in Subsection (3.3.3) we proved that $[\mathbf{x}]$ is a continuous and strictly decreasing function of $\lambda \in [0, +\infty)$ regardless of $\tilde{\mathbf{z}}$, provided that it is not a constant vector. When $\tilde{\mathbf{z}}$ is a constant vector $[\mathbf{x}] = 0$. Moreover,

$$\lim_{\lambda \rightarrow +\infty} [\mathbf{x}] = 0$$

regardless of $\tilde{\mathbf{z}}$.

This is equivalent to say that, when $\tilde{\mathbf{z}}$ is not a constant vector, a one-to-one correspondence is established between $\lambda \in [0, +\infty)$ and $\rho \in (0, [\tilde{\mathbf{z}}]]$, with $\lambda = 0$

corresponding to $\rho = \tilde{\mathbf{z}}$, and $\lambda \rightarrow +\infty$ corresponding to $\rho \rightarrow 0^+$.

As a consequence, we *do not need to know* in advance the value of ρ in (7.4.1), since baseline can be estimated according to (7.4.2) and λ can be adapted to the particular problem or to meet some performance criteria. That is, λ is used in place of ρ as the controlling parameter.

In particular, since baseline is characterized by low values of the quadratic variation with respect to the measured signal, it is estimated with (7.4.2) using *large* values of λ . In our simulations values of the order of 10^3 or even more are quite common. Based on this fact, it is worthwhile considering the behavior of the solution (7.4.2) in the limit for $\lambda \rightarrow +\infty$.

Proposition 3. *The following limit holds*

$$\lim_{\lambda \rightarrow +\infty} (\mathbf{I} + \lambda \mathbf{D}^T \mathbf{D})^{-1} \tilde{\mathbf{z}} = \left(\frac{1}{n} \sum_{k=1}^n \tilde{z}_k \right) \mathbf{1} \quad (7.4.3)$$

where $\mathbf{1} = [1 \cdots 1]^T \in \mathbb{R}^n$ and \tilde{z}_k is the k th component of $\tilde{\mathbf{z}}$ [10].

Proof. Matrix $\mathbf{D}^T \mathbf{D}$ is symmetric positive semidefinite and thus diagonalizable [64]. Moreover, it is tridiagonal and has zero as a simple eigenvalue with corresponding unit-norm eigenvector $\frac{1}{\sqrt{n}} \mathbf{1}$ [67]. Thus, the spectral decomposition of $\mathbf{D}^T \mathbf{D}$ can be expressed as

$$\mathbf{D}^T \mathbf{D} = \mathbf{U} \mathbf{\Gamma} \mathbf{U}^T \quad (7.4.4)$$

where $\mathbf{\Gamma} = \text{diag}(0, \gamma_2, \dots, \gamma_n)$ is a diagonal matrix with $\gamma_i > 0$, for $i = 2, \dots, n$, and \mathbf{U} is an orthogonal matrix having $\frac{1}{\sqrt{n}} \mathbf{1}$ as its first column.

Exploiting (7.4.4) and the fact that $\gamma_i \neq 0$, for $i = 2, \dots, n$, the limit in (7.4.3) becomes

$$\begin{aligned} \lim_{\lambda \rightarrow +\infty} (\mathbf{I} + \lambda \mathbf{D}^T \mathbf{D})^{-1} &= \lim_{\lambda \rightarrow +\infty} \mathbf{U} (\mathbf{I} + \lambda \mathbf{\Gamma})^{-1} \mathbf{U}^T \\ &= \mathbf{U} \left[\lim_{\lambda \rightarrow +\infty} \text{diag} \left(1, \frac{1}{1 + \lambda \gamma_2}, \dots, \frac{1}{1 + \lambda \gamma_n} \right) \right] \mathbf{U}^T \\ &= \mathbf{U} \text{diag}(1, 0, \dots, 0) \mathbf{U}^T = \frac{1}{n} \mathbf{1} \mathbf{1}^T \end{aligned}$$

which proves the proposition.

□

The asymptotic solution in (7.4.3) corresponds to the mean value of $\tilde{\mathbf{z}}$, which is the constant vector closest in the l_2 norm to the measured record. Consistently with Proposition 2, such vector has zero quadratic variation.

As λ ranges from 0 to $+\infty$, solution (7.4.2) captures components of the measured signal $\tilde{\mathbf{z}}$ with decreasing quadratic variation. When $\lambda \rightarrow +\infty$ such components reduce to the constant vector in (7.4.3), whereas when λ is finite more complex trends of the measured signal are captured.

Once the baseline has been estimated, it can be removed from the measured signal by subtraction

$$\begin{aligned} \mathbf{z} = \tilde{\mathbf{z}} - \mathbf{x} &= \left[\mathbf{I} - (\mathbf{I} + \lambda \mathbf{D}^T \mathbf{D})^{-1} \right] \tilde{\mathbf{z}} \\ &= \mathbf{D}^T \left(\frac{1}{\lambda} \mathbf{I} + \mathbf{D} \mathbf{D}^T \right)^{-1} \mathbf{D} \tilde{\mathbf{z}}, \end{aligned}$$

where in the last equality the Sherman-Morrison-Woodbury formula [64] has been applied.

Baseline wander estimation through (7.4.2) is a linear operator acting on the signal to detrend $\tilde{\mathbf{z}}$. As noted in Subsection (3.3.3), the matrix of the transformation, namely $(\mathbf{I} + \lambda \mathbf{D}^T \mathbf{D})^{-1}$, is not Toeplitz [66] and this makes the transformation time variant [68]. As a consequence, there exists *no* linear time-invariant filter that can achieve the same result as (7.4.2) [10]. However, it can be proved that, under some hypotheses, smoothing through (3.3.8) is approximately equivalent to passing the signal through a two-poles IIR filter whose transfer function is the z-transform of an autocorrelation function. Thus its frequency response has zero phase. In particular, it is the autocorrelation function of the impulse response of a single-pole IIR filter. In other words, smoothing through (3.3.8) can be approximately seen as zero-phase filtering, where data are passed through a single-pole IIR filter in both the forward and reverse directions [2].

7.4.2.1 Sensitivity analysis

As noticed above, baseline wander is estimated with (7.4.2) using large values of λ . However, no criterion is given to determine its appropriate value. This in

general depends on the performance metrics adopted and the class of signals to detrend. Nevertheless, it is useful to analyze how robust the proposed algorithm is to variations of λ . A measure of robustness is the sensitivity of baseline estimate to the variations of λ . Measuring sensitivity in terms of the derivative of $[\mathbf{x}]$ with respect to λ , the following result holds [10].

Proposition 4. *The sensitivity of $[\mathbf{x}]$ with respect to variations of λ satisfies*

$$\frac{\partial [\mathbf{x}]}{\partial \lambda} = O\left(\frac{1}{\lambda^3}\right) \text{ as } \lambda \rightarrow +\infty$$

where $O(\cdot)$ denotes the Landau symbol.

Proof. Let us consider the quadratic variation of the solution $[\mathbf{x}]$ as expressed by (3.3.13). Differentiating (3.3.13) with respect to λ we get

$$\frac{d[\mathbf{x}]}{d\lambda} = -\sum_{i=2}^n \frac{2(\gamma_i \mathbf{u}_i^T \tilde{\mathbf{z}})^2}{(1 + \lambda \gamma_i)^3}$$

from which the proof follows, considering the behavior as $\lambda \rightarrow +\infty$. □

Proposition 4 states that for large values of λ , and this is the case of baseline estimation, as λ increases the quadratic variation of the estimate is less and less dependent on the value of λ . Said in different words, the choice of λ is *not* a critical issue: a wide range of different values of λ produces similar estimates. This is indeed well confirmed by the numerical results reported in Section 7.6, in particular Subsection 7.6.1.4.

7.5 Fast Algorithm for Baseline Estimation

Baseline wander estimation using formula (7.4.2) involves matrix inversion. So, computational aspects become important, especially when the size of the vector to detrend is large, e.g., for typical ECG records. Indeed, in this case, the computational burden, both in terms of time and memory, and the accuracy become serious issues, even for batch processing. However, estimating the baseline through

(7.4.2) amounts to solve a linear system where the coefficient matrix, namely $(\mathbf{I} + \lambda \mathbf{D}^T \mathbf{D})$, is tridiagonal [64]. Tridiagonal systems can be solved efficiently with $O(n)$ operations [69], being n the number of unknowns. As a consequence, baseline wander estimation using (7.4.2) can be performed with complexity $O(n)$, i.e., *linear* in the size n of the vector to detrend.

Below we report the pseudocode of an efficient implementation of (7.4.2), which is the baseline wander estimation by quadratic variation reduction (QVR) [12].

Algorithm 1 QVR Baseline wander estimation

```

1: function QVRB( $\lambda, \mathbf{x}$ )
2:    $n \leftarrow \text{length}(\mathbf{x})$ 
3:    $y_1 \leftarrow -\lambda / (1 + \lambda)$ 
4:    $x_1 \leftarrow x_1 / (1 + \lambda)$ 
5:   for  $i \leftarrow 2$  to  $n - 1$  do
6:      $t \leftarrow 1 + \lambda \cdot (2 + y_{i-1})$ 
7:      $y_i \leftarrow -\lambda / t$ 
8:      $x_i \leftarrow (x_i + \lambda \cdot x_{i-1}) / t$ 
9:   end
10:   $y_n \leftarrow (x_n + \lambda \cdot x_{n-1}) / (1 + \lambda + \lambda \cdot y_{n-1})$ 
11:  for  $i \leftarrow n - 1$  downto 1 do
12:     $y_i \leftarrow x_i - y_i \cdot y_{i+1}$ 
13:  end
14:  return  $\mathbf{y}$ 
15: end

```

The input vector \mathbf{x} is the signal to detrend. The output vector \mathbf{y} in line 14 is the estimated baseline. The components of vectors are denoted by subscripts. Note that vector \mathbf{x} is internally modified in lines 4 and 8. To avoid this, such lines should be substituted with $z_1 \leftarrow x_1 / (1 + \lambda)$ and $z_i \leftarrow (x_i + \lambda \cdot z_{i-1}) / t$, respectively, and lines 10 and 12 with $y_n \leftarrow (x_n + \lambda \cdot z_{n-1}) / (1 + \lambda + \lambda \cdot y_{n-1})$ and $y_i \leftarrow z_i - y_i \cdot y_{i+1}$, respectively.

Linear complexity is a very important property that makes the proposed algorithm suitable for real-time applications, as well as for applications on devices with reduced computing power, e.g., handheld devices. To give an idea of how fast the algorithm is, a MATLAB (ver. 7.11) implementation of the algorithm above

running over a PC equipped with 2.3 GHz Core i5 processor, takes about 0.73 s to estimate the baseline from an ECG record of 10^7 double precision floating point samples. Considering handheld devices, a non optimized Java program running over an Android smartphone equipped with 1.2 GHz dual-core ARM Cortex-A9 processor takes about 0.2 s to estimate the baseline from an ECG record of 10^6 double precision floating point samples.

In the Subsection 7.6.3, we will show that, to the best of our knowledge, the proposed algorithm is the fastest algorithm for baseline wander estimation and removal, among those effective in removing baseline wander.

7.6 Numerical results

Performances of the proposed approach have been investigated with regard to two different aspects: effectiveness in removing baseline wander and distortion introduced in the ST segment. In either case, a comparative analysis with state-of-the-art algorithms for baseline wander removal has been conducted. Further, an overall analysis of performance has been carried out, taking into account *jointly* effectiveness in removing baseline wander, distortion introduced in the ST segment and computational burden. To our knowledge, this kind of joint analysis has never been conducted before. As numerical results reported hereafter will show, quadratic variation reduction has the best performance and is the fastest algorithm for baseline wander removal, among those effective in removing baseline drift.

This section is organized as follows. In Subsection 7.6.1 we report results of our performance analysis with regard to effectiveness in removing baseline wander. In particular, real and synthetic ECG signals are considered. Moreover, an analysis of robustness of our approach with regard to the parameter λ is carried out. Distortion introduced in the ST segment by our approach and state-of-the-art algorithms is reported in Subsection 7.6.2. Results of the overall analysis of performances are presented in Subsection 7.6.3.

For the sake of brevity, throughout the section the acronym QVR is used in place of quadratic variation reduction.

7.6.1 Effectiveness in removing baseline wander

We assess how effective our approach and state-of-the-art algorithms are in removing baseline wander both on real and synthetic ECG signals for a quantitative evaluation. Different performance metrics are considered in the two cases.

7.6.1.1 Performance metrics

For real ECG signals, the quality of baseline wander removal is evaluated by a visual qualitative comparison of the corresponding detrended signals, since the wandering affecting the true ECG is not known.

In the case of synthetic ECG signals, baseline wander free ECG signals are corrupted by known baseline wanders, which can be compared with the corresponding estimated baselines. The quality of baseline wander removal is evaluated through the following quantity

$$\varepsilon(\mathbf{x}_i, \mathbf{b}_i) = \frac{\|\mathbf{x}_i - \mathbf{b}_i\|^2}{\|\mathbf{b}_i\|^2} \quad (7.6.1)$$

where \mathbf{b}_i denotes the generic baseline wander realization and \mathbf{x}_i the corresponding baseline estimate. Performance of different algorithms is measured in terms of the empirical distribution function of the corresponding errors (7.6.1), namely

$$\hat{F}(\varepsilon) = \frac{1}{N} \sum_{i=1}^N \chi_{(-\infty, \varepsilon]}(\varepsilon(\mathbf{x}_i, \mathbf{b}_i)) \quad (7.6.2)$$

where $\chi_E(\cdot)$ denotes the indicator function of the set E , and N is the number of generated baseline realizations. Note that the empirical distribution function (7.6.2) provides a *complete* statistical description of the performance of each algorithm, as opposed to the mean, the variance, or the median, which give only partial information: different algorithms may exhibit errors with the same mean, median, and variance, even though the corresponding empirical distribution functions are completely different.

The use of empirical distribution function as a performance metric is motivated by the following reasons. Firstly, the Glivenko-Cantelli Theorem [166] guarantees that almost surely as $N \rightarrow \infty$, the empirical distribution function in (7.6.2)

converges uniformly to the true cumulative distribution function, since the maximum gap between the two of them goes to zero. Moreover, the estimation error in approximating the true cumulative distribution function is controlled by the Dvoretzky–Kiefer–Wolfowitz inequality [167]. Note that no similar result holds for the histogram, which moreover suffers from some problems that make it not the best choice for density estimation [167]. Secondly, the data under analysis, namely the errors in (7.6.1), are not Gaussian distributed and thus they cannot be characterized statistically by (sample) mean and variance only. Strictly speaking, errors in (7.6.1) are not Gaussian distributed since they are nonnegative and upper bounded. However, they could be approximately Gaussian distributed and this would justify their characterization in terms of (sample) mean and variance. To answer this question, we tested the data under analysis for normality using Shapiro-Wilk, Shapiro-Francia, and Anderson-Darling tests [168]. These tests are considered to be among the most powerful, if not the most powerful, tests for detecting departure from normality [168, 169]. Moreover, in their application we took into account that the Shapiro-Wilk test is more powerful at detecting platykurtic² and skewed distributions, and the Shapiro-Francia test is more powerful against leptokurtic² and symmetric distributions [170]. The results of our analysis show that for about half of the records the hypothesis of normality can be rejected at the 0.05 significance level (minimum p-value $< 2 \times 10^{-5}$) [12]. As a consequence, errors in (7.6.1) cannot be fully characterized statistically using only the first two moments, namely sample mean and variance, and the empirical distribution function (7.6.2) is needed for a complete statistical description.

An important aspect of empirical distribution functions is that they allow us to compare algorithms over the *full range* of errors taking account of error relative frequencies. This cannot be achieved by considering sample mean and variance only. Moreover, empirical distribution functions are useful for characterizing algorithms that have uniformly better performance over the whole range of errors, where better is meant as statistically better.

To this end, denoting by $\hat{F}_A(\varepsilon)$ and $\hat{F}_B(\varepsilon)$ the empirical distribution functions of errors, relative to algorithms *A* and *B* respectively, we introduce the following

²Platykurtic distributions and leptokurtic distributions are characterized by negative and positive excess kurtosis, respectively.

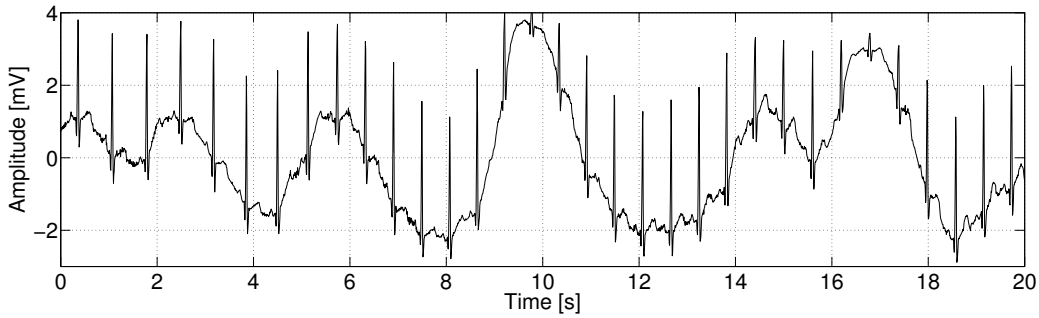


Figure 7.6.1: ECG from real data: segment of record nsrdb/16773 from PhysioNet [19, 173].

Definition 2. *Algorithm A is statistically uniformly better than algorithm B if*

$$\hat{F}_A(\varepsilon) > \hat{F}_B(\varepsilon), \quad \forall \varepsilon \in \mathcal{E}_{AB} \quad (7.6.3)$$

with $\mathcal{E}_{AB} = \{\varepsilon \in \mathbb{R} \mid 0 < \hat{F}_A(\varepsilon) + \hat{F}_B(\varepsilon) < 2\}$.

Set \mathcal{E}_{AB} consists of all real numbers except those for which $\hat{F}_A(\varepsilon) = \hat{F}_B(\varepsilon) \in \{0, 1\}$ that are not relevant for comparison. Note that when (7.6.3) holds true, $\hat{F}_A(\varepsilon) \geq \hat{F}_B(\varepsilon) \forall \varepsilon \in \mathbb{R}$, with the inequality becoming strict for $\varepsilon \in \mathcal{E}_{AB}$. In other words, algorithm A is statistically uniformly better than algorithm B when $\hat{F}_B(\varepsilon)$ is upper bounded by $\hat{F}_A(\varepsilon)$ for all values of ε except those for which $\hat{F}_A(\varepsilon)$ and $\hat{F}_B(\varepsilon)$ are both equal to 0 or 1 [12].

The relation of being statistically uniformly better is a strict partial order [171], since it is irreflexive and transitive, and thus can be used to compare algorithms. In particular, if algorithm A is statistically uniformly better than algorithm B, then it exhibits lower errors with higher probability. As a consequence, all the moments of error for algorithm A are lower than the corresponding moments for algorithm B. Moreover the median error for algorithm A, which is a more robust index of centrality [172], is also lower. Being statistically uniformly better is a strong property.

As we will see in Subsection 7.6.1.3, baseline wander removal by QVR is uniformly better than competing algorithms.

Chapter 7

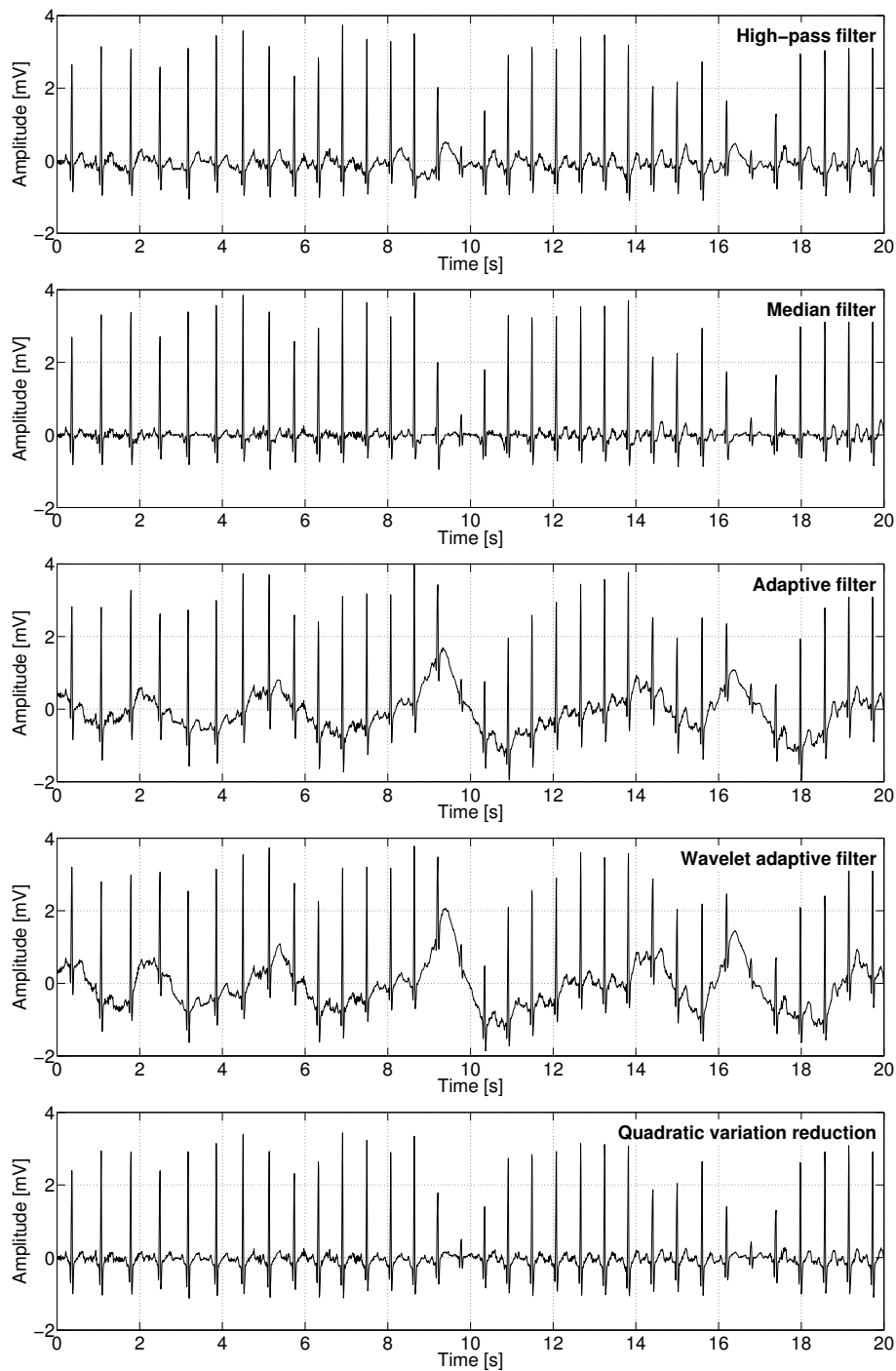


Figure 7.6.2: ECG of Figure 7.6.1 after baseline wander removal using different approaches [12].

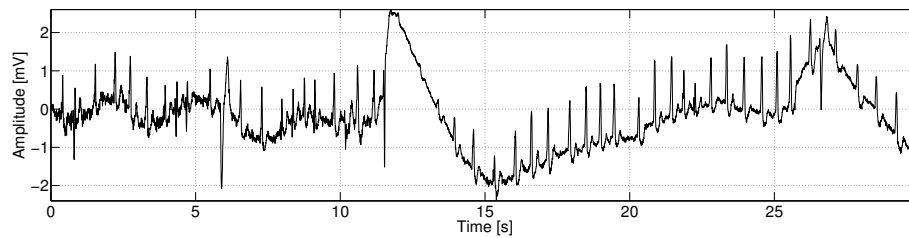


Figure 7.6.3: ECG from real data: segment of record mitdb/203 from PhysioNet.

7.6.1.2 Performance on real ECG signals

We considered ECG traces from the MIT-BIH Normal Sinus Rhythm Database publicly available on PhysioNet [19, 173]. This database includes 18 long-term ECG recordings of subjects with no significant arrhythmias. Signals were acquired at a sampling frequency of 128Hz with 12-bit resolution. We compared the performance of QVR with high-pass filtering [16, 22, 99], median filtering [140], adaptive filtering [74], and wavelet adaptive filtering [146], which are common approaches to baseline wander removal, as highlighted in Section 7.1. The high-pass filter is a linear-phase FIR filter synthesized applying the window method [68] using a Kaiser window, with 0.1 dB ripple in passband and 80dB attenuation in stopband, with cut-off frequency 0.67 Hz compliant with AHA recommendations [99]. The window size of the median filter is chosen adapting the criterion proposed in [140] to the sampling frequency of 128Hz. The convergence parameter of the adaptive filter and the wavelet adaptive filter is settled to obey AHA requirements on cut-off frequency.

We tested the performance of the aforementioned algorithms on several records from MIT-BIH Normal Sinus Rhythm Database, without fine tuning of the parameter λ in the QVR. In all cases, results are very similar and are well summarized by the example in Figure 7.6.1, where a 20s segment of the record nsrdb/16773 is reported. This record is characterized by strong baseline wandering. Figure 7.6.2 shows the same record after baseline wander removal using the algorithms described above. A visual qualitative comparison of the figures highlights the better performance of QVR, which managed to remove baseline wander while preserving the shape of the ECG [12].

As a further example, we report the results of detrending by our and competing

Chapter 7

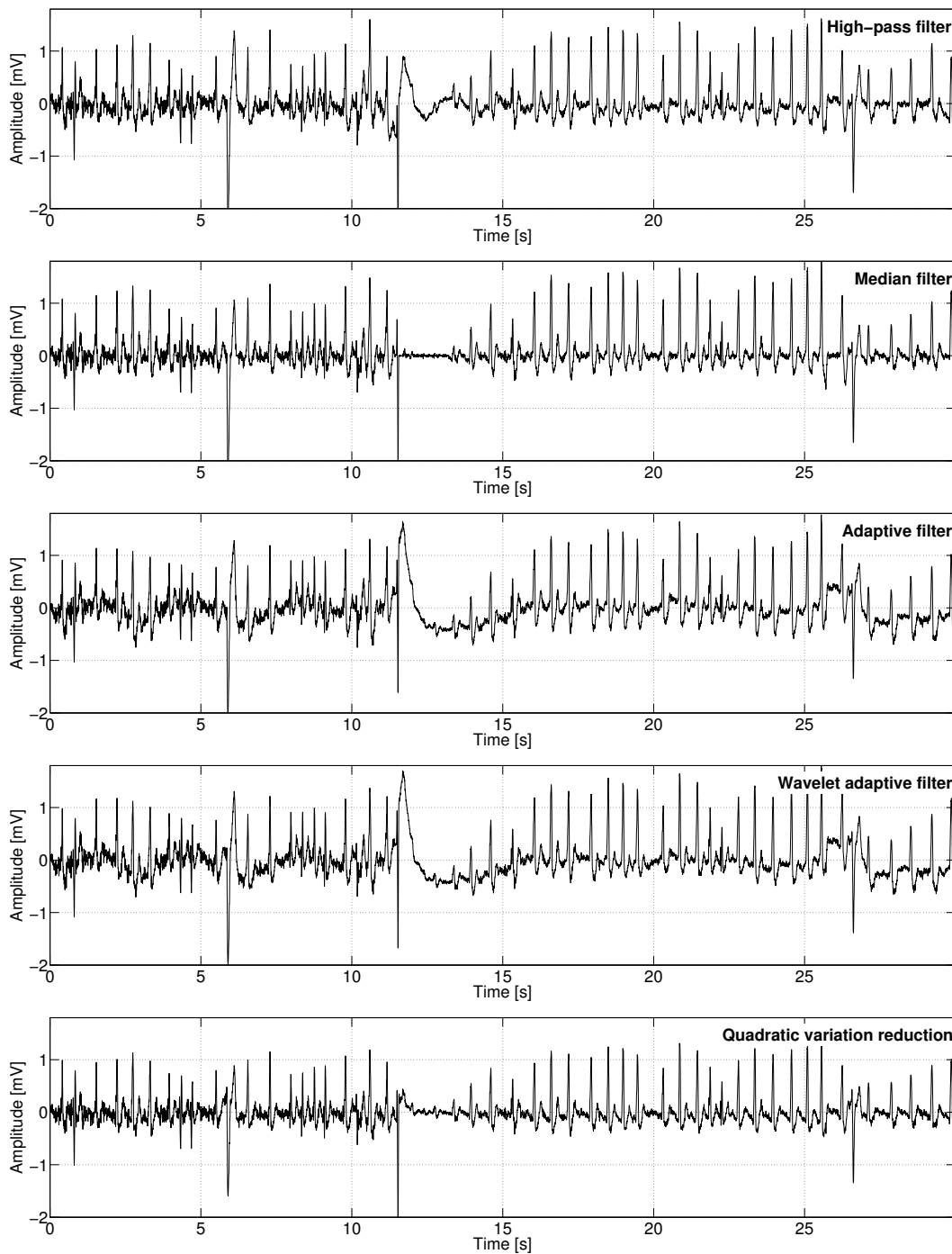


Figure 7.6.4: ECG of Figure 7.6.3 after baseline wander removal using different approaches [10].

approaches considering a different ECG record. Figure 7.6.3 shows a 30s segment of the record mitdb/203 from the MIT- BIH Arrhythmia Database, publicly available on PhysioNet [19, 97]. The database includes ECG records acquired at a sampling frequency of 360Hz with 11-bit resolution. In particular, the record in Figure 7.6.3 is known to be strongly affected by baseline drift and very difficult to analyze even for humans [174]. Figure 7.6.4 shows the same record after baseline wander removal using (from top to bottom) high-pass filtering [16, 22, 99], median filtering [140], adaptive filtering [74], wavelet adaptive filtering [146], and the proposed approach. Again, a visual comparison of the panels in Figure 7.6.4 highlights the better performance of QVR [12].

Note that both in Figure 7.6.2 and Figure 7.6.4 median filtering manages to remove baseline wander, but introduces evident distortions in the signal, especially where baseline has rapid changes, e.g., around time 9s in Figure 7.6.2 and around time 11s in Figure 7.6.4. Moreover, zooming the scale, distortion in the portion following QRS complexes, namely the ST segment and the beginning of T-wave, becomes clearly visible.

7.6.1.3 Performance on synthetic ECG signals

In order to quantify the performance of the proposed approach, we carried out a quantitative analysis on synthetic ECG signals affected by simulated baseline wander. Baseline wander free ECG signals were synthesized using the model in [79] with a sampling frequency of 512Hz. To take into account different physiological conditions, we generated three 40s long ECG records with heart rate 75 bpm, 40 bpm, and 140 bpm, which model normal sinus rhythm, sinus bradycardia, and sinus tachycardia, respectively. The resulting records are denoted in the following by $\mathbf{z}_0^{(n)}$, $\mathbf{z}_0^{(b)}$, $\mathbf{z}_0^{(t)}$, respectively. Synthetic baseline wander was rendered as Gaussian white noise with variance $\sigma^2 = 6.25$ low-pass filtered with bandwidth 0.8Hz, following similar approaches in the literature [93, 143, 153, 159]. To model measurement noise, the ECG records $\mathbf{z}_0^{(n)}$, $\mathbf{z}_0^{(b)}$, $\mathbf{z}_0^{(t)}$ were corrupted by additive Gaussian noise with signal-to-noise ratio (SNR) 20 dB.

We generated 300 independent realizations of synthetic baseline and measurement noise, denoted by \mathbf{b}_i and \mathbf{n}_i , respectively, with $i = 1, \dots, 300$. Baseline wander and noise are independent. For each pair of realizations \mathbf{b}_i and \mathbf{n}_i we consid-

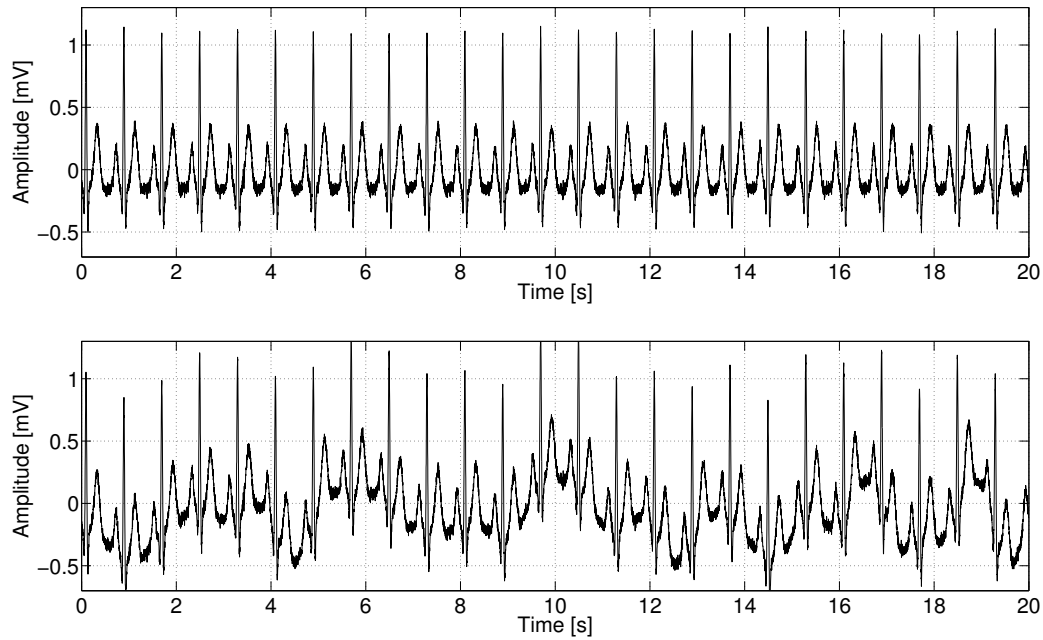


Figure 7.6.5: Noisy synthetic ECG (SNR = 20dB) in normal sinus rhythm (top) corrupted by baseline wander (bottom) [12].

ered the following ECG records

$$\begin{aligned}
 \tilde{\mathbf{z}}_i^{(n)} &= \mathbf{z}_0^{(n)} + \mathbf{n}_i + \mathbf{b}_i \\
 \tilde{\mathbf{z}}_i^{(b)} &= \mathbf{z}_0^{(b)} + \mathbf{n}_i + \mathbf{b}_i \\
 \tilde{\mathbf{z}}_i^{(t)} &= \mathbf{z}_0^{(t)} + \mathbf{n}_i + \mathbf{b}_i
 \end{aligned} \tag{7.6.4}$$

corresponding to normal sinus rhythm, sinus bradycardia, and sinus tachycardia, respectively. Note that we have deliberately used the same pair of noise and baseline realizations for the three reference ECG records to allow a fair comparison. As an example, in Figure 7.6.5 we report a 20s segment of noisy ECG in normal sinus rhythm, namely $\mathbf{z}_0^{(n)} + \mathbf{n}_i$, and the same record corrupted by baseline wander, namely $\tilde{\mathbf{z}}_i^{(n)}$.

We compared the performance of our algorithm with the following approaches to baseline wander removal: i) high-pass filtering [16, 22, 99], ii) cubic spline interpolation [143], iii) median filtering [140], iv) the method in [142], v) adaptive

filtering [74], and vi) wavelet adaptive filtering [146].

High-pass, median, adaptive, and wavelet adaptive filters were implemented as described in the previous subsection. Cubic spline interpolation [143] and the method in [142] rely on the accurate location of R peaks. Since ECG records were generated synthetically, the exact location of R peaks was known a priori, and this information was fed to both the algorithms. Thus, their performance must be considered optimistic. The parameter λ for QVR was chosen as the one that entails the minimum of (7.6.1) for each baseline realization. This choice is motivated by the need to determine the limit performance of the proposed algorithm. However, it will be shown in the following subsection that the value of λ is *not* critical, since a wide range of different values produces similar good estimates.

For all baseline realizations \mathbf{b}_i (and corresponding noise realizations \mathbf{n}_i) we computed the empirical distribution function of the error (7.6.1) for every algorithm, for each of the three ECG records in (7.6.4).

Figure 7.6.6 reports the empirical distribution functions of errors (7.6.1) for the baseline wander removal algorithms under analysis, under the three physiological conditions of normal sinus rhythm (top), sinus bradycardia (middle), and sinus tachycardia (bottom). As Figure 7.6.6 highlights, baseline wander removal by QVR exhibits the best performance, as it is statistically *uniformly better* than competing algorithms in all three heart rhythm conditions [12].

For the sake of correctness, it should be noted that being statistically uniformly better does not exclude the eventuality that for some baseline and noise realizations another algorithm could exhibit lower errors. Nevertheless, in our simulations baseline wander removal by QVR returned the lowest error for any realization of baseline, in any heart rate condition. Moreover, from Figure 7.6.6 in the normal sinus rhythm (top panel), it emerges an even stronger condition: the maximum error returned by QVR, namely 0.130, is below the minimum error (0.145) of the second best algorithm, which is median filtering [12].

Since QVR is statistically uniformly better than competing algorithms, it exhibits better performance over the full range of errors thus having the lowest mean and median error. Moreover, it also exhibits the lowest variance of error, as follows from Table 7.1 where we report the mean μ_e , median $\tilde{\epsilon}$ and variance σ_e^2 of error (7.6.1) for the algorithms considered. Values in Table 7.1 are computed from the same data used to generate the empirical distribution functions of Figure 7.6.6.

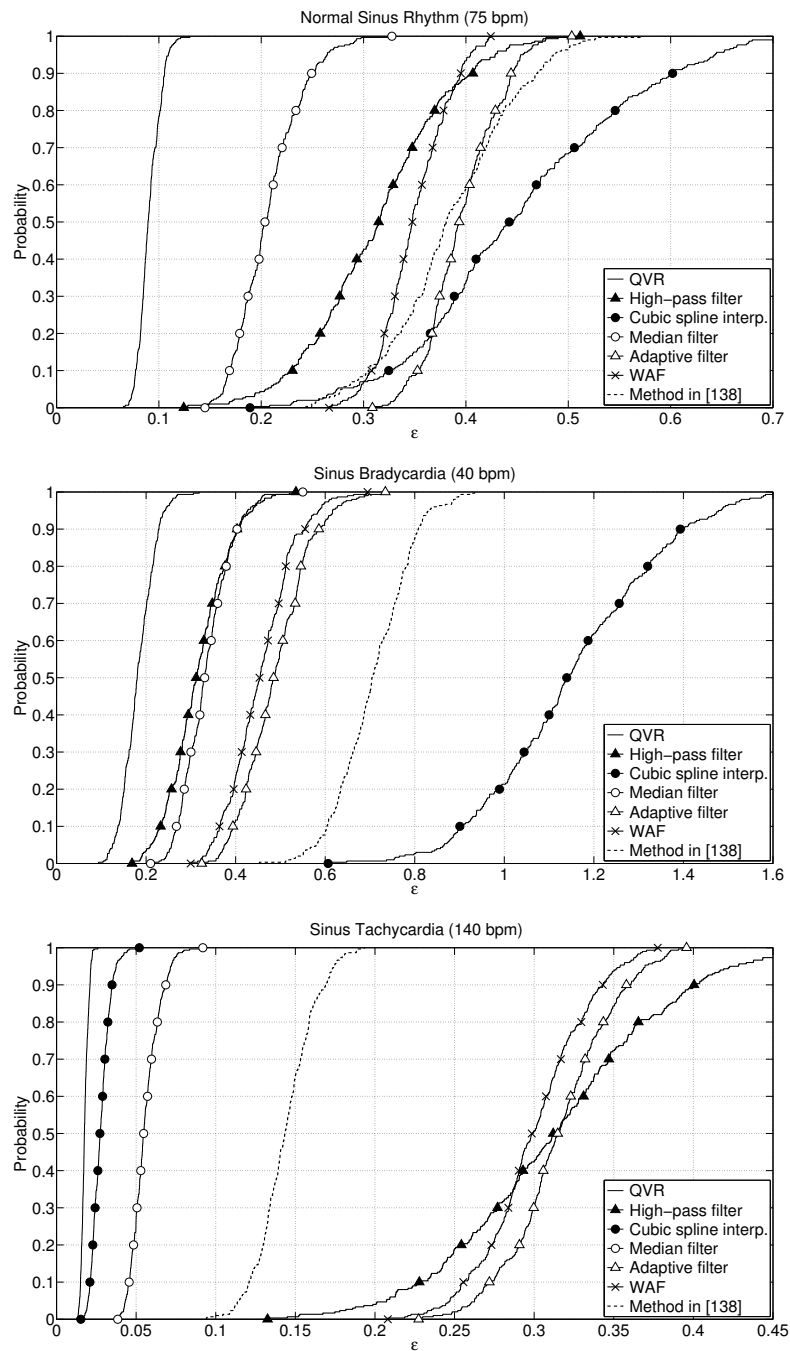


Figure 7.6.6: Empirical distribution functions of the error (7.6.1) for different algorithms, under normal sinus rhythm, sinus bradycardia and sinus tachycardia [12].

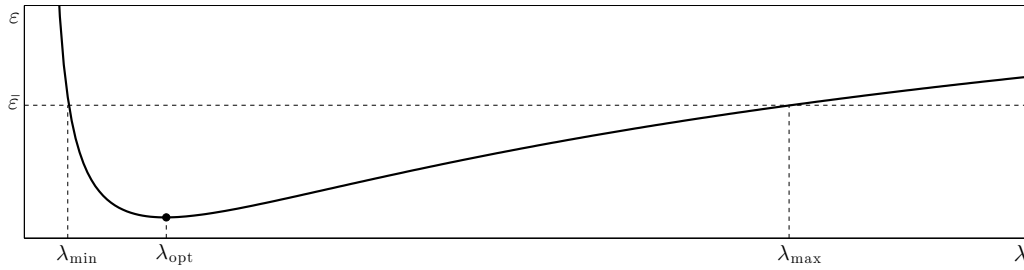


Figure 7.6.7: Typical behavior of the error (7.6.1) for QVR as a function of λ .

Note that we considered the median error since it is a more robust index of centrality [172], however in this case it has values comparable with the mean error for all algorithms. The superiority of QVR over competing algorithms is evident.

Finally, it is worthwhile noting that as the heart rate changes, the second best algorithm correspondingly changes. This implies that, without QVR, one should choose the algorithm according to the heart rate, which is impractical. In this regard QVR guarantees the best performance regardless of the heart rate.

7.6.1.4 Robustness to variations of λ

As highlighted in the previous subsection, baseline wander removal by QVR is statistically uniformly better than competing algorithms. Moreover, we remarked that in our simulations QVR always exhibited the minimum error (7.6.1) among all the algorithms considered, for any realization of baseline. Here we analyze how sensitive the solution given by QVR is to variations of the parameter λ . In particular we want to ascertain how large the interval of values of λ is for which QVR is still the best algorithm. The larger this interval is the more robust QVR is to variations of λ . We will show shortly after that such interval is *very large*, and this makes the choice of λ *not* a critical issue.

For a generic baseline realization, the error (7.6.1) returned by QVR as a function of the parameter λ exhibits the typical behavior depicted in Figure 7.6.7, where $\bar{\epsilon}$ denotes the error of the second best algorithm. Thus, for each baseline realization, indexed by i , we can compute the interval $[\lambda_{\min}(i), \lambda_{\max}(i)]$ of values of λ such that QVR still yields the minimum error (7.6.1) among all algorithms, and the value $\lambda_{\text{opt}}(i) \in [\lambda_{\min}(i), \lambda_{\max}(i)]$ for which QVR returns the minimum er-

Method	<i>Normal Sinus Rhythm (75 bpm)</i>		
	μ_{ϵ}	$\tilde{\epsilon}$	σ_{ϵ}^2
High-pass filter	0.31	0.31	4.6×10^{-3}
Cubic spline interpolation	0.45	0.44	1.1×10^{-2}
Median filter	0.21	0.20	1.0×10^{-3}
Method in [142]	0.39	0.38	3.8×10^{-3}
Adaptive filter	0.40	0.39	1.3×10^{-3}
Wavelet Adaptive Filter (WAF)	0.35	0.35	1.1×10^{-3}
Quadratic Variation Reduction (QVR)	0.09	0.09	1.0×10^{-4}

Method	<i>Sinus Bradycardia (40 bpm)</i>		
	μ_{ϵ}	$\tilde{\epsilon}$	σ_{ϵ}^2
High-pass filter	0.32	0.31	4.5×10^{-3}
Cubic spline interpolation	1.15	1.14	3.6×10^{-2}
Median filter	0.33	0.33	2.9×10^{-3}
Method in [142]	0.71	0.70	6.7×10^{-3}
Adaptive filter	0.49	0.48	5.5×10^{-3}
Wavelet Adaptive Filter (WAF)	0.46	0.45	5.2×10^{-3}
Quadratic Variation Reduction (QVR)	0.18	0.18	1.3×10^{-3}

Method	<i>Sinus Tachycardia (140 bpm)</i>		
	μ_{ϵ}	$\tilde{\epsilon}$	σ_{ϵ}^2
High-pass filter	0.31	0.31	4.6×10^{-3}
Cubic spline interpolation	0.03	0.03	3.2×10^{-5}
Median filter	0.06	0.05	1.0×10^{-3}
Method in [142]	0.14	0.14	3.0×10^{-3}
Adaptive filter	0.32	0.32	1.1×10^{-3}
Wavelet Adaptive Filter (WAF)	0.30	0.30	1.0×10^{-3}
Quadratic Variation Reduction (QVR)	0.02	0.02	4.9×10^{-6}

Table 7.1: Mean (μ_{ϵ}), median ($\tilde{\epsilon}$) and variance (σ_{ϵ}^2) of error (7.6.1) for different approaches tested in three heart rate conditions.

	$\bar{\lambda}_{\min}$	$\bar{\lambda}_{\text{opt}}$	$\bar{\lambda}_{\max}$	$\frac{\bar{\lambda}_{\text{opt}}}{\bar{\lambda}_{\min}}$	$\frac{\bar{\lambda}_{\max}}{\bar{\lambda}_{\text{opt}}}$
Normal Sinus Rhythm	1572	5981	24012	3.8	4.0
Sinus Bradycardia	2506	9203	33136	3.6	3.7
Sinus Tachycardia	1105	2082	3991	1.9	1.9

Table 7.2: Average values of $\lambda_{\min}(i)$, $\lambda_{\text{opt}}(i)$, $\lambda_{\max}(i)$ and their ratios [12].

ror (7.6.1) (see Figure 7.6.7).

Figure 7.6.8 reports in logarithmic scale the values $\lambda_{\min}(i)$, $\lambda_{\text{opt}}(i)$, and $\lambda_{\max}(i)$ obtained for the 300 baseline realizations and the three heart rate conditions considered in the previous subsection: $\lambda_{\text{opt}}(i)$ is in solid line, whereas $\lambda_{\min}(i)$ and $\lambda_{\max}(i)$ are denoted by downward-pointing and upward-pointing triangles, respectively. Moreover, horizontal dashed lines are superimposed to identify the respective arithmetic means, denoted by $\bar{\lambda}_{\min}$, $\bar{\lambda}_{\text{opt}}$, and $\bar{\lambda}_{\max}$. As Figure 7.6.8 highlights, the interval of values of λ for which QVR returns the best performance is quite large for any realization of baseline [10, 12]. This is particularly evident when considering the average values $\bar{\lambda}_{\min}$ and $\bar{\lambda}_{\max}$, which are approximately equidistant (in logarithmic scale) from $\bar{\lambda}_{\text{opt}}$, in the three heart rate conditions.

The values of $\bar{\lambda}_{\min}$, $\bar{\lambda}_{\text{opt}}$, $\bar{\lambda}_{\max}$ are reported in Table 7.2 together with the corresponding ratios $\bar{\lambda}_{\text{opt}}/\bar{\lambda}_{\min}$ and $\bar{\lambda}_{\max}/\bar{\lambda}_{\text{opt}}$. Some remarks are in order. The first remark is that the interval $[\bar{\lambda}_{\min}, \bar{\lambda}_{\max}]$ is *very large*, regardless of the heart rate. This confirms the sensitivity analysis of Proposition 4 in Subsection 7.4.2.1 [10]. Note that in the case of sinus tachycardia the second best algorithm taken as a reference is cubic spline interpolation. Its performance is optimistic, as remarked in the previous subsection, so the interval $[\bar{\lambda}_{\min}, \bar{\lambda}_{\max}]$ in this case is actually larger. The second remark is that interestingly the two ratios $\bar{\lambda}_{\text{opt}}/\bar{\lambda}_{\min}$ and $\bar{\lambda}_{\max}/\bar{\lambda}_{\text{opt}}$ are approximately equal³. Even though only average values are involved, this property suggests that choosing $\lambda = \alpha\bar{\lambda}_{\text{opt}}$ or $\lambda = \bar{\lambda}_{\text{opt}}/\alpha$, with $\alpha > 0$ “small” in some way, one should expect similar results. This is indeed the case, as we will show below.

³In the case of sinus tachycardia the ratios are actually larger as explained above in the case of $\bar{\lambda}_{\min}$ and $\bar{\lambda}_{\max}$.

Chapter 7

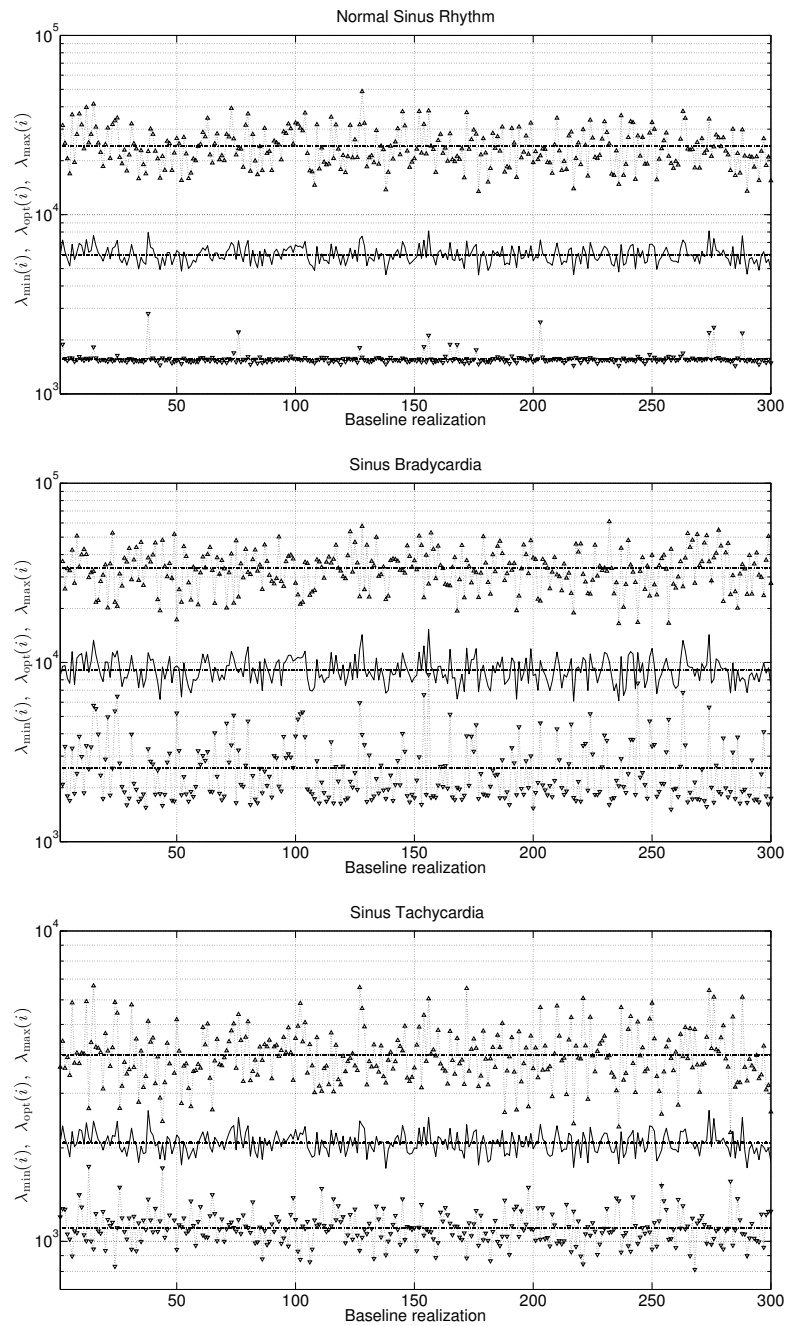


Figure 7.6.8: $\lambda_{\min}(i)$ (point-down triangle), $\lambda_{\text{opt}}(i)$ (continuous line), and $\lambda_{\max}(i)$ (point-up triangle) as a function of the i th baseline realization, for normal sinus rhythm, sinus bradycardia and sinus tachycardia [12].

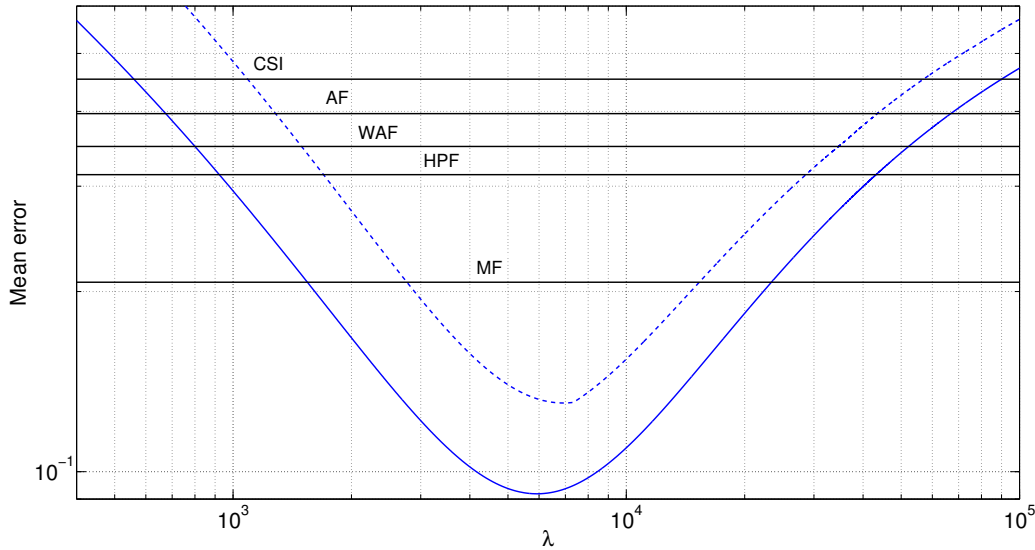


Figure 7.6.9: Mean (solid blue) and maximum (dash blue) error (7.6.1) for different values of λ compared to the mean error of state-of-the-art algorithms from Table 7.1, in the case of normal sinus rhythm [10].

In Figure 7.6.9, we report the baseline estimation error (7.6.1) returned by the proposed approach in normal sinus rhythm, as a function of λ . In particular, Figure 7.6.9 reports, in log-log scale, the mean error (7.6.1) (solid blue line), averaged over the 300 realizations of baseline and noise, considered in the case of normal sinus rhythm. The dash line corresponds to the maximum error (7.6.1) over all realizations. In the same figure we report for comparison the mean error of state-of-the-art algorithms (horizontal black lines) from Table 7.1: cubic spline interpolation (CSI), adaptive filtering (AF), wavelet adaptive filtering (WAF), high-pass filtering (HPF), median filtering (MF). Figure 7.6.9 confirms that the interval of values of λ for which quadratic variation reduction outperforms competing algorithms is quite large, namely $[1.6 \times 10^3, 2.4 \times 10^4]$, and exceeds one decade. It is worthwhile noting that such interval is still quite large even in the case of maximum error [10].

In Figure 7.6.10 we report the results of a similar analysis for the variance of error (7.6.1) of quadratic variation reduction for different values of λ (solid blue line), compared to the variance of error of state-of-the-art approaches (horizontal

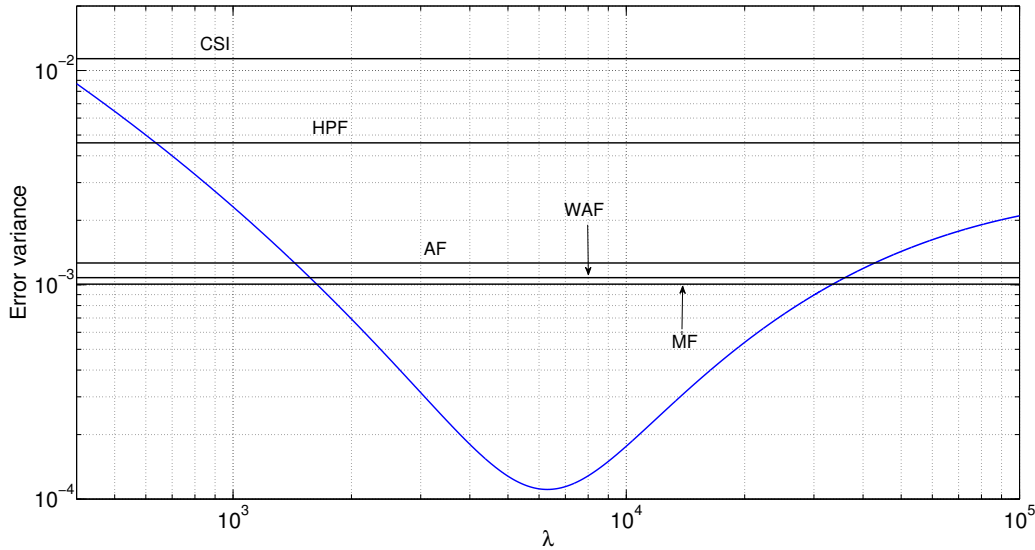


Figure 7.6.10: Variance of error (7.6.1) for different values of λ (blue) compared to the variance of error of state-of-the-art algorithms (black), in the case of normal sinus rhythm [10].

black lines) from Table 7.1, considering the case of normal sinus rhythm [10]. Plots are in log-log scale. Even in this case, the interval of values of λ for which quadratic variation reduction outperforms competing algorithms is quite large, namely $[1.6 \times 10^3, 3.4 \times 10^4]$.

The results of Figure 7.6.9 and Figure 7.6.10 can be combined in order to compare algorithms in terms of *both* mean and variance of error. To this end, in Figure 7.6.11 we report the parametric plot (solid blue line) of the mean $\mu_\varepsilon(\lambda)$ and the variance $\sigma_\varepsilon^2(\lambda)$ of error (7.6.1) for the proposed approach, parametrized by λ , compared to the corresponding values of competing algorithms (black circles) from Table 7.1, which are independent of λ . Again, values in the figure refer to the condition of normal sinus rhythm. Arrows indicate the direction in which λ increases. The best algorithm is the one closest to the origin of the axes. As Figure 7.6.11 highlights, the range of values of λ for which the proposed approach outperforms competing algorithms is quite large. In particular, for $\lambda \in [1.6 \times 10^3, 2.4 \times 10^4]$, which is more than one decade, baseline wander removal by quadratic variation reduction has uniformly the lowest mean error and the low-

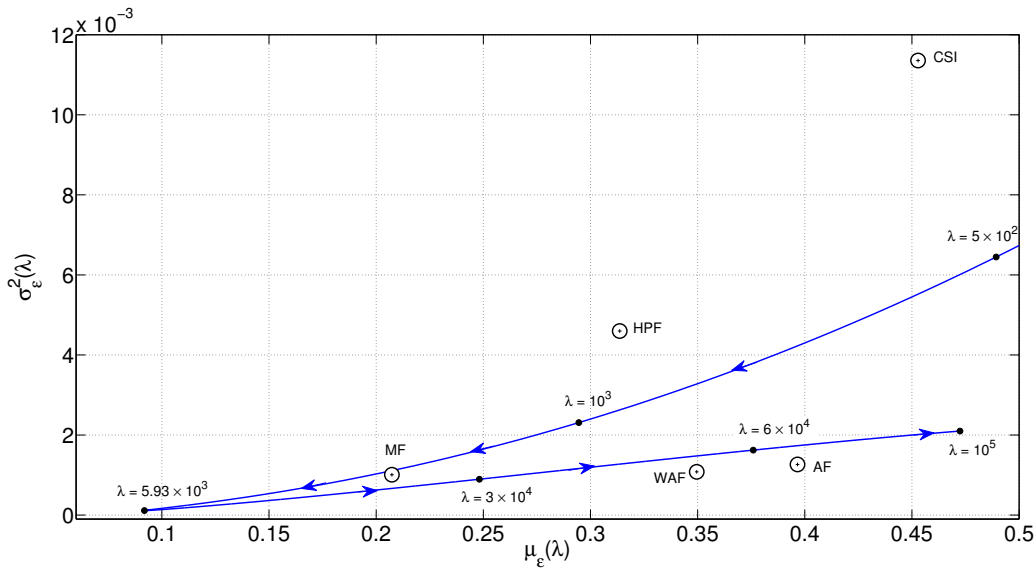


Figure 7.6.11: Parametric plot (blue) of mean $\mu_{\epsilon}(\lambda)$ and variance $\sigma_{\epsilon}^2(\lambda)$ of error (7.6.1) for different values of λ , compared to competing algorithms (black circles), in the case of normal sinus rhythm [10].

est error variance among all algorithms [10]. This confirms the robustness of the proposed approach and corroborate the sensitivity analysis of Subsection 7.4.2.1, thus making the choice of λ *not* a critical issue.

The curves corresponding to QVR in Figure 7.6.6 were computed setting λ to the optimal value $\lambda_{\text{opt}}(i)$, for any realization of baseline. Thus, it is important to evaluate the loss in performance when non optimal values of λ are used. In this regard, choosing the same constant value for all realizations of baseline is an unfavorable condition, nevertheless it is a method to assess the robustness of QVR. Following this approach, we tested QVR with different values of λ , keeping it constant for all baseline realizations. Figure 7.6.12 reports the results of the analysis in the case of normal sinus rhythm (top panel), sinus bradycardia (middle panel), and sinus tachycardia (bottom panel), respectively. Let us analyze them separately.

The top panel of Figure 7.6.12 (normal sinus) reports as reference the empirical distribution functions of QVR (solid line) and median filter (solid line with circles) from Figure 7.6.6. These are the best and the second best algorithms in

the case of normal sinus rhythm. The remaining curves (dashed, dotted, and dash-dotted) correspond to the empirical distribution functions of QVR computed using λ constant for all baseline realizations. The value of λ is reported near the corresponding curve. There are four groups of curves that are close together. Starting from the leftmost, the first group compares the reference empirical distribution function of QVR (solid line) and the corresponding function computed using $\lambda = \bar{\lambda}_{\text{opt}}$ (dash-dotted line) for all baseline realizations. In this case $\bar{\lambda}_{\text{opt}} = 5981$ from Table 7.2. The two curves are almost *indistinguishable*, thus proving that even with constant λ it is possible to achieve performance nearly *identical* to the limit performance. This result is important and confirms the robustness of QVR to variations of λ [12]. The second group comprises the empirical distribution functions of QVR computed using $\lambda = \bar{\lambda}_{\text{opt}}/2$ (dotted line) and $\lambda = 2\bar{\lambda}_{\text{opt}}$ (dashed line), whereas the third one depicts the same functions computed using $\lambda = \bar{\lambda}_{\text{opt}}/3$ (dotted line) and $\lambda = 3\bar{\lambda}_{\text{opt}}$ (dashed line). Finally, the fourth group consists of the empirical distribution functions of QVR computed using $\lambda = \bar{\lambda}_{\text{opt}}/3.8$ (dotted line) and $\lambda = 4\bar{\lambda}_{\text{opt}}$ (dashed line), and the same function of median filter (solid line with circles) from Figure 7.6.6. In this case, the values for λ have been computed using the data from the last two columns of Table 7.2. It is interesting to note that the two curves corresponding to $\lambda = \bar{\lambda}_{\text{opt}}/3.8$ (dotted line) and $\lambda = 4\bar{\lambda}_{\text{opt}}$ (dashed line), not only are close together, but they are close to the empirical distribution function of the median filter, namely the second best algorithm.

The middle panel of Figure 7.6.12 (sinus bradycardia) shows as reference the empirical distribution functions of both QVR (solid line) and high-pass filter (solid line with triangles) from Figure 7.6.6, which are the best and the second best algorithms in the case of sinus bradycardia. The remaining curves (dashed, dotted, and dash-dotted) are as in the top panel. The leftmost group of curves compares the reference empirical distribution function of QVR (solid line) and the corresponding function computed using $\lambda = \bar{\lambda}_{\text{opt}}$ (dash-dotted line) for all baseline realizations. In this case $\bar{\lambda}_{\text{opt}} = 9203$. The second group comprises the empirical distribution functions of QVR computed using $\lambda = \bar{\lambda}_{\text{opt}}/2$ (dotted line) and $\lambda = 2\bar{\lambda}_{\text{opt}}$ (dashed line), whereas the third one depicts the same functions computed using $\lambda = \bar{\lambda}_{\text{opt}}/3.6$ (dotted line) and $\lambda = 3.7\bar{\lambda}_{\text{opt}}$ (dashed line).

The bottom panel of Figure 7.6.12 (sinus tachycardia) reports as reference the empirical distribution functions of QVR (solid line), cubic spline (solid line

with filled circles) and median filter (solid line with circles) from Figure 7.6.6. These are the best, the second and the third best algorithms in the case of sinus tachycardia. The performance of median filter has been explicitly reported since the performance of cubic spline should be considered optimistic for the reason given in the previous subsection. The remaining curves (dashed, dotted, and dash-dotted) correspond to empirical distribution functions of QVR with λ constant for all baseline realizations, where the value of λ is reported near the corresponding curve.

From the above analysis, two interesting properties emerge. The first is that setting λ constant for all baseline realizations it is possible to achieve performance nearly identical to the limit performance; the second is that choosing two values of λ , namely λ_1 and λ_2 , such that $\bar{\lambda}_{\text{opt}}/\lambda_1 = \lambda_2/\bar{\lambda}_{\text{opt}}$, QVR achieves very similar performance. Both these properties confirm the robustness of QVR with respect to variations of λ [12].

These results confirm that the performance of the proposed approach is remarkable even though the parameter λ is not accurately determined. Indeed, depending on heart rate, the value of λ can be decreased or increased up to about 4-fold with respect to $\bar{\lambda}_{\text{opt}}$, and QVR continues to be the best algorithm. This eventually confirms that the choice of the value for the parameter λ is not a critical issue [10, 12].

7.6.2 Distortion in the ST segment

We considered ECG recordings from the European ST-T Database [175], collected by the European Society of Cardiology and publicly available on PhysioNet [19]. The database collects 90 ambulatory ECG recordings, each two hours long. Each record includes two signals, sampled at 250Hz with 12-bit resolution. Recordings are from subjects with diagnosis or suspicion of myocardial ischemia. Each record contains at least one ST or T episode: these are intervals during which ST segments or T waves undergo significant changes. The reader is invited to consult [175] for details. In the following, we will consider only ST episodes, being ST segment distortion a critical issue for baseline wander removal, as highlighted in Subsection 7.4.1. Two cardiologists, working independently, inspected and annotated ST segment displacements in each signal in the database. Manual

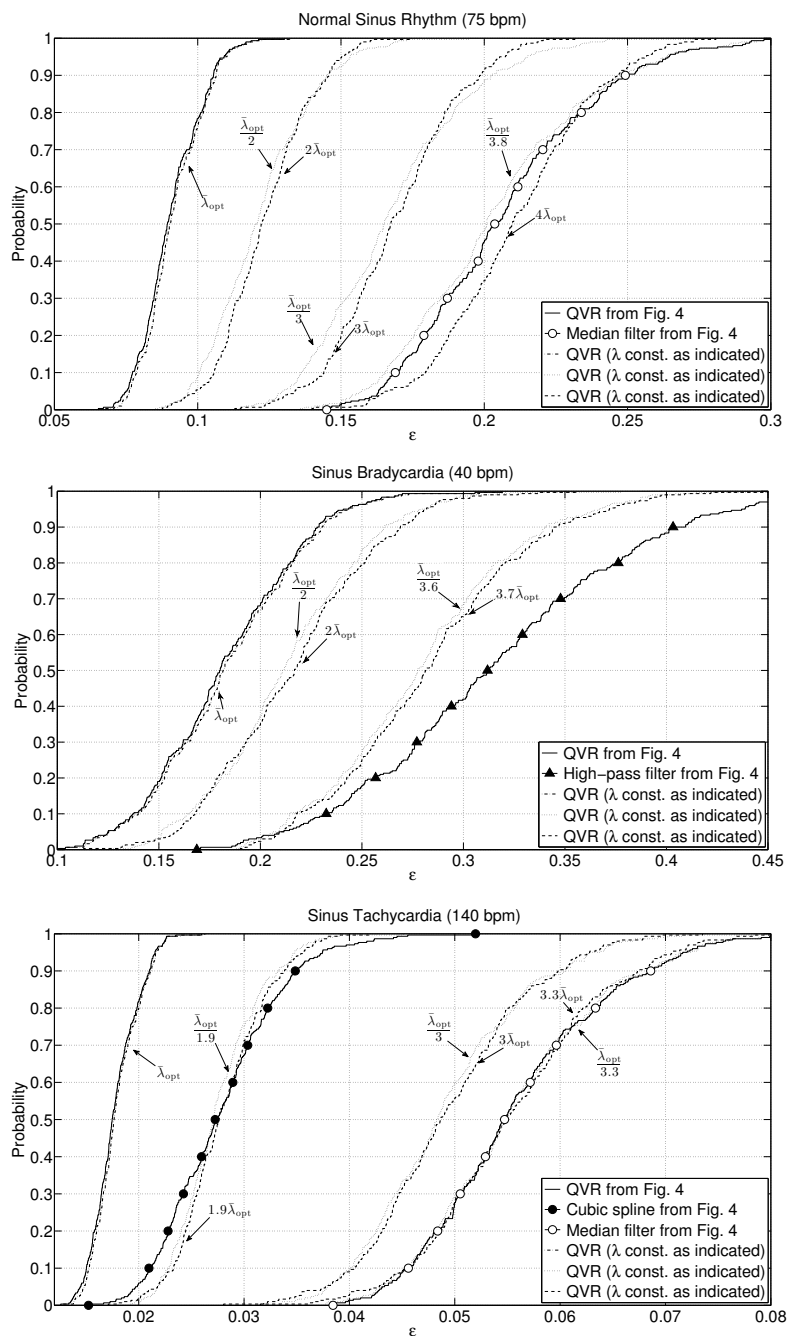


Figure 7.6.12: Empirical distribution functions of QVR for different constant values of λ , and curves from Figure 7.6.6 as reference, for normal sinus rhythm, sinus bradycardia and sinus tachycardia [12].

annotations consist in information about the onset, the offset and the peak, i.e., the greatest deviation, of each episode. Onsets and offsets are annotated in terms of temporal lag. Regarding the peak, an annotation was placed before the beat judged to exhibit the greatest deviation; this annotation contains a manual measurement, namely δ^{man} , of the peak ST variation. Such quantity was computed as

$$\delta^{\text{man}} = \delta_{\circ} - \phi. \quad (7.6.5)$$

where δ_{\circ} is the difference between the ST segment level and the isoelectric level and ϕ represents an offset that accounts for any fixed ST elevation or depression, due to possible prior myocardial infarctions. Originally, it was computed on a reference waveform, which was extracted from the first 30s of the record being annotated. Put in other words, the ST annotations in the database mark transient ST changes that are superimposed on any fixed elevation or depression [175, 176].

To evaluate how our approach and competing algorithms affect the ST segment, it is necessary to compare ST segment deviations computed on ECGs affected by baseline wander with the same deviations computed on detrended signals. This may be accomplished by comparing the peak ST deviation in detrended signals with the corresponding manual annotation δ^{man} . To this end, the following quantities need to be computed: location and amplitude of ST segment, and location and amplitude of isoelectric segment. Moreover, to exploit information about peak amplitude of ST episodes, the offset ϕ must be known.

To locate the temporal lag where the ST segment is measured, the location of the J point, i.e., the offset of QRS complex, is required. To this end, we implemented the procedure described in [16, 177], considering as fiducial points the annotations of normal beats in the database. Measurements of ST segment are taken at a distance from the J point dependent on the heart rate, according to [175]. The ST segment amplitude is computed as means of signal segments of 20ms surrounding the ST segment lag, in order to avoid jitter due to amplitude scatter of the original signal samples [16].

According to the literature [16, 177], the isoelectric level is measured at the PQ segment. To locate the PQ segment and to estimate the isoelectric level, we considered the procedure in [16, 177], considering as fiducial points the annotations of normal beats in the database.

As regards the offset, unfortunately, the reference waveform for each record is no longer available [176]. The only available information is that the waveform was taken from the first 30s of the record [176]. Thus, the quantity ϕ is unknown for each record and needs to be estimated in order to use manual annotations. As proposed in [176], we estimated it as the mean⁴ difference, namely $\tilde{\phi}$, between the amplitudes of ST segment and isoelectric PQ segment all over the first 30s of each record. Particularly noisy beats were discarded via visual inspection. To check for the consistency of such estimate, we estimated the difference, namely $\tilde{\delta}_o$, between the ST segment level and isoelectric PQ level on annotated beats of the record under analysis. We then compared $\tilde{\phi}$ to the quantity $\tilde{\delta}_o - \delta^{\text{man}}$. Unfortunately, the estimates $\tilde{\phi}$ for all records did not pass such consistency test: considerable and not uniform discrepancies between $\tilde{\phi}$ and $\tilde{\delta}_o - \delta^{\text{man}}$, up to the same order of magnitude as δ^{man} , were found. Moreover, nor the use of the quantity $\tilde{\delta}_o - \delta^{\text{man}}$, averaged for each record, proved to be a consistent estimate of the offset ϕ . Indeed, it is plain that the offset must be the same for different ST episodes in the same record. In spite of that, the quantity $\tilde{\delta}_o - \delta^{\text{man}}$ exhibited consistent variations, up to the same order of magnitude as δ^{man} , within the same record. Moreover, in some records such quantity underwent changes in sign of the order of hundreds of microVolt.

Hence, since the offset ϕ in (7.6.5) cannot be determined, manual annotations about peak amplitude of ST episodes cannot be exploited as a reference to evaluate distortion introduced in the ST segment by removing baseline wander. To overcome this, we considered the overall ST segment deviation, meant as the sum of a possible offset and the transient variation. This can be evaluated as the difference between the ST segment level and the isoelectric PQ level. Thus, distortion introduced in the ST segment by baseline wander removal was quantified by comparing the difference, computed on the detrended ECG, between the ST segment level and isoelectric PQ level with the same quantity computed on the ECG affected by baseline wander. We denoted by ϵ_i such distortion introduced by any algorithm alg_k in the generic i th ECG beat exhibiting ST segment deviation. The quantity ϵ_i was defined as

$$\epsilon_i(\text{alg}_k) = \left| \frac{a_i^{(\text{alg}_k)} - z_i^{(\text{alg}_k)} - (a_i^\circ - z_i^\circ)}{a_i^\circ - z_i^\circ} \right| \quad (7.6.6)$$

⁴Analogous results were achieved considering the median of such difference.

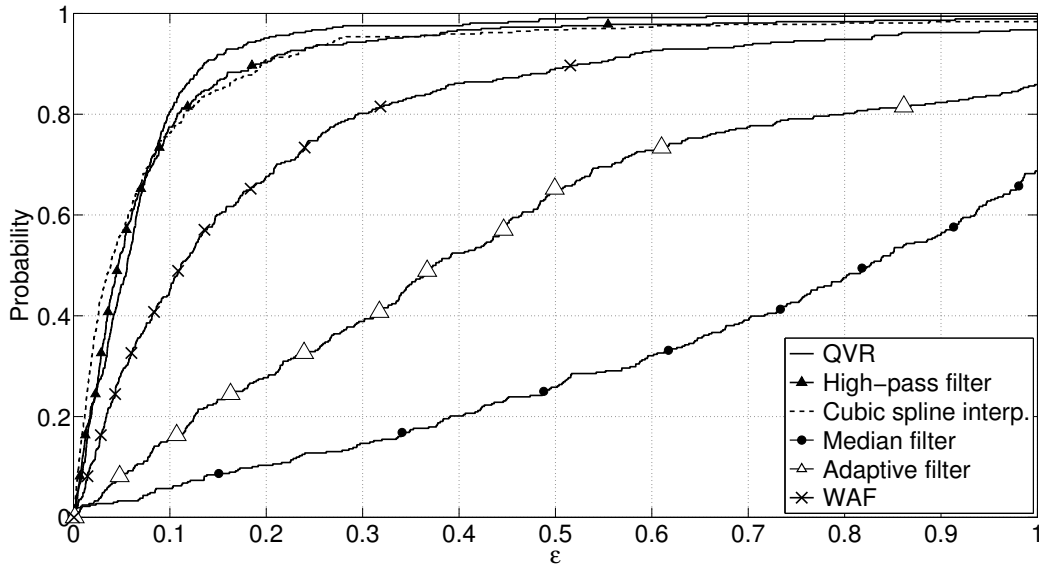


Figure 7.6.13: Empirical distribution functions of distortion (7.6.6) introduced in the ST segment by the proposed approach and state of the art (WAF: Wavelet Adaptive Filter) [13].

where $a_i^{\text{alg}_k}$ and a_i° denote the ST segment level in the ECG detrended by means of alg_k and in the one affected by baseline drift, respectively; $z_i^{\text{alg}_k}$ and z_i° are the isoelectric level in the ECG detrended by means of alg_k and in the one affected by baseline drift, respectively. Moreover, since we do not make use of manual annotations on peak amplitudes of ST episodes, we could consider in our analysis all ECG beats within the beginning and the end of each annotated ST episode. However, to the purpose of our analysis, the difference $a_i^\circ - z_i^\circ$ must not be affected by baseline drift, and should account only for ST segment displacement (elevation or depression). Beats in which ST segment displacement is contributed also by baseline wander must be discarded. Indeed, if they were considered, baseline removal would augment numerator of (7.6.6), thus resulting in great ST distortion, although the amplitude of ST segment relative to the isoelectric level is not altered. To overcome this issue, we focused only on beats annotated as peaks of ST episodes, since they are not affected by baseline wander varying from the PQ to the ST segment. In total, we evaluated the distortion of the ST segment for $N = 371$ beats.

<i>Method</i>	<i>Mean</i>	<i>Variance</i>
Quadratic variation reduction	0.08	0.03
High-pass filtering	0.11	0.13
Cubic spline interpolation	0.10	0.04
Wavelet adaptive filtering	0.24	0.24
Adaptive filtering	0.63	1.70
Median filtering	0.91	1.39

Table 7.3: Mean and variance of distortion (7.6.6) introduced in the ST segment by the proposed approach and state-of-the-art algorithms for baseline wander removal [13].

We compared the performance of our algorithm with the following approaches to baseline wander removal: i) high-pass filtering [16, 22, 99], ii) cubic spline interpolation [143], iii) wavelet adaptive filtering [146], iv) adaptive filtering [74], and v) median filtering [140]. The high-pass filter is a linear-phase FIR equiripple filter, with 0.1 dB ripple in passband, 80 dB attenuation in stopband, and cut-off frequency 0.67 Hz compliant with AHA recommendations [99]. Such tight requirements result in a filter with 4039 taps, and imply such an high computational burden that in practice much looser requirements are considered. Cubic spline interpolation [143] relies on the accurate location of isoelectric knots. Since the procedure proposed in [143] for location of knots requires prior location of R peaks and is time consuming, we located knots according to the procedure in [16] for locating isoelectric PQ level. To this end, annotations of normal beats in the database were exploited. The window size of the median filter was chosen adapting the criterion proposed in [140] to the sampling frequency of 250 Hz. The convergence parameters of the adaptive filter and the wavelet adaptive filter were set to obey AHA requirements on cut-off frequency [99]. The parameter λ for QVR was coarsely set to 10^4 , without any optimization. Indeed, we have shown in the previous subsection that the value of λ is not a critical issue, since a wide range of different values produces similar good estimates of baseline wander [10, 12].

Being distortion in (7.6.6) a random variable, performance of different algorithms was measured in terms of the empirical distribution function of the corresponding error (7.6.6), namely

$$\hat{F}^{(\text{alg}_k)}(\varepsilon) = \frac{1}{N} \sum_{i=1}^N \chi_{(-\infty, \varepsilon]}[\varepsilon_i(\text{alg}_k)] \quad (7.6.7)$$

where $\chi_E(\cdot)$ is the indicator function of the set E , N is the number of beats with ST segment deviation considered, and alg_k is one of QVR, high-pass filtering, cubic spline interpolation, wavelet adaptive filtering, adaptive filtering, and median filtering. The importance of the use of empirical distribution function has been motivated in Subsection 7.6.1.1.

Figure 7.6.13 reports the empirical distribution functions (7.6.7) of distortions (7.6.6) introduced in the ST segment by the algorithms for baseline wander removal under analysis [13]. As Figure 7.6.13 shows, median, adaptive, and wavelet adaptive filtering introduce noticeable distortions in the ST segment. On the contrary, QVR, high-pass filtering and cubic spline interpolation exhibit a high probability of introducing low distortions in the ST segment.

Table 7.3 reports mean value and variance of distortion (7.6.6) introduced in the ST segment by our approach and the state of the art [13]. Results show that baseline wander removal by QVR introduces on average minor distortion in the ST segment displacement, thus outperforming competing algorithms. It should be noted that performances of high-pass filtering and cubic spline interpolation should be considered optimistic, since the filter synthesized here is much more performing than filters used in practice and cubic spline interpolation has been fed with a priori information from manual annotations. Moreover, the filter cut-off frequency complies with AHA requirements tailored right to preserve the ST segment. This choice may result in residual drift in the filtered signal, since baseline wander has spectral components beyond such cut-off frequency.

For the sake of completeness, we point out that, as an alternative to the European ST-T Database, we could have used the long term ST database [178], also available on PhysioNet [19]. Indeed, it contains ECG recordings with episodes of ST segment changes too, and manual annotations in the long term ST database contain plenty more information than the European ST-T Database. However, annotations in the long term ST database do not refer to original recordings, but were

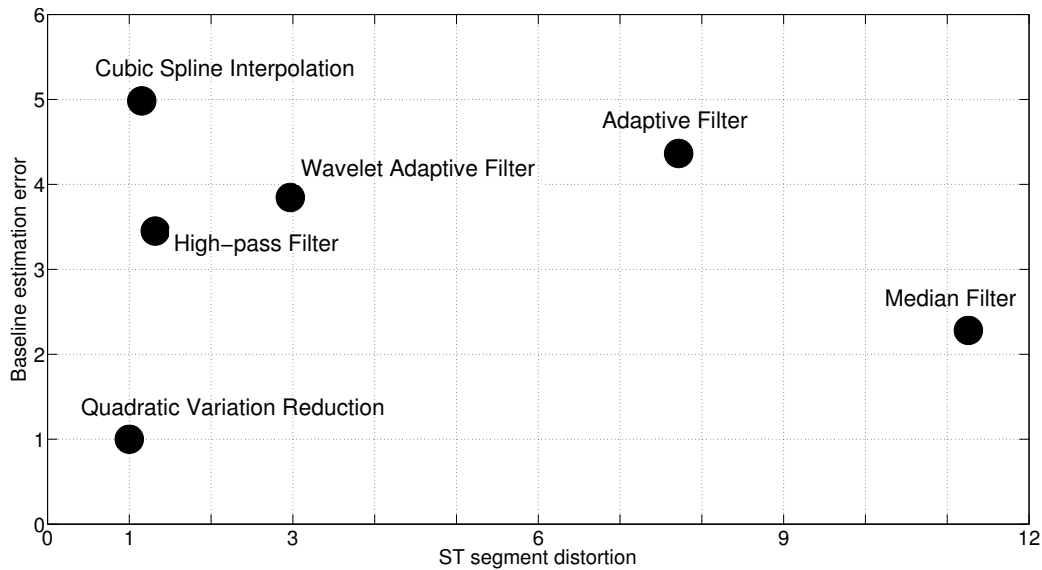


Figure 7.6.14: Overall performance of our approach and state-of-the-art algorithms in terms of baseline estimation error and distortion introduced in the ST segment. Values are referred to baseline estimation error and distortion introduced in the ST segment by our approach [13].

measured after low-pass filtering and baseline wander removal by cubic spline interpolation [178]. Thus, such annotations are unprofitable to our purpose, since our analysis is tailored right on distortions due to the operation of baseline wander removal.

7.6.3 Overall performance

In this subsection we present an overall analysis of performances of our approach and state-of-the-art algorithms for baseline wander removal [13]. Algorithms are *jointly* compared in terms of effectiveness in removing baseline drift, distortion introduced in the ST segment and computational burden. It is worthwhile noting that, to the best of our knowledge, such a joint analysis has not been conducted in the literature before.

In Figure 7.6.14 we consider jointly effectiveness in removing baseline wander and amount of distortion induced in the ST segment by the algorithms we consid-

ered in the previous subsection. In particular, in abscissa of Figure 7.6.14 we report mean distortion introduced in the ST segment from Table 7.3, considering as a reference mean distortion introduced by our approach. The ordinates represent mean error in estimating baseline wander as from numerical results in Subsection 7.6.1.3 [12], considering as a reference mean reconstruction error by our approach. As a consequence, baseline removal by QVR is located at coordinates (1, 1) and is used as a reference. The closer to the origin of axes an algorithm lies, the more performing it is, where performance is meant as effectiveness in removing baseline combined with capability to preserve the ST segment. Figure 7.6.14 highlights that QVR has the best performance and outperforms state-of-the-art algorithms: it achieves best results in baseline wander estimation, while introducing minor distortion in the ST segment [13].

Moreover, we considered execution times required by our approach and competing algorithms. In Table 7.4 we report execution times of different algorithms averaged over 10 runs. Values are expressed relative to execution time required by QVR, namely τ_e . Algorithms have been tested under MATLAB (ver. 7.11) running over a PC equipped with 2.3 GHz Core i5 processor. Table 7.4 indicates that QVR is the fastest algorithm for baseline wander removal, among those effective in removing baseline drift [13]. Indeed, adaptive filtering, being a single pole recursive filter, results in slower execution time than QVR. However, it is faulty either in removing baseline wander either in distorting ST segment, as Figure 7.6.14 shows.

As regards median filter, we report, for the sake of fairness, that we did not make use of an optimized implementation since we considered MATLAB default function. Thus, its performance in terms of execution time in Table 7.4 must be considered somehow pessimistic.

As a conclusion, from Figure 7.6.14 and Table 7.4 it results that QVR has the best performance and is the fastest (among those effective in removing baseline wander) algorithm for baseline wander removal.

7.6.4 Preliminary results on other bioelectrical signals

To conclude, we report preliminary results of the application of the proposed approach to bioelectrical signals other than ECG. In particular, in this paragraph

<i>Method</i>	<i>Execution time</i>
Quadratic variation reduction	τ_e
High-pass filtering	$77 \cdot \tau_e$
Cubic spline interpolation	$33 \cdot \tau_e$
Wavelet adaptive filtering	$5 \cdot \tau_e$
Adaptive filtering	$0.4 \cdot \tau_e$
Median filtering	$457 \cdot \tau_e$

Table 7.4: Execution times of our approach and state-of-the-art algorithms for baseline wander removal. Values are referred to execution time required by our approach [13].

some examples of detrending for EMG and EEG recordings will be considered.

As regards EMG signals, in the top panel of Figure 7.6.15 we show a segment of the nEMG record `emg_healthy` from PhysioNet [19]. The record was acquired from a subject with no history of neuromuscular disease through a 25 mm concentric needle electrode placed in tibialis anterior muscle. The sampling frequency is 4kHz. In the bottom panel of Figure 7.6.15 we report the same record after detrending using the the proposed approach. The controlling parameter has been roughly set to $\lambda = 400$, without any optimization. Nevertheless, a visual comparison of the figures highlights that the approach effectively removes baseline fluctuation without introducing any visible distortion in motor unit action potentials [10].

Finally, with respect to EEG signals, the top panel of Figure 7.6.16 reports a portion of the EEG record `S001R03_edfm` from the EEG Motor Movement/Imagery Dataset [179, 180], publicly available on PhysioNet [19]. The database collects 64-channel EEG recordings from 109 volunteers performing different motor/imagery tasks. Signals were acquired at a sampling frequency of 160Hz with 13-bit resolution [179]. In particular, Figure 7.6.16 shows a recording from the frontal electrode `Fp2`, which is highly susceptible to artifacts caused by eye movements and blinking. In the bottom panel of Figure 7.6.16 we report the same signal detrended using quadratic variation reduction, with $\lambda = 100$. Again, no optimiza-

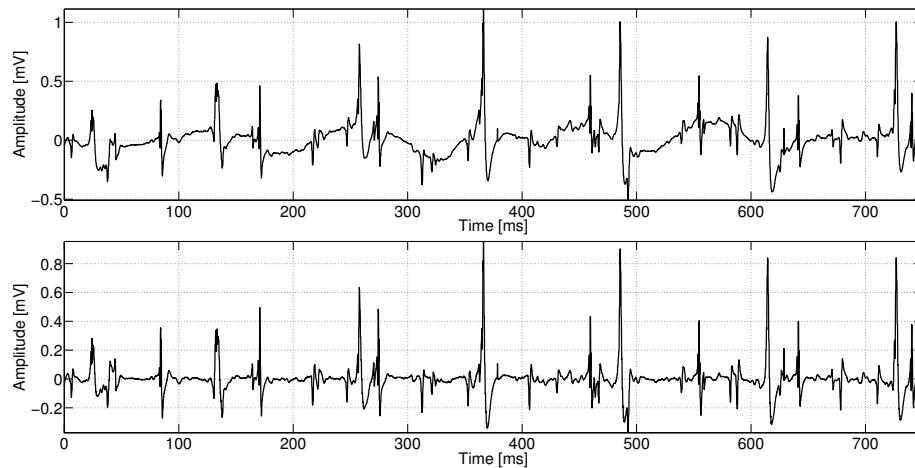


Figure 7.6.15: nEMG from real data: segment of record `emg_healthy` from PhysioNet (top) and the same signal after detrending by the proposed approach [10].

tion in the choice of λ has been performed. Note that signals in the two figures are plotted on different scales, and the noise level of the detrended record is not increased. Rather, quadratic variation reduction effectively removes only slowly varying trends without affecting rapid variations [10].

7.7 Conclusions

In this chapter we have considered the problem of baseline wander estimation and removal for bioelectrical signals. In particular, we focused on ECG due to the critical role of baseline wander removal for this class of signals. The in-band nature of baseline wander makes its removal difficult without affecting the ECG, and in particular the ST segment, thus spoiling relevant clinical information. The ST segment is a portion of ECG signal with high clinical relevance, since it is related to the diagnosis of acute coronary syndromes. These include some of the most severe forms of heart disease and are the main cause of mortality in developed countries. In this chapter we have proposed to tackle the problem of baseline wander removal from a novel perspective, considering the *quadratic variation* as an alternative measure of variability not directly related to the frequency domain. The problem of baseline wander estimation is recast as a constrained convex op-

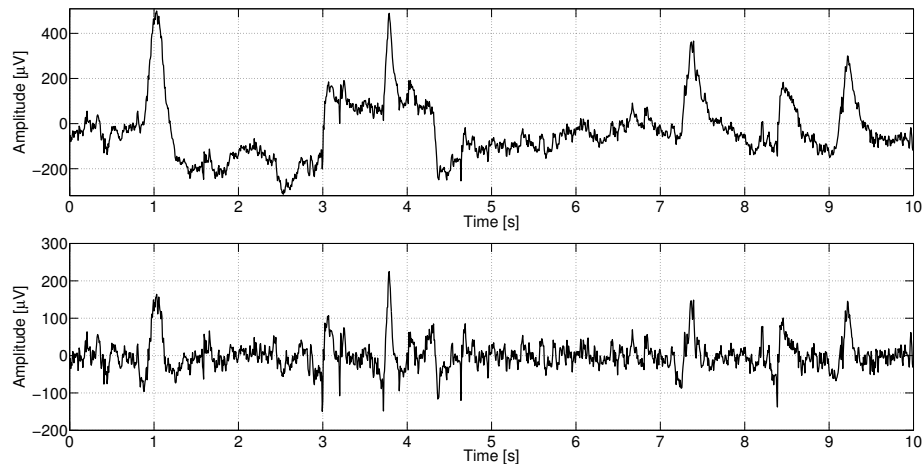


Figure 7.6.16: EEG from real data: segment of record S001R03_edfm from PhysioNet (top) and the same signal after detrending by the proposed approach (bottom) [10].

timization problem, where quadratic variation enters as a constraint. Baseline is estimated searching for the signal closest to the observed one, but exhibiting reduced quadratic variation. The algorithm depends on a single parameter whose value is not critical. Performances of the algorithm have been evaluated with regard to several aspects: effectiveness in removing baseline, distortion introduced in the ST segment, and computational burden. An extensive comparison with state-of-the-art approaches has been carried out. Numerical results confirm the effectiveness of the approach, which outperforms state-of-the-art algorithms and effectively removes baseline drift, while preserving the ST segment. Moreover, it results statistically *uniformly better* than competing algorithms with respect to effectiveness in removing baseline drift. Its sensitivity to variations of the controlling parameter has been analyzed. The algorithm proves to be robust with respect to variations of the controlling parameter. Indeed, a wide range of different values produces similar good estimates of baseline wander, thus making the choice of the parameter not a critical issue.

Furthermore, the proposed algorithm compares favorably also in terms of computational complexity, which is *linear* in the size of the signal to detrend. This makes it suitable for real-time applications as well as for applications on devices with reduced computing power, e.g., handheld devices. From an overall

analysis of performances, quadratic variation reduction results the most effective and the fastest algorithm for baseline wander removal, among those effective in removing baseline wander.

Finally, it is worthwhile remarking that the proposed algorithm is not limited to ECG, but can be effectively applied to a broader class of bioelectrical signals. Indeed, the formulation and the rationale behind it have general validity. In this regard, preliminary results on EEG, EMG, and EOG signals are encouraging.

Chapter 8

Conclusions

Throughout this dissertation, we have proposed techniques for smoothing, rejection of power-line noise and narrowband artifacts, either for single waves (Chapter 3 and 4) or entire ECGs (Chapter 5 and 6), and for baseline wander removal (Chapter 7). They all share, although with different technicalities, a common approach, based on the notion of *quadratic variation reduction*. We have proved in Chapter 3 that the quadratic variation is a consistent measure of variability. All the proposed algorithms achieve smoothing by properly reducing the quadratic variation. They allow us to remove several kinds of noise and artifacts that commonly corrupt ECG signal. The common approach and the purpose make them a *framework* for ECG signal processing. Such a framework enjoys the following properties:

Effectiveness. Numerical results, both on real and synthetic signals, show that all the proposed approaches are very effective in denoising, smoothing, and in general improving the quality of ECG. They achieve considerable SNR (or SNIR) gain for all practical values of input SNR (or SNIR). The algorithms for denoising single waves and entire records of ECG, presented in Chapter 3 and Chapter 5 respectively, outperform approaches currently used in the practice. Our approach to baseline wander removal, described in Chapter 7, has been fully characterized in terms of: i) effectiveness in removing baseline wander, and ii) distortion introduced in the ST segment. An extensive comparison with state-of-the-art algorithms has shown the superiority of the proposed approach, which is statistically uniformly better than competing algorithms and introduces less distortion in the

ST segment.

Computational efficiency. The proposed algorithms are favorably also in terms of computational complexity. Indeed, algorithms presented in chapters 3, 5 and 7 have *linear* complexity, whereas the complexity of the algorithms in chapters 4 and 6 is $O(n \log n)$, being n the size of the signal to process. This increase in complexity is due to an additional step requiring the computation of the DFT of the processed signal. In this regard, we have recently devised a novel algorithm for narrowband artifact rejection that has linear computational complexity. Some details are given at the end of this chapter. The computational efficiency makes the proposed framework suitable for real time applications and for applications on devices with reduced computing power, such as handheld devices.

Generality. The proposed approaches were devised considering the ECG as target. However, they do not rely on the structure of the signal to process, as the formulation and the rationale behind them have general validity. As a consequence, they are not limited to ECG, and can be effectively applied to a broader class of bioelectrical signals. In this regard, preliminary results on EEG, EMG, and EOG signals are encouraging. It is worth noting that the smoothing algorithms presented in Chapter 5 and Chapter 6 benefit the pseudoperiodical nature of the ECG signal, which entails a reduction in the number of independent parameters, but do not rely on it. The approaches presented in Chapter 4 and 6 exploit the structure of the artifacts to reject without relying on the structure of the signal to smooth.

From a practical perspective, the availability of a such a fast framework for processing ECG is particularly relevant when using handheld devices, especially mobile phones, which are nowadays pervasive. This may turn important when working in depressed areas of less-developed countries, where, due to a lack of adequate primary care capacity, ECG is acquired under not ideal conditions, often by untrained people, and with low-cost recorders, i.e., more sensitive to artifacts and noise.

Future works

Finally, we have recently devised two further algorithms for ECG smoothing. They are not presented in this dissertation, but preliminary results are encour-

aging. The first is an algorithm for suppressing narrowband artifacts. It is based on the notion of *modulated quadratic variation*, which is a measure of variability for modulated signals. Narrowband artifacts are suppressed in a way similar to the way we remove baseline wander, which is a narrowband artifact centered at 0Hz. The algorithm is favorable in terms of computational complexity, which is *linear* in the size of the vector to process. The second is a 2D extension of the smoothing algorithm based on quadratic variation reduction. It has been devised to smooth images, nevertheless it is useful in smoothing ECG records exploiting the fact that the ECG signal can be approximately considered as a cyclostationary process [181]. In smoothing ECG we can exploit both the correlation between adjacent samples and the correlation between samples located one beat apart. It is possible to prove that the problem of smoothing a set of ECG beats taking into account both the correlations is equivalent to the smoothing of an image.

Bibliography

- [1] A. Fasano, V. Villani, L. Vollero, and F. Censi, "ECG P-wave smoothing and denoising by quadratic variation reduction," *Proc. 4th Int. Conf. Bio-Inspired Syst. Signal Process. (BIOSIGNAL)*, pp. 289–294, 2011.
- [2] A. Fasano and V. Villani, "Smoothing and denoising for ECG waves by quadratic variation reduction," *In preparation*.
- [3] V. Villani, A. Fasano, L. Vollero, F. Censi, and G. Boriani, "Measuring P-wave morphological variability for AF-prone patients identification," *Proc. 4th Int. Conf. Bio-Inspired Syst. Signal Process. (BIOSIGNAL)*, pp. 481–484, 2011.
- [4] A. Fasano, V. Villani, and L. Vollero, "Denoising and harmonic artifacts rejection for ECG P-waves by quadratic variation reduction," *Proc. 33rd Annu. Int. Conf. IEEE Eng. Med. Biol. Soc. (EMBC)*, pp. 981–984, 2011.
- [5] —, "ECG smoothing and denoising by local quadratic variation reduction," *Proc. 4th Int. Symp. Appl. Sci. Biomed. Commun. Tech. (ISABEL)*, 2011.
- [6] A. Fasano, V. Villani, and G. Iannello, "ECG denoising and power-line interference rejection by local quadratic variation reduction," *Terzo Congresso del Gruppo Nazionale di Bioingegneria (GNB2012)*, 2012.
- [7] A. Fasano and V. Villani, "Joint denoising and narrowband artifact rejection for ECG signals," *IEEE Comput. Cardiol. (CinC)*, vol. 39, pp. 49–52, 2012.

Bibliography

- [8] A. Fasano, V. Villani, and L. Vollero, "Fast ECG baseline wander removal preserving the ST segment," *Proc. 4th Int. Symp. Appl. Sci. Biomed. Commun. Tech. (ISABEL)*, 2011.
- [9] —, "Baseline wander estimation and removal by quadratic variation reduction," *Proc. 33rd Annu. Int. Conf. IEEE Eng. Med. Biol. Soc. (EMBC)*, pp. 977–980, 2011.
- [10] A. Fasano and V. Villani, "Baseline wander removal for bioelectrical signals by quadratic variation reduction," *Submitted for publication*, 2013.
- [11] A. Fasano, V. Villani, and G. Iannello, "Fast and effective baseline wander estimation and removal," *Terzo Congresso del Gruppo Nazionale di Bioingegneria (GNB2012)*, 2012.
- [12] A. Fasano and V. Villani, "Fast baseline wander estimation and removal by quadratic variation reduction," *Submitted for publication*, 2013.
- [13] V. Villani and A. Fasano, "Fast ECG baseline wander removal preserving the ST segment," *In preparation*.
- [14] A. C. Guyton and J. E. Hall, *Textbook of Medical Physiology*, 11th ed. Elsevier Saunders, 2006.
- [15] R. E. Klabunde, *Cardiovascular Physiology Concepts*, 2nd ed. Wolters Kluwer - Lippincott Williams & Wilkins, 2012.
- [16] G. D. Clifford, F. Azuaje, and P. McSharry, Eds., *Advanced Methods and Tools for ECG Data Analysis*. Artech House, Inc., 2006.
- [17] J. G. Webster, Ed., *Medical Instrumentation: Application and Design*, 4th ed. John Wiley & Sons, Inc., 2010.
- [18] R. M. Millis, Ed., *Advances in Electrocardiograms - Methods and Analysis*. InTech, 2012.
- [19] A. L. Goldberger, L. A. N. Amaral, L. Glass, J. M. Hausdorff, P. C. Ivanov, R. G. Mark, J. E. Mietus, G. B. Moody, C. K. Peng, and H. E. Stanley,

Bibliography

- “PhysioBank, PhysioToolkit, and PhysioNet: Components of a new research resource for complex physiologic signals,” *Circulation*, vol. 101, no. 23, pp. e215–e220, 2000.
- [20] J. G. Webster, Ed., *The Measurement, Instrumentation, and Sensors Handbook*. CRC Press LLC and Springer-Verlag GmbH & Co. KG, 1999.
- [21] B. Surawicz, *Chou’s Electrocardiography in Clinical Practice*, 6th ed. SAUNDERS ELSEVIER, 2008.
- [22] L. Sörnmo and P. Laguna, *Bioelectrical Signal Processing in Cardiac and Neurological Applications*. Elsevier Academic Press, 2005.
- [23] D. B. Foster, *Twelve-Lead Electrocardiography: Theory and Interpretation*, 2nd ed. Springer-Verlag, 2007.
- [24] J. C. Huhta and J. G. Webster, “60-Hz interference in electrocardiography,” *IEEE Trans. Biomed. Eng.*, vol. 20, no. 2, pp. 91–101, 1973.
- [25] R. E. Gregg, S. H. Zhou, J. M. Lindauer, E. D. Helfenbein, and K. K. Giuliano, “What is inside the electrocardiograph?” *J. Electrocardiol.*, vol. 41, pp. 8–14, 2008.
- [26] C. Levkov, G. Mihov, R. Ivanov, I. Daskalov, I. Christov, and I. Dotsinsky, “Removal of power-line interference from the ECG: a review of the subtraction procedure,” *BioMed. Eng. OnLine*, vol. 4, no. 50, 2005.
- [27] N. Nikolaev, A. Gotchev, K. Egiazarian, and Z. Nikolov, “Suppression of electromyogram interference on the electrocardiogram by transform domain denoising,” *Med. Biol. Eng. Comp.*, vol. 39, pp. 649–655, 2001.
- [28] E. Huigen, A. Peper, and C. A. Grimbergen, “Investigation into the origin of the noise of surface electrodes,” *Med. Biol. Eng. Comp.*, vol. 40, pp. 332–338, 2002.
- [29] A. J. Brewer, E. S. Lane, P. Ross, and B. Hachwa, “Misdiagnosis of peri-operative myocardial ischemia: The effects of electrocardiogram filtering,” *Anesth. Analg.*, vol. 103, no. 6, pp. 1632–1634, 2006.

Bibliography

- [30] V. Fuster, L. E. Rydén, R. W. Asinger, D. S. Cannom, H. J. Crijns, R. L. Frye, J. L. Halperin, G. N. Kay, W. W. Klein, S. Lévy, R. L. McNamara, E. N. Prystowsky, L. S. Wann, D. G. Wyse, R. J. Gibbons, E. M. Antman, J. S. Alpert, D. P. Faxon, V. Fuster, G. Gregoratos, L. F. Hiratzka, A. K. Jacobs, R. O. Russell, S. C. Smith, E. C. for Practice Guidelines & Policy Conferences Members, W. W. Klein, A. Alonso-Garcia, C. Blomström-Lundqvist, G. de Backer, M. Flather, J. Hradec, A. Oto, A. Parkhomenko, S. Silber, and A. Torbicki, “ACC/AHA/ESC guidelines for the management of patients with atrial fibrillation: Executive summary,” *Circulation*, vol. 104, pp. 2118–2150, 2001.
- [31] A. S. Go, E. M. Hylek, K. A. Phillips, Y. Chang, L. E. Henault, J. V. Selby, and D. E. Singer, “Prevalence of diagnosed atrial fibrillation in adults: national implications for rhythm management and stroke prevention: the AnTicoagulation and Risk Factors in Atrial Fibrillation (ATRIA) Study,” *JAMA*, vol. 285, pp. 2370–2375, 2001.
- [32] V. L. Roger, A. S. Go, D. M. Lloyd-Jones, E. J. Benjamin, J. D. Berry, W. B. Borden, D. M. Bravata, S. Dai, E. S. Ford, C. S. Fox, H. J. Fullerton, C. Gillespie, S. M. Hailpern, J. A. Heit, V. J. Howard, B. M. Kissela, S. J. Kittner, D. T. Lackland, J. H. Lichtman, L. D. Lisabeth, D. M. Makuc, G. M. Marcus, A. Marelli, D. B. Matchar, C. S. Moy, D. Mozaffarian, M. E. Mussolino, G. Nichol, N. P. Paynter, E. Z. Soliman, P. D. Sorlie, N. Sotodehnia, S. S. Turan, Tanya N. and Virani, N. D. Wong, D. Woo, and M. B. Turner, “Heart disease and stroke statistics – 2012 update : A report from the american heart association,” *Circulation*, vol. 125, pp. e2–e220, 2012.
- [33] E. J. Benjamin, P. A. Wolf, R. B. D’Agostino, H. Silbershatz, W. B. Kannel, and D. Levy, “Impact of atrial fibrillation on the risk of death: the Framingham Heart Study,” *Circulation*, vol. 98, pp. 946–952, 1998.
- [34] J. Y. Le Heuzey, O. Paziand, O. Piot, M. A. Said, X. Copie, T. Lavergne, and L. Guize, “Cost of care distribution in atrial fibrillation patients: the COCAF study,” *Am. Heart J.*, vol. 147, no. 1, pp. 121–126, 2004.

Bibliography

- [35] M. V. Perez, F. E. Dewey, R. Marcus, E. A. Ashley, A. A. Al-Ahmad, P. J. Wang, and V. F. Froelicher, "Electrocardiographic predictors of atrial fibrillation," *Am. Heart J.*, vol. 158, no. 4, pp. 622–628, 2009.
- [36] P. G. Platonov, "P-wave morphology: Underlying mechanisms and clinical implications," *Ann. Noninvasive Electrocardiol.*, vol. 17, no. 3, pp. 161–169, 2012.
- [37] A. Bayés de Luna, J. Guindo, X. Viñolas, A. Martinez-Rubio, R. Oter, and A. Bayés-Genís, "Third-degree inter-atrial block and supraventricular tachyarrhythmias," *Europace*, vol. 1, pp. 43–46, 1999.
- [38] P. G. Platonov, J. Carlson, M. P. Ingemansson, A. Roijer, A. Hansson, L. V. Chireikin, and S. B. Olsson, "Detection of inter-atrial conduction defects with unfiltered signal-averaged P-wave ECG in patients with lone atrial fibrillation," *Europace*, vol. 2, pp. 32–41, 2000.
- [39] J. Carlson, R. Johansson, and S. B. Olsson, "Classification of electrocardiographic P-wave morphology," *IEEE Trans. Biomed. Eng.*, vol. 48, no. 4, pp. 401–405, 2001.
- [40] J. W. Magnani, M. Williamson, P. T. Ellinor, K. M. Monahan, and E. J. Benjamin, "P wave indices: Current status and future directions in epidemiology, clinical and research applications," *Circ. Arrhythm. Electrophysiol.*, vol. 2, no. 1, pp. 72–79, 2009.
- [41] K. Aytemir, N. Ozer, E. Atalar, E. Sade, S. Aksöyek, K. Ovünç, A. Oto, F. Ozmen, and K. S., "P wave dispersion on 12-lead electrocardiography in patients with paroxysmal atrial fibrillation," *Pacing Clin. Electrophysiol.*, vol. 23, no. 7, pp. 1109–1112, 2000.
- [42] P. E. Dilaveris and J. E. Gialafos, "P-wave duration and dispersion analysis: Methodological considerations," *Circulation*, vol. 103, p. e111, 2001.
- [43] L. Jordaens, R. Tavernier, N. Gorgov, H. Kindt, C. Dimmer, and D. L. Clement, "Signal-averaged P wave: predictor of atrial fibrillation," *J. Cardiovasc. Electrophysiol.*, vol. 9, no. 8 Suppl, pp. S30–S34, 1998.

Bibliography

- [44] M. Klein, S. J. Evans, S. Blumberg, L. Cataldo, and M. M. Bodenheimer, "Use of P-wave-triggered, P-wave signal-averaged electrocardiogram to predict atrial fibrillation after coronary artery bypass surgery," *Am. Heart J.*, vol. 129, no. 5, pp. 895–901, 1995.
- [45] A. Michelucci, L. Padeletti, M. C. Porciani, and G. F. Gensini, "P-wave signal averaging," *Card. Electrophysiol. Rev.*, vol. 1, no. 3, pp. 325–328, 1997.
- [46] A. Michelucci, G. Bagliani, A. Colella, P. Pieragnoli, M. C. Porciani, G. Gensini, and L. Padeletti, "P wave assessment: State of the art update," *Card. Electrophysiol. Rev.*, vol. 6, no. 3, pp. 215–220, 2002.
- [47] D. Darbar, A. Jahangir, S. C. Hammill, and B. J. Gersh, "P wave signal-averaged electrocardiography to identify risk for atrial fibrillation," *Pacing Clin. Electrophysiol.*, vol. 25, no. 10, pp. 1447–1453, 2002.
- [48] D. Giacomelli, J. P. Bourke, A. Murray, and P. Langley, "Spatial pattern of P waves in paroxysmal atrial fibrillation patients in sinus rhythm and controls," *Pacing Clin. Electrophysiol.*, vol. 35, no. 7, pp. 819–826, 2012.
- [49] C. Blanche, N. Tran, F. Rigamonti, B. H., and Z. M., "Value of P-wave signal averaging to predict atrial fibrillation recurrences after pulmonary vein isolation," *Europace*, vol. 15, no. 2, pp. 198–204, 2013.
- [50] F. Censi, G. Calcagnini, I. Corazza, E. Mattei, M. Triventi, P. Bartolini, and G. Boriani, "On the resolution of ECG acquisition systems for the reliable analysis of the P-wave," *Physiol. Meas.*, vol. 33, no. 2, pp. N11–N17, 2012.
- [51] M. Turakhia and Z. H. Tseng, "Sudden cardiac death: Epidemiology, mechanisms, and therapy," *Probl. Cardiol.*, vol. 32, pp. 501–546, 2007.
- [52] P. J. Schwartz and A. Malliani, "Electrical alternation of the T-wave: clinical and experimental evidence of its relationship with the sympathetic nervous system and with the long Q-T syndrome." *Am. Heart J.*, vol. 89, no. 1, pp. 45–50, 1975.

Bibliography

- [53] D. R. Adam, J. M. Smith, S. Akselrod, S. Nyberg, A. O. Powell, and R. J. Cohen, "Fluctuations in T-wave morphology and susceptibility to ventricular fibrillation," *J. Electrocardiol.*, vol. 17, no. 3, pp. 209–218, 1984.
- [54] E. A. Raeder, D. S. Rosenbaum, R. Bhasin, and R. J. Cohen, "Alternating morphology of the QRST complex preceding sudden death," *N. Engl. J. Med.*, vol. 326, no. 4, pp. 271–272, 1992.
- [55] A. A. Armoundas, G. F. Tomaselli, and H. D. Esperer, "Pathophysiological basis and clinical application of T-wave alternans," *J. Am. Coll. Cardiol.*, vol. 40, pp. 207–217, 2002.
- [56] L. Burattini, S. Bini, and R. Burattini, "Comparative analysis of methods for automatic detection and quantification of microvolt T-wave alternans," *Med. Eng. Phys.*, vol. 31, pp. 1290–1298, 2009.
- [57] M. Malik and A. J. Camm, Eds., *Dynamic Electrocardiography*. Blackwell Publishing, 2004.
- [58] J. Kautzner, "Measurement of T-wave alternans," *Card. Electrophysiol. Rev.*, vol. 3, pp. 387–389, 1997.
- [59] J. P. Martínez and S. Olmos, "Methodological principles of T wave alternans analysis: A unified framework," *IEEE Trans. Biomed. Eng.*, vol. 52, no. 4, pp. 599–613, 2005.
- [60] L. Burattini, S. Bini, and R. Burattini, "Automatic microvolt T-wave alternans identification in relation to ECG interferences surviving preprocessing," *Med. Eng. Phys.*, vol. 33, pp. 17–30, 2011.
- [61] L. Burattini, W. Zareba, and R. Burattini, "Assessment of physiological amplitude, duration, and magnitude of ECG T-wave alternans," *Ann. Non-invasive Electrocardiol.*, vol. 14, no. 4, pp. 366–374, 2009.
- [62] D. Janusek, M. Kania, R. Zaczek, H. Zavala-Fernandez, A. Zbieć, g. Opol-ski, and R. Maniewski, "Application of wavelet based denoising for T-wave alternans analysis in high resolution ECG maps," *Meas. Sci. rev.*, vol. 11, no. 6, pp. 181–184, 2011.

Bibliography

- [63] S. E. Shreve, *Stochastic Calculus for Finance II: Continuous-Time Models*. Springer Science+Business Media, Inc., 2004.
- [64] R. A. Horn and C. R. Johnson, *Matrix Analysis*. Cambridge University Press, 1990.
- [65] S. Boyd and L. Vandenberghe, *Convex Optimization*. Cambridge University Press, March 2004.
- [66] H. Lütkepohl, *Handbook of Matrices*. John Wiley & Sons, 1996.
- [67] W.-C. Yueh, "Eigenvalues of several tridiagonal matrices," *Applied Mathematics E-Notes*, vol. 5, no. 1-3, pp. 66–74, 2005.
- [68] A. V. Oppenheim, R. W. Schaffer, and J. R. Buck, *Discrete-Time Signal Processing*, 2nd ed. Prentice-Hall, Inc., 1999.
- [69] G. H. Golub and C. F. van Loan, *Matrix Computation*, 3rd ed. The Johns Hopkins University Press, 1996.
- [70] F. Censi, G. Calcagnini, C. Ricci, R. P. Ricci, M. Santini, A. Grammatico, and P. Bartolini, "P-wave morphology assessment by a Gaussian functions-based model in atrial fibrillation patients," *IEEE Trans. Biomed. Eng.*, vol. 54, no. 4, pp. 663–672, 2007.
- [71] E. Pueyo, J. P. Martinez, and P. Laguna, "Cardiac repolarization analysis using the surface electrocardiogram," *Philos. Transact. A Math Phys. Eng. Sci.*, vol. 367, no. 1887, pp. 213–233, 2009.
- [72] A. Herreros, E. Baeyens, R. Johansson, J. Carlson, J. Peran, and B. Olsson, "Analysis of changes in the beat-to-beat P-wave morphology using clustering techniques," *Biomed. Signal Proc. Control*, vol. 4, pp. 309–316, 2009.
- [73] V. D. A. Corino, I. Chouvarda, N. Maglaveras, and L. T. Mainardi, "A beat-to-beat P wave analysis in healthy population," *Computers in Cardiology*, vol. 37, pp. 553–556, 2010.

Bibliography

- [74] N. V. Thakor and Y. S. Zhu, "Applications of adaptive filtering to ECG analysis: Noise cancellation and arrhythmia detection," *IEEE Trans. Biomed. Eng.*, vol. 38, no. 8, pp. 785–794, 1991.
- [75] P. S. Hamilton, "A comparison of adaptive and non-adaptive filters for reduction of power line interference in the ECG," *IEEE Trans. Biomed. Eng.*, vol. 43, no. 1, pp. 105–109, 1996.
- [76] S. M. M. Martens, M. Mischi, S. G. Oei, and J. W. M. Bergmans, "An improved adaptive power line interference canceller for electrocardiography," *IEEE Trans. Biomed. Eng.*, vol. 53, no. 11, pp. 2220–2231, 2006.
- [77] S. C. Pei and C. C. Tseng, "Elimination of AC interference in electrocardiogram using IIR notch filter with transient suppression," *IEEE Trans. Biomed. Eng.*, vol. 42, no. 11, pp. 1128–1132, 1995.
- [78] I. Dotsinsky and T. Stoyanov, "Optimization of bi-directional digital filtering for drift suppression in electrocardiogram signals," *J. Med. Eng. Technol.*, vol. 28, no. 4, pp. 178–180, 2004.
- [79] P. E. McSharry, G. D. Clifford, L. Tarassenko, and L. A. Smith, "A dynamical model for generating synthetic electrocardiogram signals," *IEEE Trans. Biomed. Eng.*, vol. 50, no. 3, pp. 289–294, 2003.
- [80] P. Laguna, R. Jané, O. Meste, P. W. Poon, P. Caminal, H. Rix, and N. V. Thakor, "Adaptive filter for event-related bioelectric signals using an impulse correlated reference input: comparison with signal averaging techniques," *IEEE Trans. Biomed. Eng.*, vol. 39, no. 10, pp. 1032–1044, 1992.
- [81] M. Popescu, P. Cristea, and A. Bezerianos, "High resolution ECG filtering using adaptive Bayesian wavelet shrinkage," *Proc. Comput. Cardiol.*, vol. 25, pp. 401–404, 1998.
- [82] H. A. Kestler, M. Haschka, W. Kratz, F. Schwenker, G. Palm, V. Hombach, and M. Hohe, "De-noising of high-resolution ECG signals by combining the discrete wavelet transform with the Wiener filter," *Proc. Comput. Cardiol.*, vol. 25, pp. 233–236, 1998.

Bibliography

- [83] N. Nikolaev and A. Gotchev, "ECG signal denoising using wavelet domain wiener filtering," *Proc. Eur. Signal Process. Conf. (EUSIPCO)*, pp. 51–54, 2000.
- [84] O. Sayadi and M. B. Shamsollahi, "Multiadaptive bionic wavelet transform: Application to ECG denoising and baseline wandering reduction," *EURASIP J. Adv. Signal Process.*, 2007.
- [85] S. G. Mallat, "A theory for multiresolution signal decomposition: the wavelet representation," *IEEE Trans. Pattern Anal. Mach. Intell.*, vol. 11, no. 7, pp. 674–693, 1989.
- [86] C.-H. H. Chu and E. J. Delp, "Impulsive noise suppression and background normalization of electrocardiogram signals using morphological operators," *IEEE Trans. Biomed. Eng.*, vol. 36, no. 2, pp. 262–273, 1989.
- [87] Y. Sun, K. L. Chan, and S. M. Krishnan, "ECG signal conditioning by morphological filtering," *Comp. Biol. Med.*, vol. 32, pp. 465–479, 2002.
- [88] S. A. Taouli and F. Bereksi-Reguig, "Noise and baseline wandering suppression of ECG signals by morphological filter," *J. Med. Eng. Technol.*, vol. 34, no. 2, pp. 87–96, 2010.
- [89] G. B. Moody and R. G. Mark, "QRS morphology representation and noise estimation using the Karhunen-Loève transform," *Computers in Cardiology*, vol. 16, pp. 269–272, 1989.
- [90] A. K. Barros, A. Mansour, and N. Ohnishi, "Removing artifacts from electrocardiographic signals using independent components analysis," *Neurocomputing*, vol. 22, pp. 173–186, 1998.
- [91] T. He, G. Clifford, and L. Tarassenko, "Application of ICA in removing artefacts from the ECG," *Neural Comp. Appl.*, vol. 15, pp. 105–116, 2006.
- [92] R. Sameni, M. B. Shamsollahi, C. Jutten, and G. D. Clifford, "A nonlinear Bayesian filtering framework for ECG denoising," *IEEE Trans. Biomed. Eng.*, vol. 54, no. 12, pp. 2172–2185, 2007.

Bibliography

- [93] M. Blanco-Velasco, B. Weng, and K. E. Barner, "ECG signal denoising and baseline wander correction based on the empirical mode decomposition," *Comp. Biol. Med.*, vol. 38, pp. 1–13, 2008.
- [94] N. E. Huang, Z. Shen, S. R. Long, M. C. Wu, H. H. Shih, Q. Zheng, N.-C. Yen, C. C. Tung, and H. H. Liu, "The empirical mode decomposition and the Hilbert spectrum for nonlinear and non-stationary time series analysis," *Proc. Royal Soc. A*, vol. 454, no. 1971, pp. 903–995, 1998.
- [95] P. Flandrin, G. Rilling, and P. Gonçalvès, "Empirical mode decomposition as a filter bank," *IEEE Signal Process. Lett.*, vol. 11, no. 2, pp. 112–114, 2004.
- [96] "QRS detection and waveform boundary recognition using ecgpuwave." [Online]. Available: <http://physionet.org/physiotools/ecgpuwave/>
- [97] G. B. Moody and R. G. Mark, "The impact of the MIT-BIH arrhythmia database," *IEEE Trans. Biomed. Eng.*, vol. 20, no. 3, pp. 45–50, 2001.
- [98] L. Shen and P. Johnston, "A review of electrocardiogram filtering," *J. Electrocardiol.*, vol. 43, pp. 486–496, 2010.
- [99] P. Kligfield, L. S. Gettes, J. J. Bailey, R. Childers, B. J. Deal, E. W. Hancock, G. van Herpen, J. A. Kors, P. Macfarlane, D. M. Mirvis, O. Pahlm, P. Rautaharju, and G. S. Wagner, "Recommendations for the standardization and interpretation of the electrocardiogram: Part I: The electrocardiogram and its technology," *Circulation*, vol. 115, pp. 1306–1324, 2007.
- [100] P. M. Agante and J. P. Marques de Sá, "ECG noise filtering using wavelets with soft-thresholding methods," *Proc. Comput. Cardiol.*, vol. 26, pp. 535–538, 1999.
- [101] C. T. Kelley, *Iterative Methods for Linear and Nonlinear Equations*, ser. Frontiers in Applied Mathematics. SIAM, 1995, vol. 16.
- [102] B. Lütkenhöner, "Baseline correction of overlapping event-related responses using a linear deconvolution technique," *Neuroimage*, vol. 52, pp. 86–96, 2010.

Bibliography

- [103] A. Bulling, J. A. Ward, H. Gellersen, and G. Tröster, "Eye movement analysis for activity recognition using electrooculography," *IEEE Trans. Pattern Anal. Mach. Intell.*, vol. 33, no. 4, pp. 741–753, 2011.
- [104] R. Merletti, "Standards for reporting EMG data," *J. Electromyography Kinesiol.*, vol. 9, no. 1, pp. III–IV, 1999.
- [105] M. J. Stern and J. Engel, *Atlas of EEG Patterns*. Lippincott Williams & Wilkins, 2005.
- [106] E. Niedermeyer and F. Lopes da Silva, Eds., *Electroencephalography*, 5th ed. Lippincott Williams & Wilkins, 2005.
- [107] T. C. Handy, Ed., *Brain Signal Analysis: Advances in Neuroelectric and Neuromagnetic Methods*. The MIT Press, 2009.
- [108] R. Merletti and P. Parker, Eds., *Electromyography: Physiology, Engineering, and Non-Invasive Applications*. Wiley-IEEE Press, 2004.
- [109] J. Kimura, *Electrodiagnosis in Diseases of Nerve and Muscle: Principles and Practice*. OXFORD University Press, 2001.
- [110] C. J. De Luca, L. D. Gilmore, M. Kuznetsov, and S. H. Roy, "Filtering the surface EMG signal: movement artifact and baseline noise contamination," *J. Biomech.*, vol. 43, pp. 1573–1579, 2010.
- [111] I. Rodríguez-Carreño, A. Malanda-Trigueros, L. Gila-Useros, J. Navallas-Irujo, and J. Rodríguez-Falces, "Filter design for cancellation of baseline-fluctuation in needle EMG recordings," *Comp. Meth. Prog. Biomed.*, vol. 81, pp. 79–93, 2006.
- [112] I. Rodríguez, L. Gila, A. Malanda, C. Campos, and G. Morales, "Baseline removal from EMG recordings," *Proc. 23rd Annu. Int. Conf. IEEE Eng. Med. Biol. Soc. (EMBC)*, pp. 1034–1037, 2001.
- [113] V. R. Zschorlig, "Digital filtering of EMG signals," *Electromyography Clin. Neurophysiol.*, vol. 29, pp. 81–86, 1989.

Bibliography

- [114] S. Conforto, T. D'Alessio, and S. Pignatelli, "Optimal rejection of movement artefacts from myoelectric signals by means of a wavelet filtering procedure," *J. Electromyography Kinesiol.*, vol. 9, pp. 47–57, 1999.
- [115] D. A. Winter, G. Rau, R. Kadefors, H. Broman, and C. J. De Luca, "Units, terms and standards in the reporting of EMG research," *International Society of Electrophysiological Kinesiology.*, 1980.
- [116] P. J. Sparto, M. Parnianpour, E. A. Barria, and J. M. Jagadeesh, "Wavelet and short-time Fourier transform analysis of electromyography for detection of back muscle fatigue," *IEEE Trans. Rehabil. Eng.*, vol. 8, no. 3, pp. 433–436, 2000.
- [117] P. Dolan, A. F. Mannion, and M. A. Adams, "Fatigue of the erector spinae muscles: A quantitative assessment using "frequency banding" of the surface electromyography signal," *Spine*, vol. 20, no. 2, pp. 149–159, 1995.
- [118] D. F. Stegeman and H. J. Hermens, "Standards for surface electromyography: The European project surface EMG for non-invasive assessment of muscles (SENIAM)," *Proc. 3rd General SENIAM Workshop*, pp. 108–112, 1998.
- [119] J. Malmivuo and R. Plonsey, *Bioelectromagnetism - Principles and Applications of Bioelectric and Biomagnetic Fields*. Oxford University Press, 1995.
- [120] I. Ruttkay-Nedecký, "Respiratory changes of instantaneous spatial cardiac vectors," in *Vectorcardiography 2. Proceedings of the XIth International Symposium on Vectorcardiography, New York, 1970*, I. Hoffman, R. I. Hamby, and E. Glassman, Eds. North-Holland Publishing, 1971, pp. 115–118.
- [121] L. T. Sheffield, A. Berson, D. Bragg-Renschel, P. C. Gillette, R. E. Hermes, L. Hinkle, H. Kennedy, D. M. Mirvis, and C. Oliver, "AHA special report. Recommendations for standards of instrumentation and practice in the use of ambulatory electrocardiography," *Circulation*, vol. 71, no. 3, pp. 626A–636A, 1985.

Bibliography

- [122] C. Guilleminault, A. Tilkian, and W. C. Dement, “The sleep apnea syndromes,” *Annu. Review Med.*, vol. 27, pp. 465–484, 1976.
- [123] M. R. Jarvis and P. P. Mitra, “Apnea patients characterized by 0.02 Hz peak in the multitaper spectrogram of electrocardiogram signals,” *IEEE Comput. Cardiol. (CinC)*, vol. 27, pp. 769–772, 2000.
- [124] “2005 American Heart Association guidelines for cardiopulmonary resuscitation and emergency cardiovascular care, Part 8: stabilization of the patient with acute coronary syndromes,” *Circulation*, vol. 112, pp. IV89–IV110, 2005.
- [125] R. M. Califf and M. T. Roe, *ACS Essentials*. Jones and Bartlett Publishers, 2010.
- [126] V. Fuster, L. Badimon, J. J. Badimon, and J. H. Chesebro, “The pathogenesis of coronary artery disease and the acute coronary syndromes (1),” *N. Engl. J. Med.*, vol. 326, no. 4, pp. 242–250, 1992.
- [127] —, “The pathogenesis of coronary artery disease and the acute coronary syndromes (2),” *N. Engl. J. Med.*, vol. 326, no. 5, pp. 310–318, 1992.
- [128] Y. Birnbaum and B. J. Drew, “The electrocardiogram in ST elevation acute myocardial infarction: correlation with coronary anatomy and prognosis,” *Postgrad. Med. J.*, vol. 79, pp. 490–504, 2003.
- [129] K. Thygesen, J. S. Alpert, H. D. White, and Joint ESC/ACCF/AHA/WHF Task Force for the Redefinition of Myocardial Infarction, “Universal definition of myocardial infarction,” *Circulation*, vol. 116, pp. 2634–2653, 2007.
- [130] S. A. Achar, S. Kundu, and W. A. Norcross, “Diagnosis of acute coronary syndrome,” *Am. Fam. Physician*, vol. 72, no. 1, pp. 119–126, 2005.
- [131] S. E. Papapietro, G. S. Niess, T. D. Paine, J. A. Mantle, C. E. Rackley, R. O. Russell Jr., and W. J. Rogers, “Transient electrocardiographic changes in patients with unstable angina: relation to coronary arterial anatomy,” *Am. J. Cardiol.*, vol. 46, no. 1, pp. 28–33, 1980.

Bibliography

- [132] J. A. Van Alsté and T. S. Schilder, "Removal of base-line wander and power-line interference from the ECG by an efficient FIR filter with a reduced number of taps," *IEEE Trans. Biomed. Eng.*, vol. 32, no. 12, pp. 1052–1060, 1985.
- [133] J. A. Van Alsté, W. Van Eck, and E. Herrmann, "ECG baseline wander reduction using linear phase filters," *Comp. Biomed. Res.*, vol. 19, pp. 417–427, 1986.
- [134] R. A. Frankel, E. W. Pottala, R. W. Bowser, and J. J. Bailey, "A filter to suppress ECG baseline wander and preserve ST-segment accuracy in a real-time environment," *J. Electrocardiol.*, vol. 24, no. 4, pp. 315–323, 1991.
- [135] J. J. Bailey, A. S. Berson, A. Garson, L. G. Horan, P. W. Macfarlane, D. W. Mortara, and C. Zywietz, "Recommendations for standardization and specifications in automated electrocardiography: bandwidth and digital signal processing," *Circulation*, vol. 81, no. 2, pp. 730–739, 1990.
- [136] J. J. Bailey, "The triangular wave test for electrocardiographic devices: A historical perspective," *J. Electrocardiol.*, vol. 37, no. Suppl., pp. 71–73, 2004.
- [137] A. R. Houghton and D. Gray, *Making Sense of the ECG: A Hands-on Guide*, 3rd ed. Hodder Arnold, 2008.
- [138] L. Sörnmo, "Time-varying digital filtering of ECG baseline wander," *Med. Biol. Eng. Comp.*, vol. 31, pp. 503–508, 1993.
- [139] R. Jané, P. Laguna, N. V. Thakor, and P. Caminal, "Adaptive filtering of ECG baseline wander comparative analysis with cubic spline technique," *Computers in Cardiology*, vol. 19, pp. 143–146, 1992.
- [140] A. A. Hiasat, M. M. Al-Ibrahim, and K. M. Gharaibeh, "Design and implementation of a new efficient median filtering algorithm," *IEE Proc. Vis. Image Signal Process.*, vol. 146, no. 5, pp. 273–278, 1999.
- [141] R. Acharya U, J. S. Suri, J. A. E. Spaan, and S. M. Krishnan, Eds., *Advances in Cardiac Signal Processing*. Springer-Verlag, 2007.

Bibliography

- [142] V. S. Chouhan and S. S. Mehta, "Total removal of baseline drift from ECG signal," *Proc. Int. Conf. on Computing: Theory and Application (ICCTA)*, pp. 512–515, 2007.
- [143] C. R. Meyer and H. N. Keiser, "Electrocardiogram baseline noise estimation and removal using cubic splines and state-space computation techniques," *Comp. Biomed. Res.*, vol. 10, no. 5, pp. 459–470, 1977.
- [144] M. Raifel and S. Ron, "Estimation of slowly changing components of physiological signals," *IEEE Trans. Biomed. Eng.*, vol. 44, no. 3, pp. 215–220, 1997.
- [145] J. N. Froning, M. D. Olson, and V. F. Froelicher, "Problems and limitations of ECG baseline estimation and removal using a cubic spline technique during exercise ECG technique," *J. Electrocardiol.*, vol. Supplemental Issue, pp. S149–S157, 1988.
- [146] K. L. Park, K. J. Lee, and H. R. Yoon, "Application of a wavelet adaptive filter to minimise distortion of the ST-segment," *Med. Biol. Eng. Comp.*, vol. 36, no. 5, pp. 581–586, 1998.
- [147] D. Zhang, "Wavelet approach for ECG baseline wander correction and noise reduction," *Proc. 27th Annu. Int. Conf. IEEE Eng. Med. Biol. Soc. (EMBC)*, pp. 1212–1215, 2005.
- [148] K. Daqrouq, "ECG baseline wandering reduction using discrete wavelet transform," *Asian J. Inf. Technol.*, vol. 4, no. 11, pp. 989–995, 2005.
- [149] M. A. Tinati and B. Mozaffary, "A wavelet packets approach to electrocardiograph baseline drift cancellation," *Int. J. Biomed. Imaging*, pp. 1–9, 2006.
- [150] M. Boutaa, F. Bereksi-Reguig, and S. M. A. Debbal, "ECG signal processing using multiresolution analysis," *J. Med. Eng. Technol.*, vol. 32, no. 6, pp. 466–478, 2008.
- [151] I. Daubechies, *Ten Lectures on Wavelets*. SIAM, 1992.

Bibliography

- [152] J. Yao and Y.-T. Zhang, "Bionic wavelet transform: A new time–frequency method based on an auditory model," *IEEE Trans. Biomed. Eng.*, vol. 48, no. 8, pp. 856–863, 2001.
- [153] P. Sun, Q. H. Wu, A. M. Weindling, A. Finkelstein, and K. Ibrahim, "An improved morphological approach to background normalization of ECG signals," *IEEE Trans. Biomed. Eng.*, vol. 50, no. 1, pp. 117–121, 2003.
- [154] T. Y. Ji, Z. Lu, Q. H. Wu, and Z. Ji, "Baseline normalisation of ECG signals using empirical mode decomposition and mathematical morphology," *Electron. Lett.*, vol. 44, no. 2, pp. 82–83, 2008.
- [155] Z. Wu and N. E. Huang, "Ensemble empirical mode decomposition: A noise-assisted data analysis method," *Adv. Adapt. Data Anal.*, vol. 1, no. 1, pp. 1–41, 2009.
- [156] Z.-D. Zhao and Y.-Q. Chen, "A new method for removal of baseline wander and power line interference in ECG signals," *Proc. Int. Conf. Machine Learning Cybernetics (ICMLC)*, pp. 4342–4347, 2006.
- [157] N. Pan, V. Mang I, M. Peng Un, and P. Sio hang, "Accurate removal of baseline wander in ECG using empirical mode decomposition," in *Joint Meeting 6th Int. Symp. Noninvasive Functional Source Imaging of the Brain and Heart & Int. Conf. Functional Biomed. Imaging (NFSI-ICFBI)*, 2007, pp. 177–180.
- [158] K.-M. Chang, "Arrhythmia ECG noise reduction by ensemble empirical mode decomposition," *Sensors*, vol. 10, pp. 6063–6080, 2010.
- [159] J. Łęski and N. Henzel, "ECG baseline wander and powerline interference reduction using nonlinear filter bank," *Signal Process.*, vol. 85, pp. 781–793, 2005.
- [160] M. A. Mneimneh, E. E. Yaz, M. T. Johnson, and R. J. Povinelli, "An adaptive Kalman filter for removing baseline wandering in ECG signals," *Computers in Cardiology*, vol. 33, pp. 253–256, 2006.

Bibliography

- [161] B. Boucheham, Y. Ferdi, and M. C. Batouche, "Piecewise linear correction of ECG baseline wander: a curve simplification approach," *Comp. Meth. Prog. Biomed.*, vol. 78, pp. 1–10, 2005.
- [162] Z. Barati and A. Ayatollahi, "Baseline wandering removal by using independent component analysis to single-channel ECG data," *Proc. Int. Conf. Biomed. Pharm. Eng. (ICBPE)*, pp. 152–156, 2006.
- [163] J. Mateo, C. Sanchez, C. Vaya, R. Cervigon, and J. J. Rieta, "A new adaptive approach to remove baseline wander from ECG recordings using made-line structure," *Computers in Cardiology*, vol. 34, pp. 533–536, 2007.
- [164] F. A. Afsar, M. S. Riaz, and M. Arif, "A comparison of baseline removal algorithms for electrocardiogram (ECG) based automated diagnosis of coronary heart disease," *Proc. Int. Conf. Bioinf. Biomed. Eng. (ICBBE)*, 2009.
- [165] G. Zheng, Y. Gu, and M. Dai, "Distortion measurement of ECG baseline wander elimination," *J. Comput. Inform. Syst.*, vol. 7, no. 5, pp. 1770–1777, 2011.
- [166] A. Gut, *Probability: A Graduate Course*. Springer, 2013.
- [167] O. Thas, *Comparing Distributions*, 1st ed. Springer Publishing Company, Incorporated, 2009.
- [168] H. C. Thode, *Testing for Normality*. CRC Press, 2002.
- [169] R. B. D'Agostino and M. A. Stephen, Eds., *Goodness-of-Fit-Techniques*. New York: Marcel Dekker, 1986.
- [170] S. P. Millard, N. K. Neerchal, and P. Dixon, *Environmental Statistics with S-PLUS*. CRC Press, 2000.
- [171] S. Roman, *Lattices and Ordered Sets*. New York: Springer, 2008.
- [172] P. J. Huber and E. M. Ronchetti, *Robust Statistics*. Wiley, 2009.
- [173] "The MIT-BIH normal sinus rhythm database." [Online]. Available: <http://www.physionet.org/physiobank/database/nsrdb/>

Bibliography

- [174] “MIT-BIH Arrhythmia Database Directory.” [Online]. Available: <http://www.physionet.org/physiobank/database/html/mitdbdir/records.htm>
- [175] A. Taddei, G. Distanti, M. Emdin, P. Pisani, G. B. Moody, C. Zeelenberg, and C. Marchesi, “The European ST-T Database: standard for evaluating systems for the analysis of ST-T changes in ambulatory electrocardiography,” *Eur. Heart J.*, vol. 13, pp. 1164–1172, 1992.
- [176] “Annotations in the European ST-T database.” [Online]. Available: <http://www.physionet.org/physiobank/database/edb/annotations.shtml>
- [177] A. Smrdel and F. Jager, “Automated detection of transient ST-segment episodes in 24 h electrocardiograms,” *Med. Biol. Eng. Comp.*, vol. 42, pp. 303–311, 2004.
- [178] F. Jager, A. Taddei, G. B. Moody, M. Emdin, G. Antolič, R. Dorn, A. Smrdel, C. Marchesi, and R. G. Mark, “Long-term ST database: a reference for the development and evaluation of automated ischaemia detectors and for the study of the dynamics of myocardial ischaemia,” *Med. Biol. Eng. Comp.*, vol. 41, pp. 172–182, 2003.
- [179] G. Schalk, D. McFarland, T. Hinterberger, N. Birbaumer, and J. Wolpaw, “BCI2000: A general-purpose brain-computer interface (BCI) system,” *IEEE Trans. Biomed. Eng.*, vol. 51, no. 6, pp. 1034–1043, 2004.
- [180] “BCI2000.” [Online]. Available: <http://www.bci2000.org>
- [181] W. Gardner and L. Franks, “Characterization of cyclostationary random signal processes,” *IEEE Trans. Inf. Theory*, vol. 21, no. 1, pp. 4–14, 1975.